Capture of Radioactive Iodine and Krypton from Nuclear Off-Gas Streams with a Novel Sorbent

A Thesis
Presented in Partial Fulfillment of the Requirements for the
Degree of Master of Science
with a
Major in Chemical Engineering
in the
College of Graduate Studies
University of Idaho
by

Kai Coldsnow

Major Professor: Vivek Utgikar, Ph.D.
Committee Members: Wudneh Admassu, Ph.D, Matthew Bernards, Ph.D.
Department Administrator: D. Eric Aston, Ph.D

August 2017

Authorization to Submit Thesis

This thesis of Kai Coldsnow, submitted for the degree of Master of Science with a Major in Chemical Engineering and titled "Capture of Radioactive Iodine and Krypton from Nuclear Off-Gas Streams with a Novel Sorbent," has been reviewed in final form. Permission, as indicated by the signatures and dates below, is now granted to submit final copies for the College of Graduate Studies for approval.

Advisor:	Vivek Utgikar, Ph.D.	Date
Committee Members:	Wudneh Admassu, Ph.D	Date
	Matthew Bernards, Ph.D.	Date
Department Chair:	D. Eric Aston, Ph.D	Date

Abstract

Reprocessing of used nuclear fuel (UNF) is key to making nuclear energy a sustainable, viable part of the world's energy portfolio. However, during aqueous reprocessing of UNF, volatile radionuclides are released in off-gas posing a hazard to health and the environment. Of these radionuclides, ^{129}I and ^{85}Kr present the biggest threat and are removal priorities. Since the 1960's, many methods of removing ^{129}I and ^{85}Kr have been employed, including caustic and acidic scrubbing, fluorocarbon absorption, and cryogenic distillation. Each of these processes has pitfalls: the use of toxic and corrosive chemicals, high energy consumption, and high cost upkeep. Removal of off-gas contaminants through adsorption provides a simpler, safer, and more cost-effective method of removal, and research into new materials for adsorption is voluminous. Nonetheless, much of the existing research is bereft of studies at realistic conditions, such as low concentrations, ambient temperatures, and testing adsorbents for the removal of multiple contaminants.

To further this research, we have developed a novel adsorbent consisting of Engelhard titanosilicate 10 supported hollow carbon nano-polyhedrons (C/ETS-10) for the capture of iodine and krypton with large-scale synthesis and cost-effectiveness in mind. We investigated the capture of iodine and krypton on C/ETS-10 under single- and multi-component conditions, ambient temperatures, and concentrations similar to actual off-gas. Additionally, we have developed a mathematical model based on mass-transfer to assist in scale up of the process and compared the model to the well-known Thomas, Yoon-Nelson, and Adams-Bohart kinetic models.

Our investigations show that even in multicomponent conditions, 10 wt% C/ETS-10 has iodine capacity comparable to—and krypton capacity twice that of—silver mordenite, a zeolitic sorbent considered to be at the forefront of sorbents for both ^{129}I and ^{85}Krremoval. Furthermore, the mass-transfer model fit experimental breakthrough curves better than the Thomas, Yoon-Nelson, and Adams-Bohart kinetic models, and its inherent flexibility allows extrapolation to other operating conditions. Overall, 10 wt% C/ETS-10 has proven to be a competitive sorbent for iodine and krypton at realistic off-gas conditions.

Acknowledgements

I could not have asked for a better advisor, mentor, and role model than Dr. Vivek Utgikar. Thank you for your support and wisdom through it all.

Thank you to Dr. Sachin Nandanwar, who carried out his post-doctorate work aiding this research. Your tireless work and colorful background opened my eyes to much.

I am also grateful to have had Jarod Perko, Austin Porter, and Michael Green working as undergraduates tying up loose ends in the lab. Research wouldn't be possible without you!

To my committee members, Dr. Wudneh (Woody) Admassu and Dr. Matthew Bernards, thank you for your sharp and grounded feedback.

This work would not have been possible without all the technical help, advice, and comedic stylings of Dr. Dave MacPherson (Dmac), Dr. James Moberly, Charles Cornwall, and John Faila.

And to the rest of the Chemical & Materials Engineering Department at the University of Idaho: Dr. Eric Aston, Dr. David Drown, Gail Bergman, and Margaret Baker. Thank you for an outstanding education, inexhaustible patience, invaluable guidance, and unwavering support over my 9 years here!

Thank you to my mom, Gillian, who instilled me with the desire to be a lifelong learner and always be true to myself. Thank you for giving me everything.

I am fortunate and grateful to have my sister and brother, Rose and Joe, who allow me to antagonize them while they keep a smiling face. Thank you guys for being good friends as well as family.

A special thank you to Breanna Wong for showing me there is always more to learn, experience, and love. Also, for correcting my thesis. Bre, you constantly surprise and inspire me!

Finally, thank you to all my educators, and role models, and friends.

Table of Contents

List of Tables

List of Figures

Nomenclature

Acronyms

AC	Activated carbon
Ag°Z	Reduced silver mordenite
AgA	Silver-impregnated alumina
AgZ	Silver mordenite
BT	Breakthrough
C/ETS-10	Engelhard titanosilcate 10 supported hollow carbon nano-polyhedron sorbent
C/HCNPHs	Hollow carbon nano-polyhedrons
DF	Decontamination factor
DOG	Dissolver off-gas
EBCT	Empty-bed contact time
EDS	Energy dispersive x-ray spectroscopy
ETS-10	Engelhard titanosilicate 10
GCMC	Grand Canonical Monte Carlo
HZ	Hydrogen mordenite
LCV	Leuco crystal violet
LWRs	Light-water reactors
MFC	Mass flow controller
MOFs	Metal-organic frameworks
MWNTs	Multi-walled carbon nanotubes
NRC	Nuclear Regulatory Commission

o-SWNTs	Open-ended single-walled carbon nanotubes
ORNL	Oak Ridge National Laboratory
RBM	Radial breathing mode
SEM	Scanning electron microscopy
SWNTs	Single-walled carbon nanotubes
TEDA	Triethylenediamine
TEM	Transmission electron microscopy
TGA	Thermogravimetric analysis
THF	Tetrahydrofuran
UNF	Used nuclear fuel
VOG	Vessel off-gas
XRD	X-ray diffraction

Equation Variables

ΔG	Change in Gibbs free energy
ΔH	Change in enthalpy
Δq	Normalized standard deviation
ΔS	Change in entropy
λ	Relaxation factor
ρ_b	Density of the sorbent bed
τ	Time required to reach 50% breakthrough. Used by the Yoon-Nelson model
$C(t, z)$	Bulk concentration of contaminant as a function of time and position in the adsorption column
C_i^l	Bulk concentration in the adsorption column with respect to a time step, l, and column segment, i

C_{i0}	Inlet concentration of contaminant i in dynamic adsorption experiments
C_{ie}	Outlet concentration of contaminant i in dynamic adsorption experiments
D_z	Diffusivity of contaminant through the bulk gas
E_a	Activation energy
H_B	Height of the sorbent bed saturated at t
H_T	Total height of the sorbent bed
H_{MTZ}	Height of the mass-transfer zone
k_a	Rate of adsorption constant
k_AB	Adams-Bohart kinetic constant
k_d	Rate of desorption constant
K_F	Freundlich equilibrium constant
k_i	First order adsorption rate constant
K_L	Langmuir equilibrium constant
k_s	Second order adsorption rate constant
K_t	EBCT constant
k_{i0}	Pre-exponential factor to the adsorption rate constant
k_{TH}	Thomas kinetic constant
k_{YN}	Yoon-Nelson kinetic constant
M	Mass of sorbent charged into the adsorption column
N	Number of experimental data points
N_0	Sorption capacity of the sorbent on a per volume basis. Used by the Adams-Bohart model
Q	Flow rate of gas through adsorption column

$q(t)$	Amount of contaminant adsorbed as a function of time
q_0	Maximum sorbent capacity. Used by the Thomas model
q_e	Equilibrium adsorbed amount
q_i	Sorption capacity of a sorbent for component i
q_m	Maximum sorption capacity of the sorbent
q_{calc}	Calculated adsorbed amount by corresponding model
q_{exp}	Experimental adsorbed amount
q_{iu}	Useable capacity of the sorbent for contaminant i
R	Universal gas constant
r_{ads}	Rate of adsorption
r_{des}	Rate of desorption
T	Temperature
t	Time in adsorption experiment
t_b	Breakthrough time
t_f	Exhaustion time. The time it takes to completely saturate the sorbent with contaminant
v	superficial velocity of gas through the adsorption column
z	Position in the adsorption column

Chapter 1: Introduction and Literature Review

1.1 Nuclear Energy in the 21ST Century

Since the Industrial Revolution in the mid-1700s, people have depended on fossil fuels to drive civilization's growth by providing energy. Today, 60% of the energy in the US is still derived from fossil fuels, the major sources being petroleum, natural gas, and coal. However, the extended use of fossil fuels carries serious consequences. Drought, ecosystem collapse, and rising ocean levels are all triggered by global warming and ocean acidification. This, in turn, disrupts food and water sources. Carbon dioxide (CO_2) released by the burning of fossil fuels is at the root of these issues.

This problem has spurred debate on how we should produce energy to meet demand, both now and in the future, because energy demand is quickly rising—the Energy Information Administration predicting as much as a 56% increase by 2040 [1]. Currently, public sentiment is focused on solar and wind energy, which have little CO_2 emissions and are sustainable. Though solar and wind energy have merit as alternative energy sources, harnessing the power of the sun and wind is expensive and difficult to implement, especially on the scale needed to meet energy demands. This has pushed the US to expand energy production to natural gas because it is perceived as economic and it releases about half the CO_2 that burning coal does to obtain the same energy output. However, if we look to future consequences, the amount of CO_2 emitted by natural gas energy is still excessive. Additionally, all fossil fuels are nonrenewable—there exists only a finite amount—and thus, unsustainable.

Nuclear energy is an alternative to fossil fuels that emits little to no CO_2 or particulates during the operation of nuclear reactors. Nuclear energy harnesses the latent energy within uranium which contains so much energy that a nickel-sized pellet of uranium oxide, used by light-water nuclear reactors (LWRs), has the equivalent energy of one ton of coal. However, the implementation of nuclear energy faces many social and political hurdles because it is viewed as expensive and dangerous by much of the population. In actuality, nuclear plant lifetime costs are among the cheapest per unit of energy produced. It is comparable to or cheaper than the costs of natural gas [2, 3]. The perceived danger associated with nuclear energy can be attributed to large-scale accidents such as Chernobyl and Fukushima, but advanced reactors developed recently overcome many of the shortcomings of older reactors. Thus, the risk of large-scale accidents occurring is

significantly reduced.

Even though nuclear faces opposition in the western countries, what has been called a "nuclear renaissance" emerged in 2001. China is ambitiously aiming to double their nuclear energy output to 58 GWe by 2020, and increasing output to 150 GWe by 2030 [4]. India is on track to add 30 new reactors by 2030 [4]. In fact, the Nuclear Regulatory Commission (NRC) expects the global demand for nuclear energy to increase 100% by 2030 [5]. This increase in demand puts a growing strain on the world's uranium supply. Even at current consumption rates, the world supply of uranium is expected to last only ~200 years, and will last even shorter if nuclear is to replace fossil fuels. Nuclear reprocessing of used nuclear fuel (UNF) can be used to significantly extend the usefulness of the 96% uranium still contained in UNF, of which 0.4–0.8% is fissile uranium and 1% is plutonium. Reprocessing recovers the remaining uranium and plutonium in UNF to create fresh fuel, gaining 25–30% more energy and reducing high-level radioactive waste volume by 80%.

1.2 Used Nuclear Fuel Reprocessing

The two predominant methods of reprocessing are aqueous reprocessing, which uses PUREX (Plutonium Uranium Redox Extraction) for mixed-oxide (MOX) UNF used for LWRs, and electrochemical processing, used for metal alloy fuel used in fast reactors. Currently, the majority of nuclear energy is produced using MOX fuel, thus, developing aqueous reprocessing is more pertinent than electrochemical processing.

A key challenge in the aqueous reprocessing of LWR UNF is the release of volatile radionuclides produced by fission. This collection of gaseous contaminants is called off-gas. MOX nuclear fuel consists of long, hollow, metal rods coated with zircalloy cladding. These fuel rods contain UO_2 pellets at their center as the 'meat'. Collections of fuel rods used in reactors are called fuel assemblies. Once a fuel assembly has been removed from a reactor, it is typically stored underwater in a cooling pool for five years or longer. When reprocessing commences, the fuel assembly is disassembled, and the fuel rods are sheared into 1- to 2-inch lengths. The meat of the fuel is then reacted with oxygen at high temperature in a process called voloxidation. During voloxidation, UO_2 is oxidized to U_3O_8 and becomes a fine powder, which is then dissolved in nitric acid for further extractive separation of the fissile materials. Gases released during the shearing, voloxidation, and dissolution of UNF are considered dissolver off-gases (DOGs), while

gases released in subsequent extraction steps are vessel off-gases (VOGs) [6]. As shown in Fig. 1.1, DOGs contain the majority of the radionuclides released from UNF; thus, they are the primary concern for treatment.

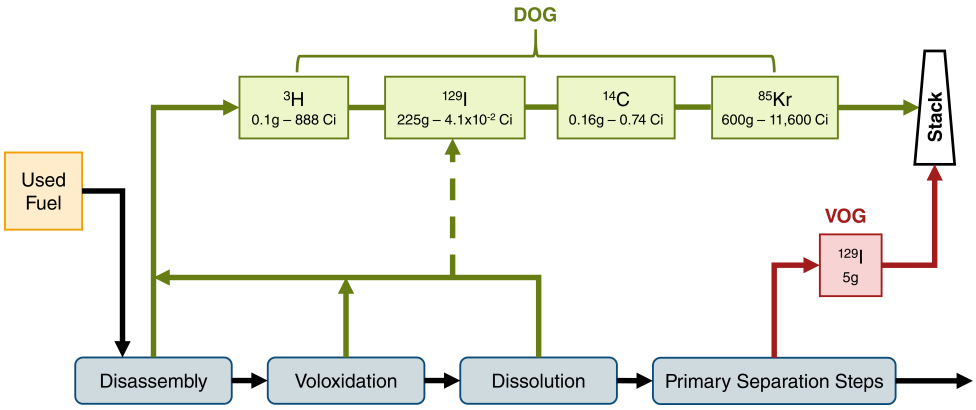

Figure 1.1: Dissolver and vessel off-gas released during UNF reprocessing for 1 MT initial heavy metal LWR UNF reproduced from [6].

The major constituents of DOGs are ^{3}H (tritium), ^{129}I, ^{14}C, ^{85}Kr, and various Xe isotopes. The capture of tritium and ^{14}C is typically of less concern: tritium has a short half-life and a relatively low beta decay energy (18.5 keV), and ^{14}C is not abundant in reprocessing off-gas as it is a neutron activation product and is only weakly radioactive [7, 8]. Xe is also released in off-gas, but the longest lived isotope has a half-life of only 36.4 days and is stable within the cooling period of UNF. ^{129}I and ^{85}Kr present the largest threat and are the main priority for removal.

The regulation 40 CFR 190, established by the EPA, limits their release on a fuel usage basis—no more than 50,000 Ci of ^{85}Kr or 5 mCi of ^{129}I per gigawatt-year of energy produced may be released. To meet these standards, a decontamination factor (DF=initial activity/final activity) of 150–200 is required for ^{129}I. Of course, regulation is only one motivation behind developing capture technology; ^{129}I has a 16-million-year half-life and tends to accumulate in the thyroid, causing health problem. Even though for many years ^{85}Kr was released into the atmosphere and Geary [8] said, "dispersal is almost certainly preferable to disposal," ^{85}Kr is radioactively the hottest nuclide in off-gas, and the atmospheric activity in the northern hemisphere has risen from 0.1 Bq/m^3 in 1959 to 1.2 Bq/m^3 in 2001. Table 1.1 shows the compiled radionuclide information.

Table 1.1: Radionuclides released during UNF reprocessing.

Radionuclide	Half-life (yr)	Effect
^{3}H	12.33	Low decay energy Short half-life
^{14}C	5730	Not abundant in UNF
^{85}Kr	10.73	Accumulating in the atmosphere (0.1 Bq/m^3 in 1959 to 1.2 Bq/m^3 in 2001) Decays to corrosive rubidium
$^{127\text{-}131}Xe$	days	Decays to stable isotope during UNF cooling
^{129}I	1.59 x 10^7	Long half-life Accumulates in thyroid

1.3 Methods for the Capture of Radioactive Iodine and Krypton

1.3.1 Methods for Iodine Capture

Iodine's apparent reactivity has borne many wet scrubbing methods for the removal of both its off-gas forms: I_2, and methyl iodide (organic iodine, CH_3I). Being a halogen, iodine is present in numerous forms in solution, iodide, iodate, hypoiodous acid, hypo iodite, diatomic iodine, etc., depending on the solution's chemical constituents and pH. Hence, wet scrubbing processes for the removal of iodine require many steps to capture iodine and transform it into suitable waste forms.

Alkaline Scrubbing

One of the simplest and most mature wet scrubbing methods is alkaline scrubbing [9, 10]. *La Hague* Reprocessing Facility in France and the Windscale and THORP facilities in the United Kingdom have all used alkaline scrubbing to capture DOG iodine [9]. Off-gas is passed through 1–2 M NaOH and iodine is removed to a modest degree (DF = 10–100). The liquid residue left by the process contains iodine captured as NaI and $NaIO_3$, which must be stabilized either directly

in cement or, more suitably, converted to barium iodate [$Ba(IO_3)_2$] before being stabilized in cement. In theory, alkaline scrubbing should remove all the elemental iodine from the off-gas through the disproportionation reaction;

$$3I_2 + 6OH^- \rightleftharpoons 5I^- + IO_3^- + 3H_2O \tag{1.1}$$

However, alkaline scrubbing has not been able to achieve much higher than 90% efficiency due to the speciation of iodine in the off-gas and its inability to remove organic iodine [11]. Sodium carbonate precipitate is also and issue if the entering gas stream contains significant levels of CO_2, but this may be solved by using KOH in place of NaOH.

KOH and NaOH in molten form have also been studied for the removal of iodine by Trowbridge et al. at Oak Ridge National Laboratories (ORNL) to capture iodine while forgoing the formation of iodate, making transmutation to a suitable waste form more feasible. As much as 96% of iodine was removed, and iodine removal was strongly related to the temperature of the hydroxide melt [12]. The molten hydroxide tests were preliminary, using iodine in 96% argon and 4% hydrogen as off-gas; it is not known how the method would handle NO_x or methyl iodide species.

Iodox

The Iodox process was developed by ORNL in the 1970's to capture ^{131}I released by the reprocessing of liquid metal fast breeder fuel, which has a short cooling period of 180 days [9, 13]. It employs high concentrations (20–23 M) of hyperazeotropic nitric acid (HNO_3) to oxidize and solubilize both elemental and organic iodine [8, 10, 14]. Off-gas is passed through a bubble cap column containing the nitric acid, and the following reactions occur:

$$2CH_3I + 4HNO_3 \rightleftharpoons 2CH_3NO_3 + I_2 + N_2O_4 + 2H_2O \tag{1.2}$$

$$I_2 + 4H_2O \rightleftharpoons 2I^+ + 2NO_3^- + N_2O_4 + H_2O \tag{1.3}$$

$$I^+ + 3HNO_3 + NO_3^- \rightleftharpoons IO_3^- + H^+ + 2N_2O_4 + H_2O \tag{1.4}$$

This results in iodine in solution in the form of iodate. Evaporating the nitric acid leaves solid iodic acid, which must be stabilized in barium iodate for future storage. The Iodox process has a

high DF of 10^4 and has achieved DFs of up to 10^6. The Iodox process has the distinct advantage of handling both NO_2 and moisture in the off-gas streams with with a small removal efficiency decreases; however, the use of high concentrations of nitric acid calls for expensive equipment designed to handle such conditions.

There is a variant of the Iodox process that uses a lower concentration of nitric acid (8–12 M) containing 0.1 M Co^{3+}, which oxidizes both organic and elemental iodine to iodate. Using cobalt as the oxidizing agent is advantageous because it is able to remove organic iodine compounds as well as elemental; however, the DF is lowered to between 100–600 [10]. Furthermore, NO_2 now greatly affects the efficiency—competing with iodine to react with the Co^{3+} ions—reducing the DF up to 10 times with a NO_2 concentration in the off-gas of just 1%.

Mercurex

Similar to the Iodox process, the Mercurex process was developed to handle large amounts of ^{129}I released from short-cooled UNF. Mercurex uses a combination of 0.4 M mercuric nitrate ($Hg(NO_3)_2$) and up to 14 M nitric acid to absorb iodine in a packed or tray column. Full scale Mercurex removal has been used at the Dounreay Plant in the United Kingdom and the full-scale Allied-General Nuclear Services Plant, achieving DFs of 10–150 [9]. Laboratory tests carried out at ORNL showed higher removal efficiencies with DFs up to 10^4. Mercurex is advantageous because it removes organic and elemental through the following reactions [14]:

Elemental iodine:

$$6I_2 + 6Hg(NO_3)_2 + 6H_2O \rightleftharpoons 5HgI_2 + Hg(IO_3)_2 + 12HNO_3 \tag{1.5}$$

Methyl iodide:

$$2CH_3I + Hg(NO_3)_2 \rightleftharpoons HgI_2 + 2CH_3NO_3 \tag{1.6}$$

$$2CH_3I + Hg(NO_3)_2 + 2H_2O \rightleftharpoons HgI_2 + 2CH_3NO_3 + 2HNO_3 \tag{1.7}$$

Mercury is regulated as a toxic metal. Therefore, the Mercurex process would benefit from the conversion of the mercuric iodine compounds to non-mercuric species. This can be accomplished by oxidizing the products to $NaIO_3$, eventually precipitating out iodine as barium iodate.

Organic Solvents

Apart from caustic and acidic scrubbing, both fluorocarbon and polymethylsiloxane solvents have been studied for the removal of iodine from off-gas. Fluorocarbon absorption, absorption in dichlorodifluoromethane (Freon-12), is a robust process that traps ^{85}Kr, ^{14}C, and ^{129}I. ORNL has reported DFs of up to 10^4 for both elemental iodine and methyl iodide [13, 14]. The capture of iodine in fluorocarbon absorption appears to be unimpeded by NO_2 absorption. However, the process requires 400 psig and temperatures of -30 to -15 °C, and its indiscriminate absorption requires further separation of the off-gas components with additional solvent stripping columns.

Polymethylsiloxane solvents have been studied by Russian researchers and exhibit a DF of up to 150 [10], but must be regenerated by passing warm air through the solvent and further alkaline scrubbing must be performed on the resulting concentrated off-gas.

The wet scrubbing processes Iodox and Mercurex have proven effective for the removal of iodine with high decontamination factors and chemical specificity; however, they have many disadvantages. Wet processes negatively impact the environment because of toxic and corrosive chemicals used and they require expensive equipment. Furthermore, steps to immobilize the iodine require even more processes that are chemically intensive and result in large volumes of waste; about 3 m^3 of cement matrix is required to house 340 kg of iodine as barium iodate [8].

1.3.2 Methods for Krypton Capture

Cryogenic Distillation

Cryogenic distillation is the most mature noble gas separation technology—used by nuclear reprocessing facilities for several decades—and is used commercially to separate air into 99.999% pure krypton and xenon. Krypton DFs for cryogenic distillation range from 100–1000 [6, 9]. Unfortunately, other volatile components of off-gas must be removed before the cryogenic distillation step, particularly NO_2, which along with ozone formed during the process, provoke violent reactions [8, 15]. This necessitates methods to remove NO_2, like an alkaline wash, before

distillation. Other NO_x species are removed by passing the off-gas over a rhodium catalyst in excess of 500 °C to reduce them to nitrogen and water before cooling the stream to cryogenic temperatures [9].

Fluocarbon Absorption

Fluorocarbon absorption for the retention of krypton and xenon utilizes the high solubility of krypton and xenon in Freon-12. It is similar to, but advantageous over, cryogenic distillation, because efficient operation is possible over a wider range of temperatures and pressures, and it is insensitive to impurities [15]. Krypton removal efficiencies are high at 99%, but disadvantages remain [6, 8, 9, 15, 16]:

1. High energy consumption and capital costs are comparable to that of cryogenic distillation.
2. Fluorocarbon release into the atmosphere damages the ozone layer.
3. Lack of krypton and xenon separation leads to a waste volume increased by a factor of 10.
4. Solvent is carried over to the product stream.
5. Radiolysis of solute promotes corrosion of equipment.

Like the wet processes for iodine removal, cryogenic distillation and fluorocarbon absorption are undoubtedly effective. However, both consume large amounts of energy to bring off-gas to cryogenic temperatures and suffer from complicated immobilization processes. For example, one method of krypton immobilization involves storing the krypton in steel canisters. This becomes an issue when ^{85}Kr decays to rubidium, a metal that corrodes the container. Another method is to spray the separated krypton into a silica aerogel treated with fluoroalkyl groups. The aerogel must then be densified through isostatic compression or sintering at 1050 °C [17]. This seals the pores, trapping the krypton within. Aerogels provide a stable housing for ^{85}Kr, but the kinetics of aerogel densification are complicated, and further research is required before it can be implemented [17, 18].

1.3.3 Adsorption

The adsorption of radionuclides presents a way to circumvent many of the difficulties associated with other capture methods.

1. Adsorption processes have a simpler design
2. Capture with porous sorbents is comparatively non-corrosive
3. The waste product of adsorptive capture is in a dry form that is much easier to stabilize and dispose of
4. Adsorption is highly reliable
5. Equipment used for adsorption has low maintenance costs
6. The ability to selectively capture of gaseous fission products with unique sorbents enables lower volume of high-level waste
7. Adsorption can be used to capture any contaminant of interest, and separate removal processes for each contaminant are unnecessary

Adsorption is a phenomenon that occurs on surfaces rather than in the bulk phase, like other removal processes. During adsorption, a liquid or gas containing contaminants (i.e., adsorbates or sorbates) contacts the surface of a solid (i.e., adsorbent or sorbent), and the contaminants adhere to the surface of the solid in a thermodynamically favorable process. The strength of the interactions between the contaminants and the sorbent signify how favorable adsorption is on a particular sorbent. If the only interactions are van der Waals forces, then the process is called physisorption; whereas if chemical bonding exists between sorbent and sorbate, it is called chemisorption. Iodine and krypton are most often physisorbed.

Because adsorption is a surface phenomenon, the affinity of the sorbent surface for a particular sorbate and its surface area determine efficiency. The most revealing property of a sorbent is its sorption capacity; sorption capacities are reported as the maximum amount of contaminant (iodine or krypton) per unit of adsorbent. Sorption capacity is commonly reported as the weight of contaminant adsorbed per mass of the sorbent (e.g., mg/g), moles of contaminant adsorbed per mass of sorbent (e.g., mol/g), or a simple weight percentage (mass of adsorbed contaminant/mass of sorbent $\times$ 100). When sorbent capacities are not available from literature, decontamination factors give a measure of how well the sorbent can remove a contaminant. The remainder of this chapter reviews sorbents for the capture of iodine and krypton.

While comparing the sorption capacities of sorbents, it is also important to note that the conditions of adsorption—temperature, carrier gas, flow rate, impurities, feed gas concentra-

tions, and sorbent preparation—significantly affect the sorbent's performance. General thermodynamics dictate that a sorbent's capacity for a particular contaminant increases with increasing contaminant concentration in the bulk fluid, and decreases with higher operating temperatures; though, there are exceptions to both rules. Because the studies detailed in the following sections were performed at so many different conditions, it is difficult to compare sorbents directly based on their capacities. However, an attempt is made to compare each sorbent in relative terms.

1.4 Porous Sorbents for the Capture of ^{129}I

1.4.1 Carbon Materials

Activated carbon (AC) has been the backbone for iodine removal in air ventilation and cleanup systems for decades and with good reason; AC can be derived from coal, coconut, walnut shells, bamboo, or other organic matter, so it is inexpensive and provides over 1000 m^2/g surface area. Additionally, it effectively captures iodine; the DFs for any type of AC exceed 100 under any combination of temperature and humidity found in reprocessing off-gas [14]. In fact, Sun and coworkers [19] have recently developed a KOH activated carbon with a surface area of 1973 m^2/g that captured 376% of its weight in iodine during static adsorption experiments at 350 K; however, its ability to remove CH_3I is lacking. Adams et al. [20] found AC to have a capacity of only 0.08 mg/g (0.008 wt%) for CH_3I. This deficiency is overcome by impregnating AC with chemicals such as urotripine, KI, and triethylenediamine (TEDA). Park et al. [21] found that TEDA-impregnated AC captured 20 wt% CH_3I at 30 °C. Though AC has proven effective for iodine capture in nuclear facilities, its use cannot be extended to nuclear reprocessing off-gas. The performance of AC for iodine adsorption is greatly diminished by acidic conditions, moisture, age of the sorbent, and, perhaps most significantly, temperature. AC at high temperatures is liable to ignite, its ability to hold iodine decreases rapidly, and it undergoes explosive reactions with nitrogen oxides contained in off-gas. These properties also make AC a poor candidate for long-term storage [13, 22].

1.4.2 Silver-Impregnated Sorbents

Among the first options devised to replace AC were metal-loaded zeolites. Zeolites are naturally occurring aluminosilicate materials first discovered for their ability to adsorb large amounts of

water. Over 40 different zeolitic structures have been discovered, but they all share a framework consisting of SiO_4 and AlO_4 joined by oxygen atoms [23]. The aluminum in the zeolite's structure introduces a negative charge, which must be balanced by a cation external to the framework. Typically, the default cation is Na or K, but these can be ion-exchanged with many different metals, such as Cd, Cu, Hg, Mn, Co, Ni, or Ag. This is an advantage of zeolites for iodine capture. Iodine reacts with metal oxides to form metal iodide complexes according to the reaction,

$$2MO(s) + I_2(g) \rightarrow 2MI(s) + O_2(g) \tag{1.8}$$

Where M is a metal. Since each metal cation reacts with a single iodine atom, the metal loading on sorbent materials is important, and every metal-exchanged material retains different weight percentages of the metals. No metal has been found to be as effective for iodine removal as silver ($\Delta G = -16.1$ kcal/mole).

Silver zeolites have been studied for iodine capture as early as 1968 by Maeck et al. [24], who investigated 40 wt% silver Linde Molecular Sieve 13X (a zeolite) for iodine capture. With an iodine feed concentration of 1μg/ft^3 at 25 °C, the zeolite had a DF of 5000—equivalent to the DF found for AC in the same study. However, at 250 °C, the AC desorbed much of its iodine; and at 300 °C, it ignited. The silver-exchanged molecular sieve did not suffer this issue, retaining iodine up to 1000 °C. The zeolite also performed 5–6 times better than AC when steam was introduced into the off-gas. Similarly, 20–30 wt% silver faujasite, studied by Puppe et al. [25], exhibited a high removal efficiency of 99.99% with an iodine feed of 1.27 mg/m^3 at 160 °C and a bed depth of 10 cm. Aging the sorbent with steam-saturated air for four hours at 140 °C only decreased the iodine removal efficiency to 99.83%.

Though these zeolites which are X- and Y-type exhibit substantial iodine removal efficiency, they are highly susceptible to acidic conditions. A zeolite's Si:Al ratio determines its acid resistance; the higher the ratio, the lower pH a zeolite can withstand. X- and Y-type zeolites such as faujasite and Linde MS typically have Si:Al ratios of 1.0–3.0, whereas mordenite has an Si:Al ratio of at least 5.0, making it suitable for acidic conditions [23].

Slansky et al. [26] found that silver mordenite (AgZ) has an iodine capacity of about 60 mg/g at 100 °C with 150 ppm iodine and dry air as the carrier gas. Reducing silver mordenite with hydrogen, denoted by Ag°Z, increased its capacity to 119±2 mg/g. Interestingly, the addition

2% NO and NO_2 to the carrier gas decreased the capacity of Ag°Z to 113 mg/g, but 2% NO_2 decreased its capacity to 68 mg/g. This was speculated to be because NO_2 acts as a reductant to Ag, but the presence of NO curbs its reducing effect. Separately, Jubin [27] performed a wide series of tests to evaluate AgZ for methyl iodide capture, determining the effects of NO, NO_2, humidity, and temperature of the stream. AgZ exhibited high loading capacities of 139 mg/g for iodine and 23 mg/g for methyl iodide at 200 °C. He found that higher temperatures and humidity increased loading capacity of methyl iodide onto AgZ. Jubin attributes the effect of temperature the kinetic energy of the sorbate; the greater the kinetic energy, the deeper the sorbate can penetrate the sorbent and the more silver sites it can access. Recently, Patton et al. [28] synthesized a lower 9.5 wt% Ag°Z and tested its long-term use by aging it with NO for one week. They found that at 150 °C and a 50 ppm iodine inlet gas concentration, Ag°Z had a 7.19 wt% (70 mg/g) iodine sorption capacity, and aging the Ag°Z with NO decreased iodine capacity about half to 3.24 wt%. AgZ continues to be a sorbent of much interest for industrial application; thus, researchers have pursued a deeper understanding of the adsorption of iodine on AgZ. Nenoff et al. [29] attempted to better understand the reaction mechanism of methyl iodide with AgZ by performing X-ray diffraction and pair distribution function analysis on AgZ samples.They found that methyl iodide is actually cleaved, leaving I_2 or HI to bond with the silver sites, where it is physically and chemically bound. Alumina has also been the subject of silver impregnation studies because of its heat resistant properties. Cheng et al. [30] showed silver-impregnated alumina (AgA) to remove iodine better than unimpregnated alumina. Cheng et al. synthesized a 10 wt% AgA with a surface area of 107 m^2/g [30]. It exhibited only modest DFs of about 3.0, most likely attributable to a small sorbent bed and high iodine feed concentration used in their experiments. More importantly, DFs for AgA dropped by only 20% with a temperature increase from 100 °C to 650 °C, while DFs dropped almost 70% at the same temperatures for alumina. Fukasawa et al. [31] made a higher-loaded, 24 wt% AgA and tested it with a 750 ppm iodine feed at 150 °C, finding a 22 wt% capacity. The 24 wt% AgA exhibited DFs above 10^3 for bed depths greater than 5 cm, and DFs of the AgA increased with increasing feed concentration, temperature, and bed depth.

Silver-based adsorbents have many advantages: they bond strongly with iodine, immobilizing it, and they exhibit high iodine sorption capacities while retaining high removal efficiencies up to 500 °C. But perhaps the biggest disadvantage of silver-based adsorbents is their cost. For example, on a mass basis, silver Linde MS is twenty times the cost of AC. Their utility can outweigh

their cost, but only provided the sorbent is reused; however, the regeneration of silver sorbents must be done under the flow of pure hydrogen at 500 °C, which is difficult, expensive, and may not be permitted in nuclear reprocessing facilities for safety reasons [14, 27]. Additionally, much of the reaction mechanism between iodine and silver remains unknown [8].

1.4.3 Organic Resins and Chalcogels

Another class of sorbents proposed for iodine removal is organic resins. From as early as 1970, resins have been used for iodine sorption and have exhibited high capacities. Moore and Howerton [32] studied Amberlite XAD-2 through XAD-12 for iodine removal. The resins had iodine capacities as high as 209 mg/g with an iodine feed of 300 ppm at 21 °C, the same capacity as a silver zeolite tested in the same study. More recently, Sarri et al. [33] examined polyethylenimine-epichlorohydrin resins for iodine uptake from aqueous solutions finding greater than 500 mg/g capacity at low pH, but they also found that the performance was strongly affected by competing anions [33]. A separate study on Amberlyst A-27 also showed effective iodine sequestration, but, as with the polyethylenimine resin, lacked selectivity due to co-adsorbed ions competing with iodine [34]. This poor selectivity is one of the pitfalls of organic resins, as they tend to have a high affinity for organics. Impregnating organic resins with silver can improve selectivity. Decamp et al. made a silver impregnated CL resin, which captured iodine at 95 wt% [35]; however, silver impregnation does not prevent organic resins being affected detrimentally at high temperatures. At high temperatures, the thermal stability of organic resins is limited, and iodine capacities decrease precipitously above 50 °C [10]. For example, the iodine capacity of Amberlite XAD-12 decreased by 60% when temperatures were increased to 100 °C [32].

Chalcogen-based aerogels are currently being studied as an alternative to AgZ because they are a more efficient candidate for iodine waste forms. Silica aerogels were originally considered because they are a precursor to stable iodine waste forms, but they turn brittle after exposure to moisture. Instead, chalcogels are aerogels that contain S, Se, and Te anions, but not O as silica aerogels do. There are a wide range of chalcogel compositions because they can be formed from aggregations of binary crystals, or their structural units can be held together by metal ions such as Pt^{2+}[36–38]. Riley et al. [36] synthesized Pt-Ge-S chalcogels using two gel-casting techniques, plate- and cylindrical-casting. Iodine sorption on the chalcogels was performed in a vacuum desiccator at 6.7 Pa. They found that cylindrically-cast chalcogel, Cg-5C, had a large uptake

of iodine at 239 wt% [36]. Separate sorption experiments were performed with a flow of dry air containing 4 ppm iodine, where the same chalcogel had a 1.80 wt% capacity [36]. Subrahmanyam [38] found that ZnSnS and NiMoS chalcogels had capacities of up to 225 wt%. While chalcogels certainly exhibit high capacities, even higher than silver adsorbents, the rate of adsorption was very low in both studies; Riley's chalcogel taking 20 days to reach its maximum capacity. This low sorption rate does not scale well, requiring massive amounts of chalcogel to meet iodine removal requirements.

1.4.4 Metal-Organic Frameworks

Metal-organic frameworks (MOFs) are a new breed of porous material that has sparked much interest in their application to electronics, catalysis, biomedicine, chemical sensing, radiation detection, and gas separation and storage [39]. MOFs are crystalline frameworks with metal-cation joints and organic electron-donor limbs. This means hundreds of thousands of possible MOFs exist with unique pore sizes, shapes, surface area, and chemical functionalities. Their unique structure gives them a synthetic flexibility previously unseen in porous materials. Thus, they are being studied intensively for their application in adsorption processes. Sava et al. [40] developed the ZIF-8 and Cu-BTC (a.k.a. HKUST-1) MOFs for iodine capture. They found that both ZIF-8 and HKUST-1 were very promising; ZIF-8 had a 125 wt% capacity at 350 K and 0.014 atm iodine partial pressure, and HKUST-1 had a 175 wt% capacity at 350 K and 3.5% relative humidity. ZIF-8 was subsequently studied by Chapman et al. [41] for its immobilization properties. They annealed the iodine-loaded ZIF-8 at 398 K and applied 1.2 GPa of pressure to the powder in a pellet press to give it an enhanced durability, but they noted that high pressures could induce problematic responses in the ZIF-8.

1.5 Porous Sorbents for the Capture of ^{85}Kr

Sorption of noble gases is particularly difficult because they lack chemical reactivity, have low solubility, and have very low melting and boiling points. As with ^{129}I, AC has been a traditional sorbent for ^{85}Kr capture, and is used as a reference when testing new sorbent materials. [16, 42]

1.5.1 Carbon Nanotubes

Multi-walled carbon nanotubes (MWNTSs) were first discovered in 1991, and single-walled carbon nanotubes (SWNTs) two years later. Both have attracted much attention because of their unique thermal and structural stability. A study by Dillon et al. in 1997 sparked real interest in SWNTs when they found that significant amounts of H_2 adsorbed on SWNTs, with a binding energy substantially higher than that of planar graphite [43, 44]. Each study of SWNTs—experimental [44–46] and simulation [47, 48]—found stepwise adsorption isotherms attributable to gases adsorbing on the outer walls, interstitial channels, and inner channels of the nanotubes. Babaa et al. [45] demonstrated that opening the ends of SWNTs improved the adsorption of krypton and xenon while changing the nature of their respective isotherms. The krypton adsorption isotherms generated by Babaa [45] and Muris [46] are shown in Fig. 1.2.

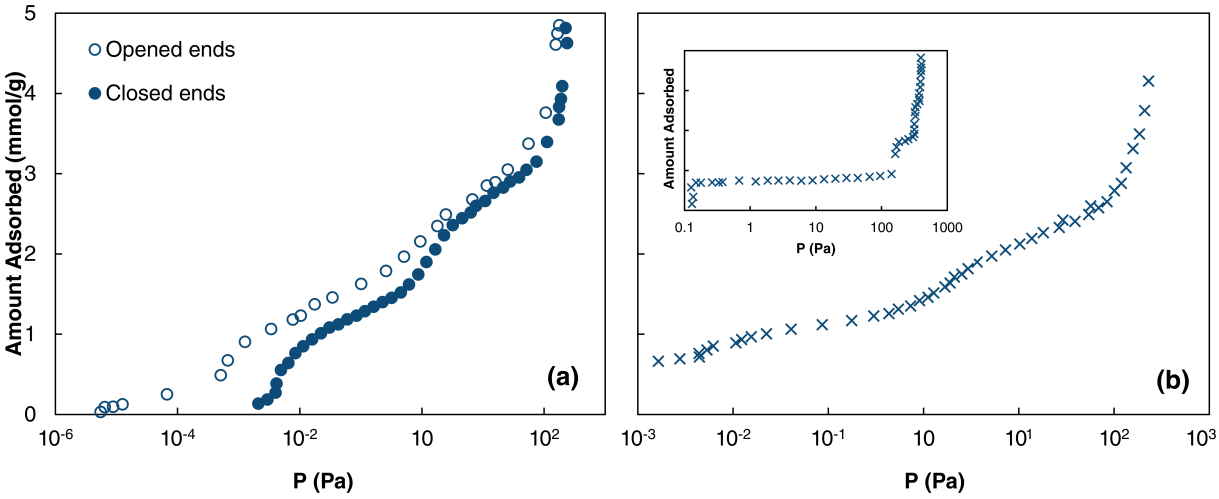

Figure 1.2: SWNT krypton adsorption isotherms. (a) Comparison of opened and closed SWNTs at 77 K [45] and (b) SWNTs at 77.3 K. The inset represents a krypton isotherm on graphite at 80 K [46].

Molecular dynamics simulations by Foroutan [47] and Jalili [48] showed that the unique geometry of SWNTs make them selective to noble gases when adsorbing mixtures of Ar, Kr, and Xe, and that temperature has a strong bearing on their effectiveness. This means that the operating pressure and temperature significantly affect the adsorption of nobles gases onto SWNTs, and predictive simulations are difficult. Table 1.2 lists krypton adsorption capacities for various carbon materials.

Table 1.2: Krypton sorption capacities for various carbon materials.

Sorbent	**SA (m^2/g)**	**T (K)**	**P_{Kr} (Pa)**	**q_{Kr} (mol/g)**	**Ref.**
Activated Carbon	-	298	1.0E+05	2.6E-03	[49]
Activated Charcoal	663	273	7.2E+00 1.2E+04	4.7E-03 4.1E-06	[50]
Ambersorb 563	-	273	1.6E+01 2.0E+03	7.6E-06 9.1E-04	[42]
Ambersorb 572	1100	273	3.1E+01 1.6E+02	2.3E-05 1.1E-04	[42]
SorboNorit B3	778-1012	303	4.7E+04 3.0E+06	5.8E-04 5.6E-03	[51]
Tsurumi-HC-30	1115	195 273	2.9E+00 4.4E+04 2.2E+01 5.9E+04	4.3E-06 5.0E-03 1.1E-06 1.3E-03	[52]
Takeda-G	1400	195 273	7.9E+00 5.3E+04 2.9E+01 7.5E+04	1.4E-05 5.3E-03 1.0E-06 1.3E-03	[52]
Takeda-L	1290	195 273	5.1E+00 4.5E+04 3.6E+01 6.9E+04	1.4E-05 5.5E-03 2.0E-06 1.6E-03	[52]
o-SWNT	-	77 93	6.7E+01 5.9E-01	3.4E-03 8.4E-04	[45]
SWNT	160-210	77.2	2.6E-02 1.8E+02	9.8E-05 4.1E-03	[46]

SA = surface area of sorbent.
P_{Kr} = partial pressure of krypton in equilibrium with sorbent.
o-SWNT = single-walled carbon nanotubes whose ends have been mechanically opened.

1.5.2 Zeolites

Zeolites have attracted a great interest in noble gas sorption due to their physical properties: high specific capacity, structural stability, and small pore size. Hydrogen mordenite (HZ) is a zeolite of interest for Kr removal because of its apparent high capacity. HZ is created by ion exchanging mordenite in HCl. Ianovski et al. [53] investigated HZ for Kr sorption and concluded that the adsorption capacity of HZ for Kr was about four times greater than Molecular Sieve 5A and two times higher than natural mordenite and comparable to AC at 195 K in helium carrier gas. The Kr adsorption capacity of HZ was enhanced by changing it into a large–pore type mordenite, removing extraneous materials in the mordernite channels, and increasing the surface area formed from the Si-O-Si bond by dealuminization. Garn et al. [54] have presented a more detailed study on HZ for the sorption of Kr. An important step in the process was the pelletization of HZ. Although the powder form of zeolites has higher surface area, using powder in an adsorption column leads to a large pressure drop. Pelletization of the powder reduces the pressure drop but at the expense of the sorbent's surface area. Garn et al. lessened the loss of surface area during pelletization by using a polymer binder to form HZ pellets of 336 m^2/g [54]. Though this is a decrease from the 500 m^2/g surface area of the raw HZ powder, it is a significant improvement over typical, commercial HZ pellets which have surface areas of 30–50 m^2/g. Garn et al. found that their HZ pellets had a sorbent capacity of 100 mmol/kg with an inlet off-gas concentration of 150 ppm krypton balanced with helium. The sorbent capacity is considered to be quite high. HZ was also shown to have high thermal stability, proving suitable for thermal regeneration cycles. However, the addition of Xe to the inlet gas at a concentration of 1000 ppm reduced the HZ Kr capacity to 7.41 mmol/kg. This problem can be avoided by using a second zeolite, AgZ, to trap Xe before the process gas is passed through the HZ column. In recent years, Daniel et al. [55] studied five commercially available zeolites loaded with silver, and obtained the Xe adsorption isotherms over a wide range of Xe partial pressures. Increasing the Ag loading showed a direct correlation to an increase in the number of strong adsorption sites located on the exterior of the porous zeolites. This increase in strong bonding sites improves adsorption at lower pressures. The experimentally observed capacities were quite good: at 303 K and 100 ppm Xe, Ag-PZ2-25 had a capacity of 5×10^{-4} mol/g, whereas the traditionally-used AC had a capacity of 4.3×10^{-6} mol/g.

1.6 Separation of Kr and Xe

Though Xe isn't a radioactive concern, it has a chemistry similar to Kr and is more polarizable—thus, more reactive in many cases—and is present at about 10 times the concentration of Kr in off-gas. Consequently, when Xe is not separated from Kr, Kr and Xe compete for available active sites, more sorbent is needed to remove Kr, and the overall volume of high-level waste increases significantly. A few multicomponent adsorption studies have been done with Kr and Xe [49, 54, 56, 57] as well as pure Kr and Xe adsorption comparisons [39, 45, 51, 52, 58]. Some zeolites, such as NaA and NaX have shown selectivities of four to six but have low capacities [59].

Separation of Kr and Xe is a task well-suited for MOFs because the wide variety available. However, the sheer number of possible MOF structures numbers into the hundreds of thousands, and it is not feasible for experimentalists to systematically study them all. For this reason, computational screening using Grand Canonical Monte Carlo (GCMC) simulations has gained momentum for screening existing and hypothetical MOF structures. Sikora et al. [60] used high-throughput GCMC simulations to determine which properties of over 137,000 MOFs affected Kr/Xe selectivities. Selectivity is a measure of the affinity of the sorbent for one component of a mixture, and it is shown by the equation below;

$$S_{AB} = \frac{x_A/y_A}{x_B/y_B} \tag{1.9}$$

where x is the absorbed phase concentration, and y is the gas phase concentration of components A and B. Sikora's results confirmed that pore size and shape play an important role in MOF-adsorbate interactions [60]. MOFs with the highest Xe/Kr selectivity typically had long, tube-like pores with diameters close to the kinetic diameter of Xe. Ryan et al. [61] screened prominent MOFs computationally as well and emphasized the need to balance optimal pore size and selectivity. MOFs with larger surface area exhibited higher capacities and lower selectivity.

Two of the first benchmark MOFs for Xe/Kr adsorption were HKUST-1 and Ni/DOBDC (MOF-74). Mueller and coworkers [57] were among the first to experimentally determine the behavior of MOFs for Kr/Xe separation. They found that IRMOF-1 and HKUST-1 both showed a significant selectivity for Xe [57]. A deeper investigation of both Ni/DOBDC and HKUST-1 by Liu et al. [49] found that with 1000 ppm inlet concentrations of Kr or Xe, Ni/DOBDC had Kr and

Xe capacities of 1.8 and 9.3 mmol/kg, respectively, and HKUST-1 had Kr and Xe capacities of 2.0 and 8.5 mmol/kg, respectively. Later, Liu et al. studied the effect of adding silver to Ni/DOBDC and found that silver increased the Xe/Kr selectivity of Ni/DOBDC from 5.3 to 9.5 [62]. One other notable MOF for Xe/Kr separation is FMOFCu, a partially fluorinated MOF synthesized by Fernandez et al. [63]. FMOFCu exhibited a huge Kr/Xe selectivity of 36 at 0.1 bar and 203 K. FMOFCu has been the only MOF to preferentially adsorb Kr over Xe [63].

1.7 Engelhard titanosilicate 10 & Hollow Carbon Nano-polyhedrons

The difficulty of honing in on a sorbent that is both effective at iodine and krypton capture and economic has motivated our research. We have developed an Engelhard titanosilicate 10 (ETS-10) supported hollow carbon nano-polyhedron sorbent for iodine and krypton sorption.

We chose to use hollow carbon nano-polyhedrons (HCNPHs), discovered by Zhu et al. [64], as the principal adsorbent because carbon nanomaterials have shown promise for the adsorption of both iodine and krypton and have a high chemical and thermal stability. However, the large-scale synthesis of carbon nanotubes is difficult; methods of carbon nanotubes include arc discharge, laser vaporization of graphite rods, and chemical vapor deposition in fluidized bed reactors. Conversely, HCNPHs were chosen because they can be produced on a large-scale in batch reactors. Similar to MWNTs but polyhedron shaped instead of cylindrical, the HCNPHs are loose and tend to agglomerate; this makes HCNPHs difficult to pelletize and less surface area available when agglomeration occurs, hindering adsorption. For this reason, we chose to support the HCNPHs on the surface of Engelhard titanosilicate 10 (ETS-10).

Engelhard titanosilicate 10 is a zeolitic-type material with potential applications as a catalyst [65], a dessicant [66, 67], and an adsorbent [68–72]. It was first synthesized by Kuznicki et al. in 1989 [73], and its detailed structure was proposed in 1995 by Anderson et al. [74] as corner sharing SiO_4 tetrahedra and TiO_6 octahedra. Titania chains composed of TiO_6 run through the crystal, linked by 12-, seven-, and five-membered SiO_4 rings. The apertures of these rings define the pores of ETS-10 and are illustrated in Fig 1.3. This unique structure framed by TiO_6 is what gives ETS-10 its high surface area and structural resilience. However, all titanosilicates share the same functional groups and bonds as ETS-10, which rouses the question—what makes ETS-10 unique? Of the Engelhard titanosilicates, ETS-4 and ETS-10 have attracted the most attention from scientists because they have shown the most promise as adsorbents [75].

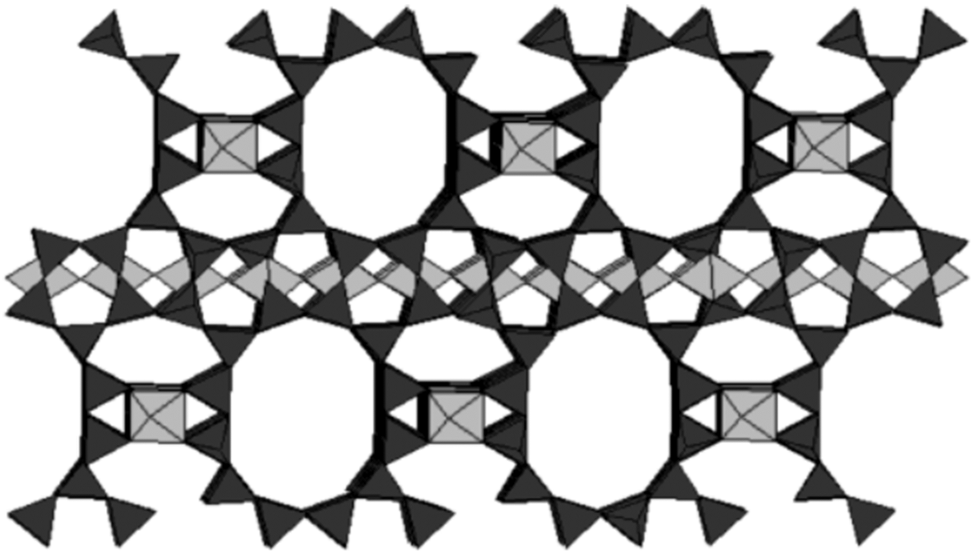

Figure 1.3: Illustrated structure of ETS-10. TiO_6 groups are shown in grey, SiO_4 groups in black.

ETS-10 is resistant to radiation and this is important to its usefulness for long term radionuclide storage once radionuclides have been adsorbed upon its surface, and ETS-10 has been studied for the removal of radionuclides showing high adsorption capacities for heavy metals [68]. ETS-10 sets itself apart from zeolites because of its durability under acidic conditions that progressively damages most zeolites. Its silica pore walls are hydrophobic, so ETS-10 has an advantage in humid off-gas conditions. The water adsorption of zeolites typically only decreases 30% from 25 to 100 °C, but Tanchuk et al. found the water adsorption of ETS-10 to drop a full order of magnitude between 25 and 100 °C [67]. Additionally, its thermal stability up to 600 °C, 8 Å pore size and a high surface area lend themselves well to application in nuclear reprocessing off-gas conditions.

Like zeolites, ETS-10 has extraframework sodium cations that can be ion-exchanged to impregnate the ETS-10 with silver, and this has been done by Ansön et al. to study the adsorption of nitrogen, argon, and oxygen [71] on silver-impregnated ETS-10. 30 wt% Ag on ETS-10 (Ag@ETS-10) exhibited comparable sorption capacities to AgZ for each gas. Though Ansön et al. did not study the sorption of krypton on silver-impregnated ETS-10, they did study the sorption of argon which is similar to krypton. Furthermore, previous studies by Liu et al. and Perry et al. [39, 49] showed that argon adsorbed to various zeolites and MOFs at proportionally lower amounts than krypton and xenon. Thus, it is not unreasonable to assume that Ag@ETS-10 would also have a similar capacity for krypton as the AgZ counterpart. Further studies of xenon adsorp-

tion by Kuznicki et al. [72] compared Na@ETS-10 (the natural state of ETS-10) to Ag@ETS-10, and showed that the addition of silver more than doubled the titanosilicate's capacity for xenon. Wu et al. performed static iodine adsorption on Ag@ETS-10 by placing the sorbent in a closed chamber with iodine crystals at 80 °C [76]. Wu et al. compared Ag@ETS-10 to Na@ETS-10, recording sorption capacities of the ETS-10 after heating the saturated sorbent at 100 °C for 24 hours to confirm chemisorbed iodine only. Regardless, significant amounts of iodine were retained—22.2 and 3.3 wt% iodine on Ag@ETS-10 and Na@ETS-10, respectively.

The procedures for synthesizing the HCNPHs, ETS-10, and the HCNPH/ETS-10 sorbent as well as the characterization of all materials are detailed in the next chapter.

Chapter 2: Synthesis & Characterization of C/ETS-10

2.1 Sorbent Synthesis

2.1.1 Hollow Carbon Nano-Polyhedrons Synthesis

The hollow carbon nano-polyhedrons are synthesized using the method reported by Zhu et al. [64]. A 2:1 stoichiometric ratio of calcium carbide (CaC_2) to nickel dichloride hexahydrate ($NiCl_2{\cdot}6H_2O$) is powderized, mixed well, and reacted in a temperature-controlled 316 stainless steel autoclave at 250 °C for 5 hours. The product is a solid mixture containing top and bottom layer. A diagram of this process is shown in Fig. 2.1. The top-layer product contains the HC-

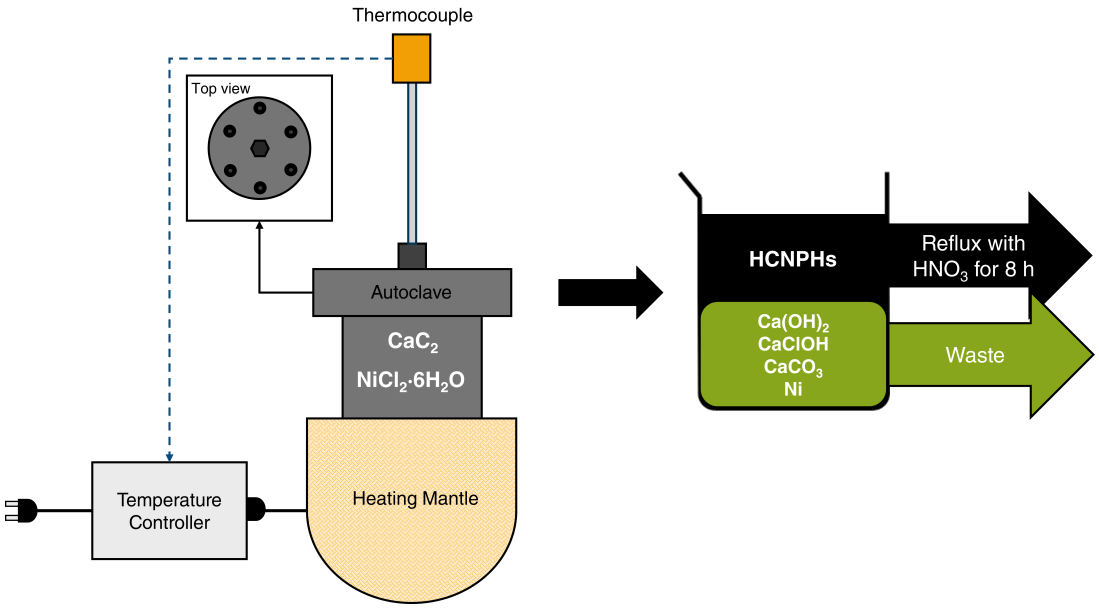

Figure 2.1: Diagram of the synthesis of HCNPHs

NPHs and is a dark black, loose, cotton-like substance, while the bottom-layer is a hard, sandy

material. Zhu tentatively proposes the reaction mechanism as:

$$CaC_2 + 2H_2O \rightarrow Ca(OH)_2 + C_2H_2 \tag{2.1}$$

$$NiCl_2 + C_2H_2 \rightarrow Ni + 2C + 2HCl \tag{2.2}$$

$$C_2H_2 \rightarrow 2C + H_2 \tag{2.3}$$

$$2HCl + Ca(OH)_2 \rightarrow CaCl_2 + 2H_2O \tag{2.4}$$

The overall reaction is:

$$4CaC_2 + NiCl_2 \cdot 6H_2O \rightarrow 3Ca(OH)_2 + 8C + Ni + CaCl_2 + H_2 \tag{2.5}$$

The important step is given in Equation 2.2, where Ni nanoparticles are formed. Once the Ni nanoparticles are formed, Zhu submits that the carbon graphitizes upon them in successive layers [64]. This proposed mechanism is reasonable because Ni is known to catalyze the pyrolysis of C_2H_2 (Equation 2.2) and the ordering of carbon nanomaterials [77]. The Ni nanoparticle at the center of the synthesized HCNPHs is removed by refluxing the top-layer product in nitric acid for 8 hours to remove the Ni. The product is dried for 12 hours at 180 °C, after which it can be characterized.

2.1.2 Engelhard Titanosilcate 10 Synthesis

We synthesized ETS-10 by using the hydrothermal method reported by Yang et al. [78], in which crystals are grown from an aqueous solution at a high temperature. First, we mix 80 g of sodium silicate with 140 mL of deionized water, then subsequently add 27 g NaCl, 5.2 g KCl, and 5.2 g TiO_2. A thick, white paste results which we transfer to the same type of autoclave as used for HCNPH synthesis (Fig. 2.1). The autoclave is then heated to 200 °C and held at that temperature for 42 hours. ETS-10 results and is a hard, white substance that we remove from the autoclave and rinse with deionized water under vacuum filtration. It is then put in an oven to dry at 180 °C for 12 hours. Once the ETS-10 is dry, we grind it to a fine powder using a ceramic mortar and pestle to facilitate the dispersion of HCNPHs onto its surface.

2.1.3 C/ETS-10 Sorbent Synthesis

When synthesizing sorbent, our objective is to disperse the HCNPHs evenly on the surface of ETS-10, creating a HCNPH/ETS-10 powder. Next, we want to form a pellet from the HCNPH/ETS-10 powder that retains as much of the surface area and pore size as possible. To disperse the HCNPHs on ETS-10, HCNPHs are put into tetrahydrofuran (THF), and the solution is sonicated for 30 minutes. Then, ETS-10 is added to the THF mixture which is stirred for 12 hours and the THF is evaporated. A gray powder results that we heat at 180 °C for 12 hours.

The HCNPH/ETS-10 powder, which will be denoted as C/ETS-10 from now on, is formed into pellets by adding a 1:1 mass ratio of C/ETS-10 powder to Ludox HS-40 colloidal silica to bind the powder. The paste that forms is put into an extrusion press, forming 1/8" diameter cylindrical pellets of varying lengths. C/ETS-10 pellets were made from 3 to 30 wt% HCNPHs on ETS-10 by changing the ratio of carbon to ETS-10 in the THF solution.

2.2 Characterization

The synthesized HCNPHs, ETS-10, and C/ETS-10 sorbent were characterized through various methods better understand their structure and properties. These methods and the theory behind them is discussed in the following sections.

2.2.1 Scanning & Transmission Electron Microscopy

Scanning electron microscopy (SEM) and transmission electron microscopy (TEM) use electron scattering to view materials on a much smaller scale than what is allowed by traditional microscopes. SEM focuses a narrow electron beam at low voltage on a material sample and creates an image from the electrons reflected back to a sensor, while TEM uses a broader higher voltage electron beam that penetrates the sample to image layers. SEM images of the samples were taken with a LEO SUPRA 35VP field emission-scanning electron microscope, and TEM images were taken using a JEOL JEM-2100 high-resolution transmisson electron microscope at 200 kV to provide a 0.27 nm resolution.

From the SEM image of ETS-10 in Fig. 2.2a, we see the characteristic square truncated bipyramidal crystals of ETS-10; identifiable crystals formed of 400–500 nm in length. Fig. 2.2b shows that the C/ETS-10 sorbent has a uniform surface, confirming that the HCNPHs are evenly

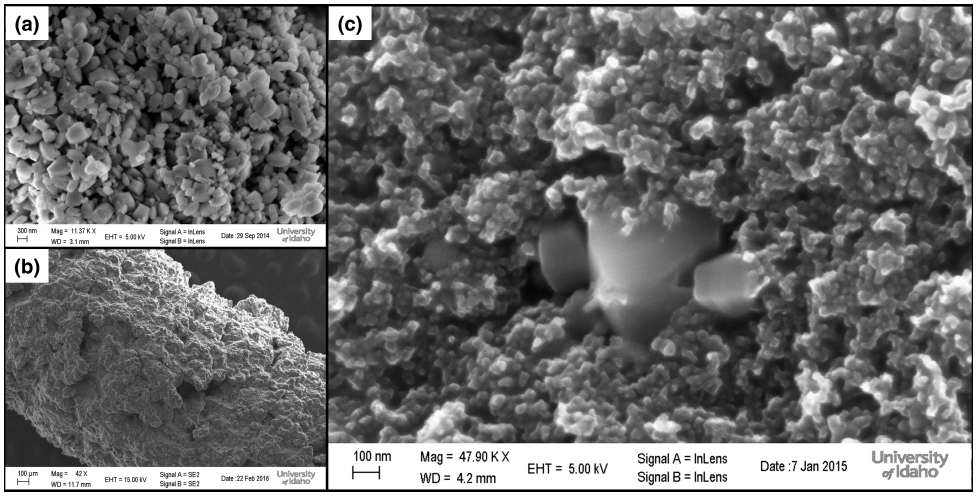

Figure 2.2: SEM of synthesized (a) ETS-10, and the (b) 10 wt% C/ETS-10 sorbent at 42X magnification, and (c) 10 wt% C/ETS-10 at 47.9 KX magnification.

distributed on the surface of ETS-10. This was further confirmed by the higher magnification image in Fig. 2.2c; this image also shows the HCNPHs—small aggregates around the center ETS-10 crystal—to have a uniform width of 50–70 nm. Fig. 2.3 shows the TEM images of ETS-10, HC-

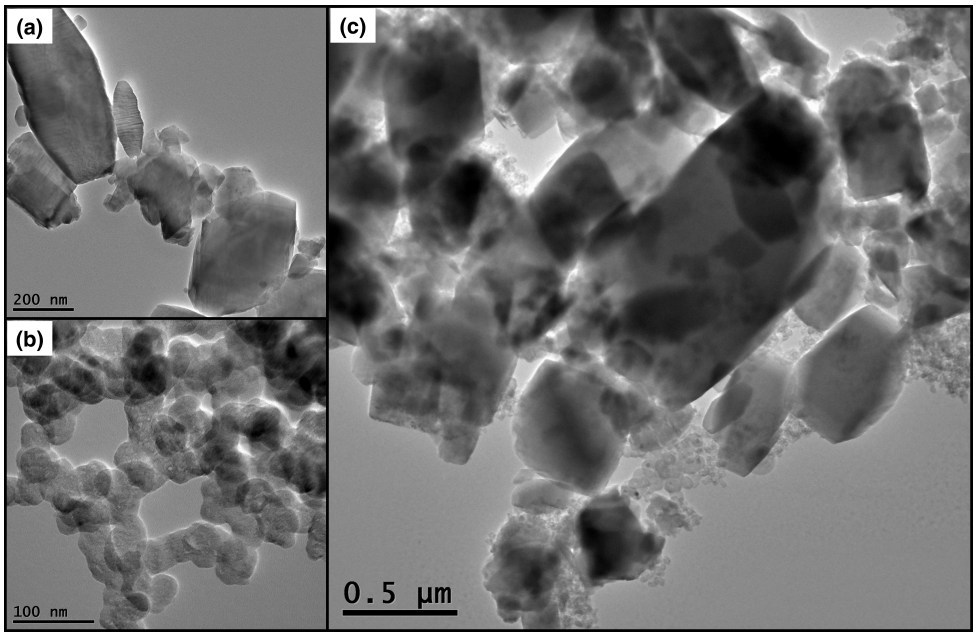

Figure 2.3: TEM of synthesized (a) ETS-10, (b) HCNPHs, and (c) 10 wt% C/ETS-10 sorbent.

NPHs, and the C/ETS-10 sorbent. The TEM image of the HCNPHs shown in Fig 2.3b illustrates that the HCNPHs tend to agglomerate, shown by dark patches which represent overlapping material; however, when dispersed on to ETS-10 (Fig. 2.3c), this agglomeration is controlled since

the patches of carbon, shown by small sandy looking patches, overlap less frequently. It is possible that this is because the Na^+ ions on the ETS-10 surface influence the position of the carbon.

2.2.2 BET Surface Area

BET surface area analysis of the C/ETS-10 samples was carried out at 77 K on a Tristar III 3020 Micromeritics analyzer. Before BET isotherms were taken, the samples were outgassed at 300 °C for 3 hr under vacuum in the degas port of the analyzer. Table 2.1 shows the BET surface areas of the samples. The synthesized HCNPHs have a surface area of 70 m^2/g, and ETS-10 has a surface

Table 2.1: BET surfaces areas of sorbent materials

Material	BET Surface Area (m^2/g)
Activated Carbon	882
HCNPHs	70
ETS-10	242
5 wt% C/ETS-10	118
10 wt% C/ETS-10	149
20 wt% C/ETS-10	145
30 wt% C/ETS-10	76

area of 242 m^2/g. Depositing HCNPHs onto ETS-10 and pelletizing the resulting powder yields surface area values between that of raw HCNPHs and ETS-10. C/ETS-10 had different BET surface areas for each carbon loading with 10 wt% loading having the highest surface area of 149 m^2/g. We hypothesize that this is due to the HCNPHs agglomerating and/or blocking the pores of the ETS-10 at higher loadings.

2.2.3 Raman Spectroscopy

When a beam of light collides with a molecule, a portion of its photons lose energy and are scattered back away from the molecule with a longer wavelength (lower energy). This phenomenon is known as Raman scattering, or inelastic scattering. Raman spectroscopy capitalizes on this property by illuminating a sample with monochromatic light and measuring the scattered photons to identify molecules based on their characteristic scattering spectra or how the wavelengths of the photons are 'shifted'. We collected the Raman spectra for all of our samples using a WITewc alpha 300 Raman microscope with an incident beam of 532 nm.

Raman spectroscopy lends itself particularly well to the characterization of carbon materi-

als because the inelastic scattering of photons that occurs during Raman spectroscopy is quite sensitive to the non-polar covalent bonds between carbon atoms [79]. Determining the specific structure of carbon on the nanoscale is difficult because of the numerous forms it may take, but characterization can help specify its structure. It is first necessary to understand the characterization of graphene, because it is the building block for all other carbon structures [80]. Strictly speaking, graphene consists of a sp^2 hybridized carbon atoms in a beehive-type structure that is one atom thick. Understanding the Raman spectra of carbon materials requires knowledge of two basic Raman shifts: the G (graphite) and the D (defect) bands, which occur due to sp^2 hybridized carbon and disorder in carbonaceous structures, respectively. Fig. 2.4 compares the Raman spectra of diamond and graphite on a silicon substrate. The diamond band at 1332 cm^{-1} is attributable to the sp^3 hybridized carbon. The G band for graphite at 1582 cm^{-1} is also due to structured carbon, but it has been shifted because sp^2 hybridized carbon bonds are stronger and cause a larger shift in wavelength. There is also a G' (or 2D) band labeled at ~2700 cm^{-1} that is typical of graphene sheets, but it shows up in the Raman spectra of graphite as well because graphite is essentially stacked graphene. SWNTs also have a similar Raman spectrum to

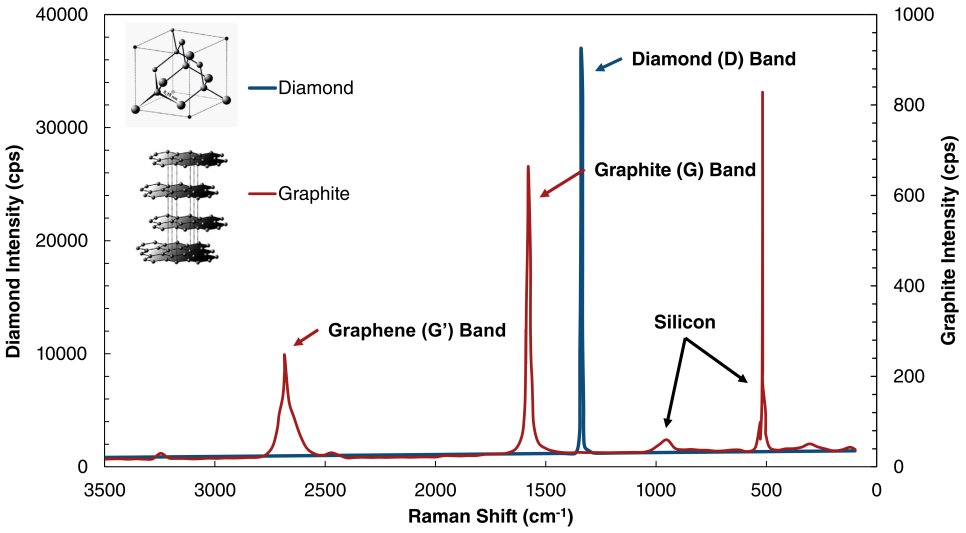

Figure 2.4: Raman spectra of diamond and graphite reproduced from [79]

graphene because SWNTs are graphene sheets rolled into a cylinders. However, they also include the D band shown in Fig. 2.5. The D band originates from bonds associated with graphene edges and represents disorder or defects in the carbon structures. The D band's intensity relative

to the G band is used as a measure of nanotube quality. MWNTs exhibit higher D/G band ratios because the multiple layers add disorder to the structure. The series of peaks in at the low end of the spectrum in Fig. 2.5 correspond to the expansion and contraction of the tubes; this region is accordingly named the Radial Breathing Mode (RBM). Knowing this, we can look at the Raman

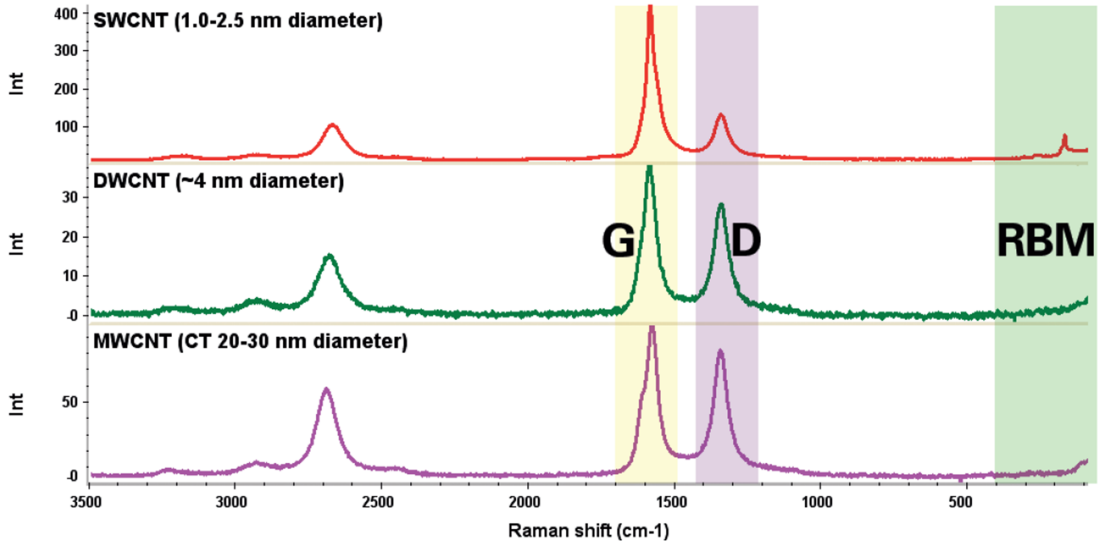

Figure 2.5: Raman spectra of carbon nanotubes from [79].

spectrum of our own synthesized HCNPHs in Fig. 2.6. There are peaks at 1328 cm^{-1} and 1569 cm^{-1} that correspond to the D and G bands, respectively. The presence of these two bands are indicative of a MWNT-like structure, the high D/G band ratio showing that it is multi-walled. The graphene band at 2700 cm^{-1} further confirms that these are graphene-based structures.

ETS-10 is one of many titanosilcates with similar functional groups, so it has a Raman spectrum that needs to be distinguished among others in the ETS family. The Ti-O-Ti bond stretching in TiO_6 groups appears in Raman spectra anywhere between 700–800 cm^{-1}. Su et al. [81] narrowed the Ti-O-Ti stretching in titania-linked chains (characteristic of ETS-10) to ~750 cm^{-1}. ETS-10 specifically exhibits a strong Raman shift at 723 cm^{-1}, and this is observed in the Raman spectra of the synthesized ETS-10 (Fig. 2.7). The weaker peak occurrences from 300–400 cm^{-1} are slightly more difficult to identify, but have been attributed to Si-O-Si and Ti-O-Ti fragments near defects by Southon [82]. The peak at 636 cm^{-1} has been attributed to Ti-O-Ti vibration by Su et al. [81]. Fig. 2.8 shows comparison of the Raman spectra of ETS-10, HCNPHs, and 10 wt% C/ETS-10. The characteristic Raman markers of HCNPHs and ETS-10 are seen in the Raman spectrum for 10 wt% C/ETS-10. However, the intensities of each shift were much lower,

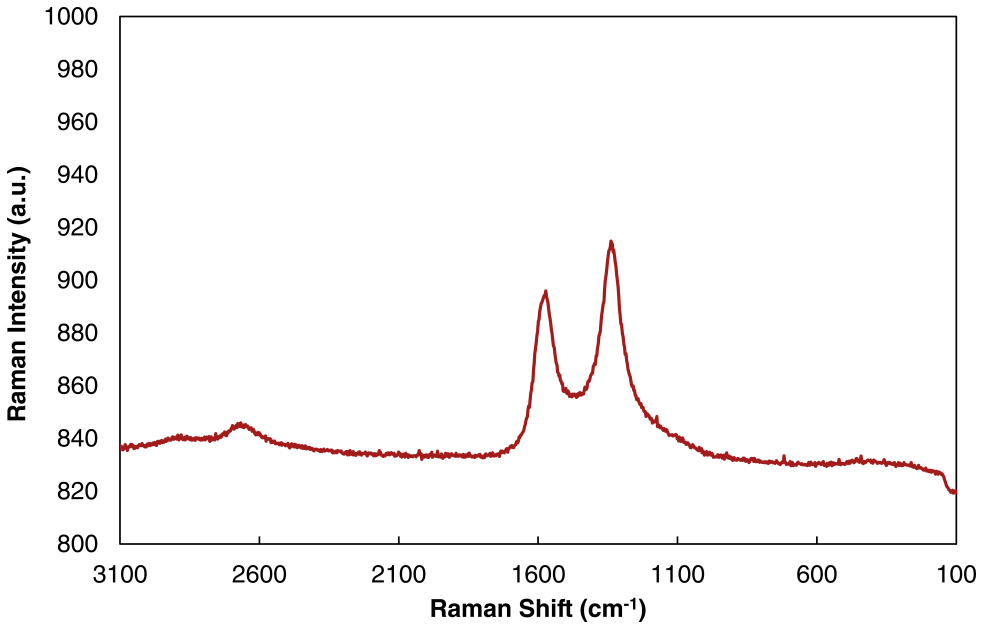

Figure 2.6: Raman spectrum of the synthesized HCNPHs

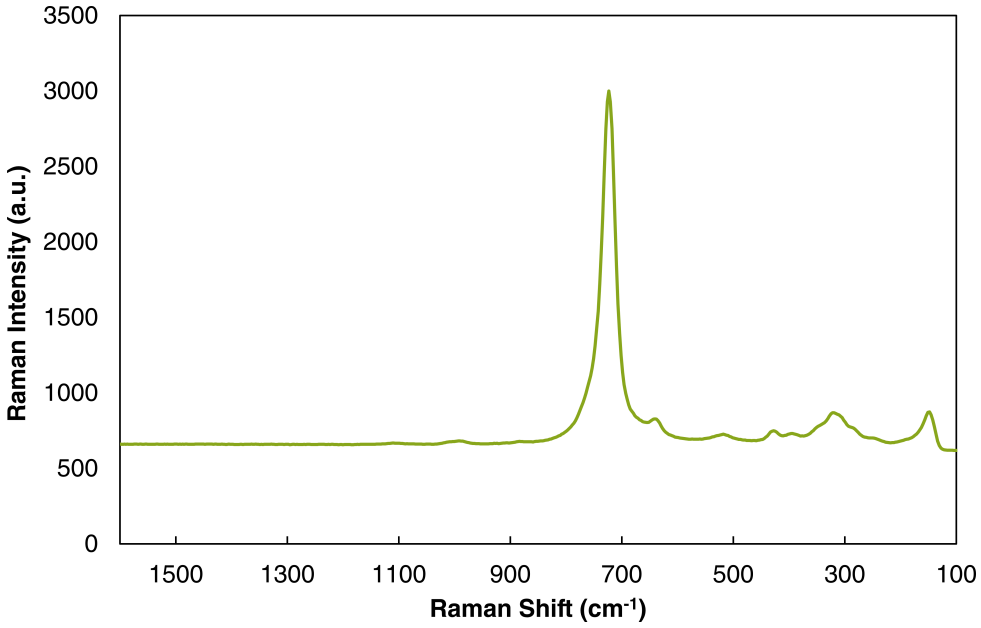

Figure 2.7: Raman spectra of the synthesized ETS-10

indicating a uniform dispersion of the HCNPHs onto the surface of ETS-10.

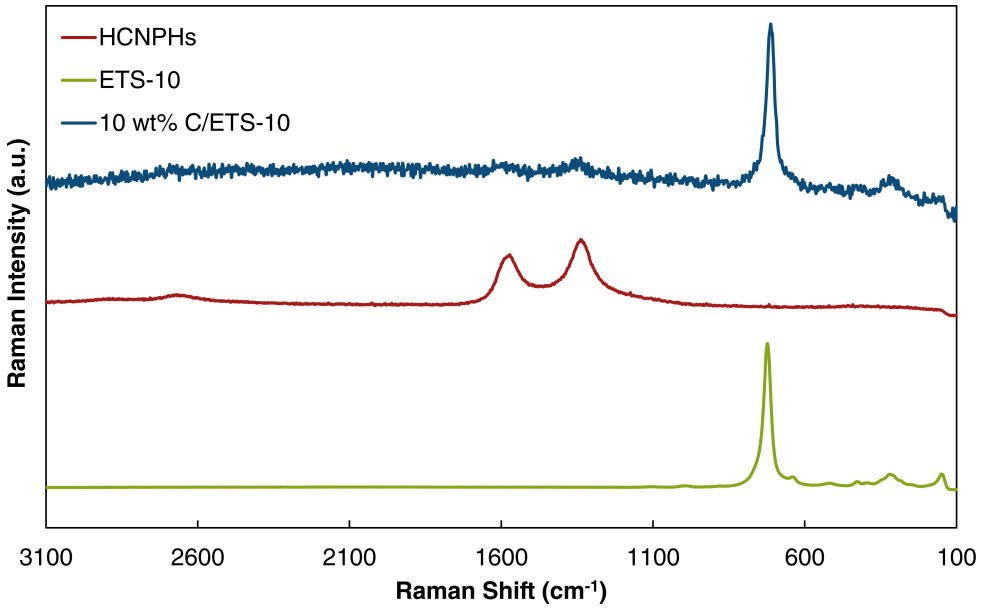

Figure 2.8: Comparison of the Raman spectra of HCNPHs, ETS-10, and 10 wt% C/ETS-10

2.2.4 X-ray Diffraction

Crystalline structure faces are diffraction gratings, which means they diffract X-rays directed at them predictably. In X-ray diffraction characterization (XRD), X-rays of a single wavelength are directed at a sample. If the sample is crystalline, its faces will constructively diffract the X-rays toward a detector. XRD works by directing the X-rays toward a sample over a range of 2θ angles to detect all crystalline faces. If a material has any crystalline order, it will appear on an XRD pattern as a defined peak. Overall, XRD is mainly used to characterize the unit cells of crystalline structures, or, in our case to confirm the identity of materials. We performed XRD on the synthesized materials using a Bruker D5000 diffractometer and Cu Kα radiation at 40kV and 30 mA at a scanning rate of 5°/min.

The XRD of the HCNPHs in Fig. 2.9 shows two main peaks at 2θ = 25.2°and 43.5°. These correspond to the 002 and 101 planes of hexagonal carbon. The peaks appear broad and slightly noisy because of long range disorder in the bulk of the HCNPHs. Because these are the only two peaks exhibited, the sample of HCNPHs has a high purity. In the XRD of ETS-10, many well-defined peaks can been seen between 2θ = 24.65°–27.5°; this shows that the ETS-10 has an overall high degree of crystallinity. The other peaks at 5.9°, 12.3°, 20.1°, 29.9°, 31.7°, and 35.6°match well with the XRD patterns of ETS-10 reported in literature [74, 78, 83, 84].

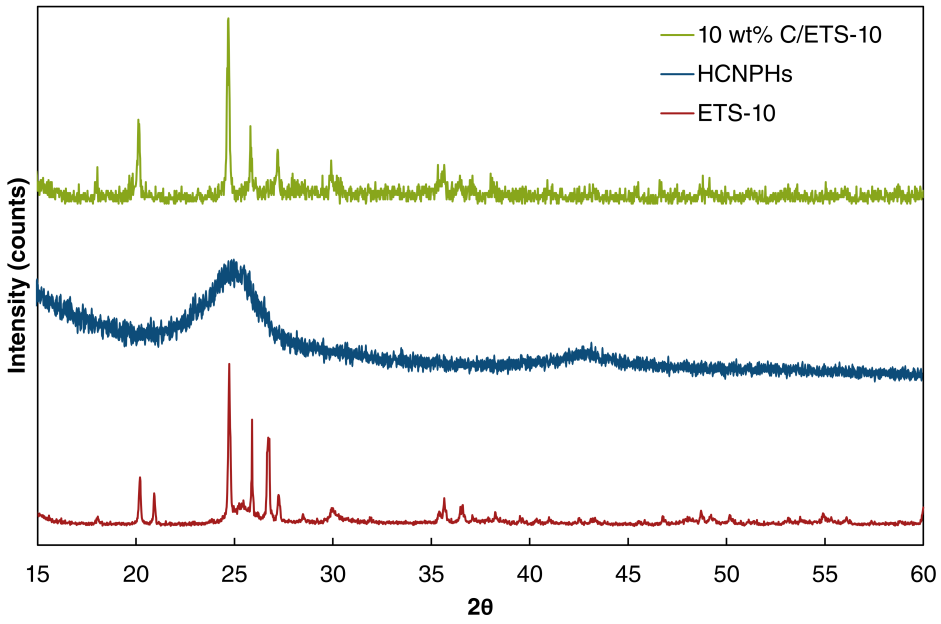

Figure 2.9: XRD comparison of synthesized materials

The remainder of this thesis focuses on the results of the single component (Chapter 3) and multicomponent (Chapter 4) adsorption experiments performed on the C/ETS-10 sorbent and the model derived to predict adsorption equilibria, which is discussed in Chapter 5.

Chapter 3: Single Component Adsorption Studies

3.1 Materials & Methods

Performing single component adsorption experiments is necessary to understanding the affinity of the C/ETS-10 sorbent for iodine and krypton. Results can be used to benchmark sorbents as well as to understand the mechanisms behind adsorption without the results being convoluted by competitive adsorption. Hence, we performed single component adsorption experiments of iodine and krypton while varying the carbon loading on ETS-10, empty bed contact time, and temperature to find optimal conditions for adsorption. Thermogravimetric analysis (TGA), energy-dispersive X-ray spectroscopy (EDS), SEM, TEM, and XRD were used to confirm the presence of iodine or krypton on the surface of C/ETS-10 and to characterize sorbent used for iodine adsorption.

For single component studies, two separate types of experiments were performed: iodine adsorption, and krypton adsorption. The iodine experiments used off-gas of 25±3 ppm iodine balanced with nitrogen, and krypton experiments used 70±5 ppm krypton balanced with nitrogen off-gas. The total off-gas flow rate was kept at 180±1 SCCM for all experiments.

In our experimental design, we perform adsorption experiments by flowing simulated off-gas consisting of iodine or krypton balanced with nitrogen through an adsorption column charged with 1–4 g of sorbent. The column is made of borosilicate glass, is 1 inch in diameter, and is water-jacketed to control the temperature at which each experiment is performed. The off-gas is primarily made of ultra-high purity (UHP) nitrogen procured from AirGas, and flow is contained in piping of 316 stainless steel, borosilicate glass, and Viton fluoroelastomer tubing. Viton and glass tubings are used to avoid setup corrosion from iodine. Gate valves are installed throughout the piping for diverting flow to add iodine and krypton and for sampling purposes. To add iodine to the off-gas, the UHP nitrogen from the gas cylinder is split into two streams, a large (150–170 SCCM) and small (10–30 SCCM) stream, each passing through an Aalborg mass flow controller (MFC). The small stream of nitrogen is passed through a water-jacketed iodine vaporizer at at 40±2 °C. The vaporizer initially contains 3±0.1 g of elemental iodine crystals

that are heated and partially vaporize, allowing the gas flowing through the vaporizer to carry the iodine and combine with the larger flow of nitrogen. Krypton is added by passing 1000 ppm of krypton balance with nitrogen (AirGas) through an MFC and merging it with the larger nitrogen flow as is illustrated in Fig. 3.1.

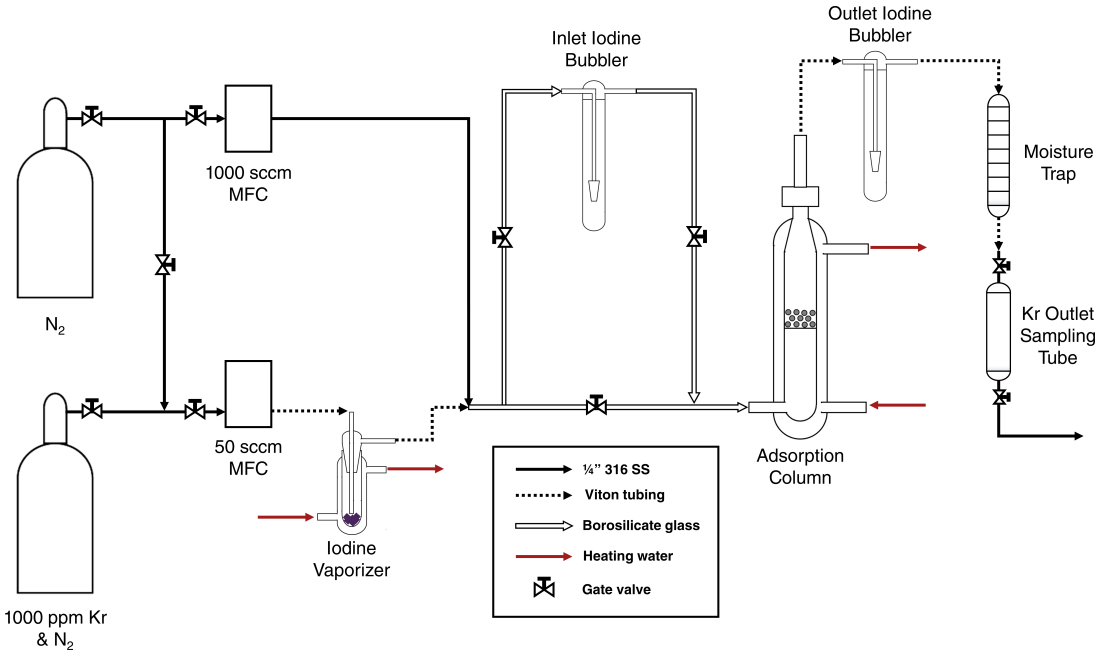

Figure 3.1: Experimental setup for iodine and krypton adsorption

3.1.1 Stream Concentration Analysis

The concentration of iodine and krypton in the inlet and outlet streams to/from the column was recorded throughout the duration of adsorption experiments, and it is used to find the sorption capacity of the adsorbent through Eq. 3.1.

$$q_i = Q \int_0^{t_f} \frac{(C_{i0} - C_{ie})}{M} dt \tag{3.1}$$

Here, q_i is the sorption capacity of the sorbent for contaminant i. Q is the volumetric flow rate of the off-gas flowing through the column, C_{i0} is the inlet concentration of contaminant i, C_{ie} is the outlet concentration of contaminant i. t_f is the exhaustion time, or time when $C_{i0} = C_{ie}$.The maximum uptake of the contaminant on the sorbent occurs at the beginning of the experiment when the sorbent has no contaminant on its surface. The outlet concentration of the column

increases until the sorbent is saturated at t_f, when the outlet and inlet concentrations are equal.

Iodine concentration in the gas stream was sampled by sparging the gas through milli-q water-filled bubblers, capturing the iodine in the water. We then measured the concentration of iodine in the water using the Leuco Crystal Violet (LCV) method as described in [85]. The LCV solution turns aqueous iodine solutions a dark purple color. The absorbance of the iodine solution follows Beer's Law, and it is proportional to the iodine concentration. Absorbance measurements were taken at 592 nm with a Thermo Scientific Evolution 60S UV-Vis spectrophotometer, then iodine solution concentration was found by using a LCV method calibration curve to relate absorbance to the iodine solution concentration; finally, the gas stream concentration of iodine was calculated from the total amount of iodine and off-gas sparged through solution.

We verified the accuracy of sampling iodine concentration using the bubbling technique by adding adding milli-q water-filled bubblers in series and passing the iodine-contaminated nitrogen through them, and measured the concentration of each by LCV. This confirmed that all the iodine was captured by the water in the first bubbler. The volume of water in the bubblers and bubbling times were also varied to ensure that this sampling method accurately reflected the gas stream concentration of iodine. Off-gas flow was diverted from the adsorption column when taking iodine samples to avoid moisture adsorption on the sorbent.

Kr concentration was taken by analyzing gas stream samples in a gas chromatograph (GC, Hewlett-Packard 6890 series) equipped with a CP-Molsieve 5 Å 25 m $\times$ 0.25 mm $\times$ 30 mm capillary column with a mass selective detector. The temperature of the GC column was initially kept at 100 °C for 5 min, was then increased at a rate of 30 °C/min until it reached 200 °C, and was then held at 200 °for 1 min. Helium at a flow of 1 mL/min was used as the GC carrier gas.

3.2 Single Component Adsorption Results

The outlet concentration from the adsorption column was taken for the duration of the adsorption experiments for both iodine and krypton single component experiments. The outlet concentration normalized by the inlet concentration, denoted by C/C_0, and plotted against time in the breakthrough (BT) curves shown in Fig. 3.6. Third-order polynomials were fit to the BT curves to find a function for outlet concentration as a function of time; R^2 values for the polynomial fits were above 0.98. The polynomial equations were substituted into Eq. 3.1 to find sorbent capacity, q_i.

3.2.1 *Effect of HCNPH Loading*

The first parameter we studied was the effect of carbon (HCNPH) loading on the iodine and krypton removal capacities. Results are shown in Fig. 3.2. For the carbon loading experiments, iodine sorption was performed with 25 ppm iodine in nitrogen at 20 °C, and krypton sorption experiments were done with 70 ppm krypton and nitrogen at -10 °C. We performed each experiment with one gram of sorbent in the column. We observe both krypton and iodine uptake

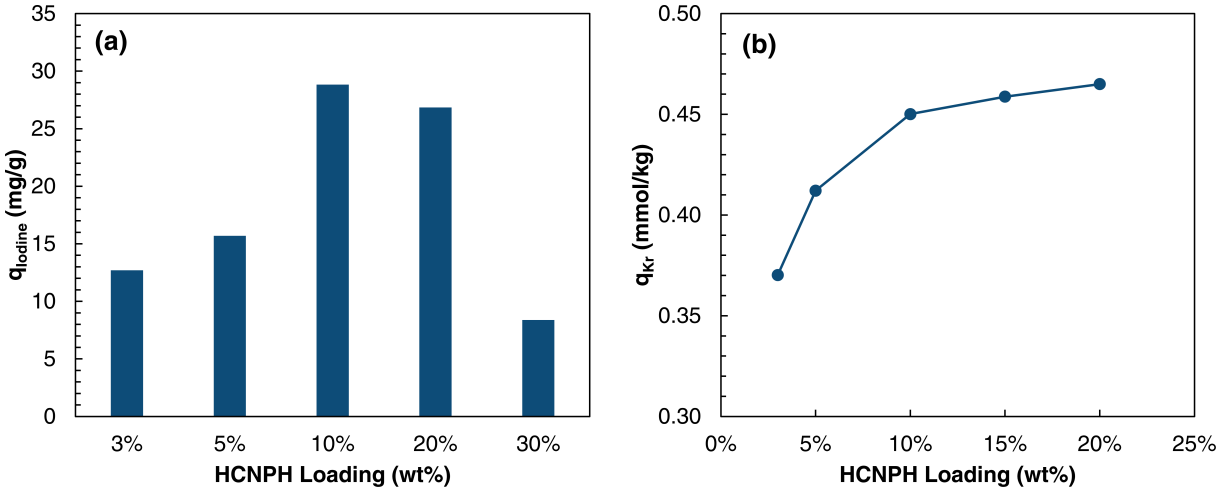

Figure 3.2: (a) Iodine and (b) krypton sorbent capacities for C/ETS-10 at various HCNPH (carbon) loadings

to increase substantially with the addition of carrbon on the ETS-10 up to 10 wt% HCNPHs on ETS-10. Subsequent additions of carbon only increase krypton uptake 1.6%, but lower the sorbent's iodine capacity. From this study, we deduce that at HCNPH loadings above 10 wt%, the carbon may block the larger pores of the ETS-10. This would make a portion of the sorbent's surface inaccessible to iodine molecules, but less so for krypton atoms, as they are smaller (Kr radius = 88 pm, I_2 radius = 532 pm). This conclusion is further supported by the 10 wt% C/ETS-10 having the highest available BET surface area, as shown in Table 2.1. Therefore, 10 wt% C/ETS-10 was determined to be the optimal loading of HCNPHs and was used for all subsequent adsorption experiments.

3.2.2 *Effect of Empty Bed Contact Time*

Many of the studies in the literature review were performed using static adsorption, a batch process. However, industrially, all adsorption is performed using continuous flow processes. Ther-

fore, it is important to perform dynamic adsorption in a continuous-flow column. In dynamic adsorption, gas flow through the sorbent bed is subject to channeling and maldistribution. This leads to gas that is not well-mixed within the adsorption bed, and the observed sorption capacity may be convoluted as a result. This can be avoided by having a large sorbent bed in which the bulk gas flow is given ample time to mix during its contact with the sorbent.

Increasing the bed height also increases the residence time of the off-gas in the bed, i.e., the empty bed contact time (EBCT). We performed iodine adsorption on 10 wt% C/ETS-10 at 20 °C for a range of EBCTs (0.8–7 s), by varying the sorbent bed height. We calculated the iodine sorption capacity for each experiment, and the results are shown in Fig. 3.3a. At an 0.8 s EBCT,

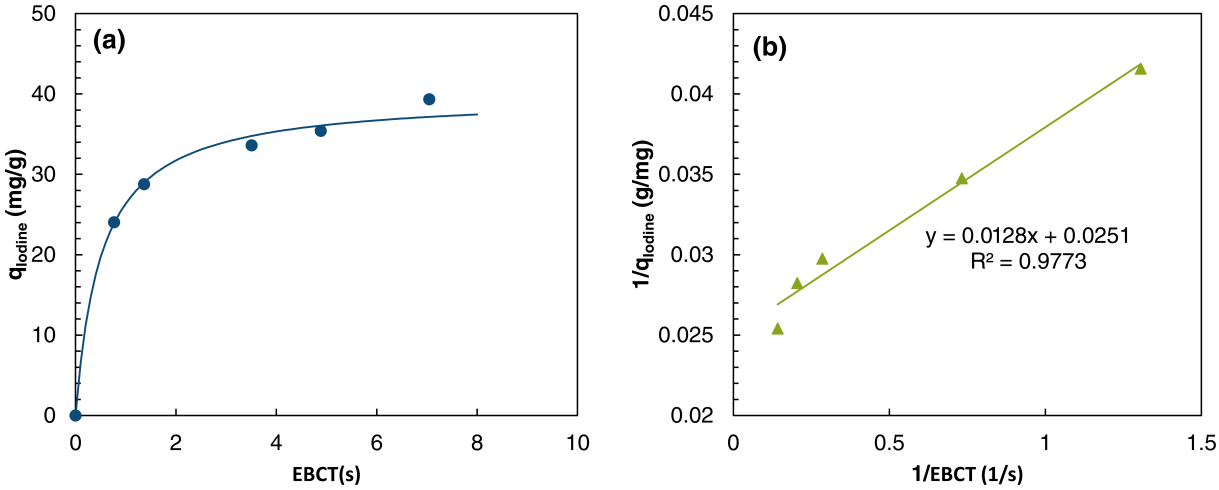

Figure 3.3: Iodine sorption capacities of 10 wt% C/ETS-10 at various empty bed contact times (EBCT) (a) q_{Iodine} vs. EBCT and (b) the linearized form

the sorbent was saturated quickly, yielding a 24.2 mg/g capacity. Increasing the EBCT to 1.4 s increased capacity to 28.9 mg/g, and increasing EBCT to 1.4 s increased the capacity to 28.9 mg/g. However, increasing EBCT further yielded a diminishing increase in iodine sorption capacity. The dependence of iodine sorption capacity on EBCT was found to follow a Langmuir-type relationship, where the sorption capacity approaches a maximum as the EBCT is increased according to Eq. 3.2,

$$q_{Iodine} = \frac{K_t q_m \tau}{K_t \tau + 1} \tag{3.2}$$

$$\frac{1}{q_{Iodine}} = \frac{1}{q_m} + \frac{1}{K_t q_m \tau} \tag{3.3}$$

where K_t is a constant related to EBCT, q_m is the maximum sorption capacity, and τ is the EBCT in seconds. Linearizing Eq. 3.2 gives Eq. 3.3. Then, $\frac{1}{q_{Iodine}}$ can be plotted against $\frac{1}{\tau}$ to find q_m from the intercept and K_t from the slope of the linear fit. The linearized data is shown in Fig. 3.3b. From Fig. 3.3b we found the maximum capacity to be 40.0 mg/g and K_t to be 1.95 s^{-1}.

3.2.3 Effect of Temperature

Adsorption, like all processes, can be described by the thermodynamic equation:

$$\Delta G = \Delta H - T\Delta S \tag{3.4}$$

Here, ΔG is the change in Gibbs free energy and ΔH and ΔS are the enthalpy and entropy changes, respectively. Since adsorption indisputably occurs, the process is spontaneous and $\Delta G < 0$. ΔS is also less than zero in virtually all adsorption because the adsorbate goes from the fluid phase to a solid phase. This requires that $\Delta H < 0$, making adsorption is an exothermic phenomenon. By applying Le Chatelier's principle, we conclude that adsorption will proceed to a higher extent at lower temperatures.

Le Chatlier's principle has been exploited in almost all the adsorption studies in the literature review, especially for krypton. Most researchers performed adsorption experiments with pure gas at cryogenic temperatures, which maximizes the adsorption capacity. Thus, the adsorption performance at low temperatures is idealistic and difficult to use in a practical manner. It is for this reason that we performed adsorption close to ambient temperature. We performed iodine sorption experiments from 10–60 °C and krypton sorption experiments from -10 to 20 °C to quantify the sensitivity of the sorbent capacity to the operating temperature. Each experiment was performed with one gram of 10 wt% C/ETS-10 in the adsorption column.

Fig. 3.4 shows the BT curves found for iodine sorption at various temperatures on 10 wt% C/ETS-10. Third-order polynomial fits are included as a solid line in Fig. 3.4 to illustrate trends of the experimental data. Fig. 3.5 shows the iodine and krypton sorption capacities of 10 wt% C/ETS-10. Fig. 3.4 shows the exhaustion time for iodine adsorption decreasing with increased operating temperatures from 14 hours at 10 °C, to 6 hours at 60 °C. The decreasing exhaustion time is because the increased temperature also increases the rate of adsorption while reducing the iodine sorption capacity; thus, the sorbent is more quickly saturated. In Fig. 3.5, iodine

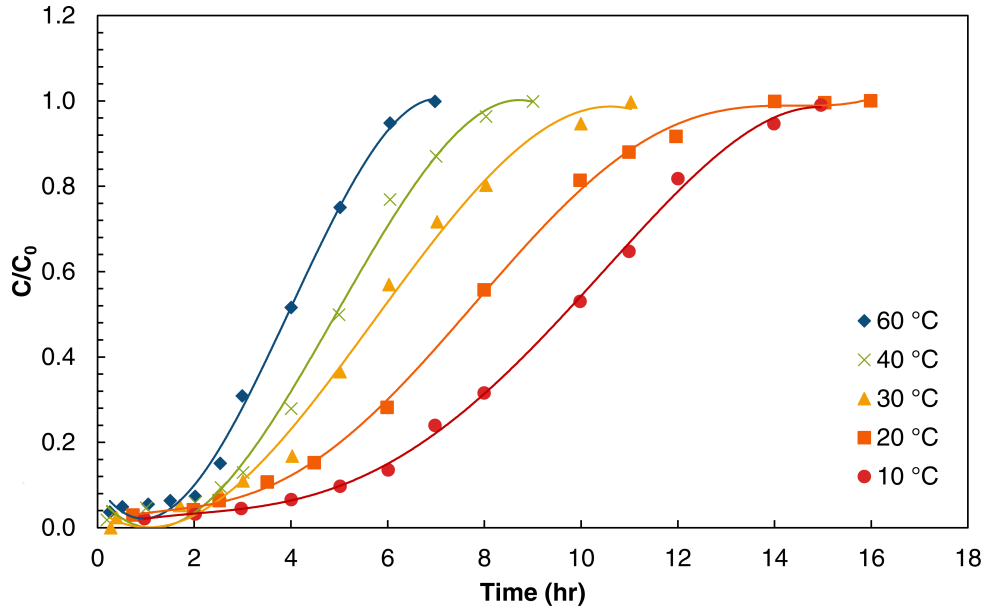

Figure 3.4: Breakthrough curves for iodine on 10 wt% C/ETS-10 from 10–60 °C

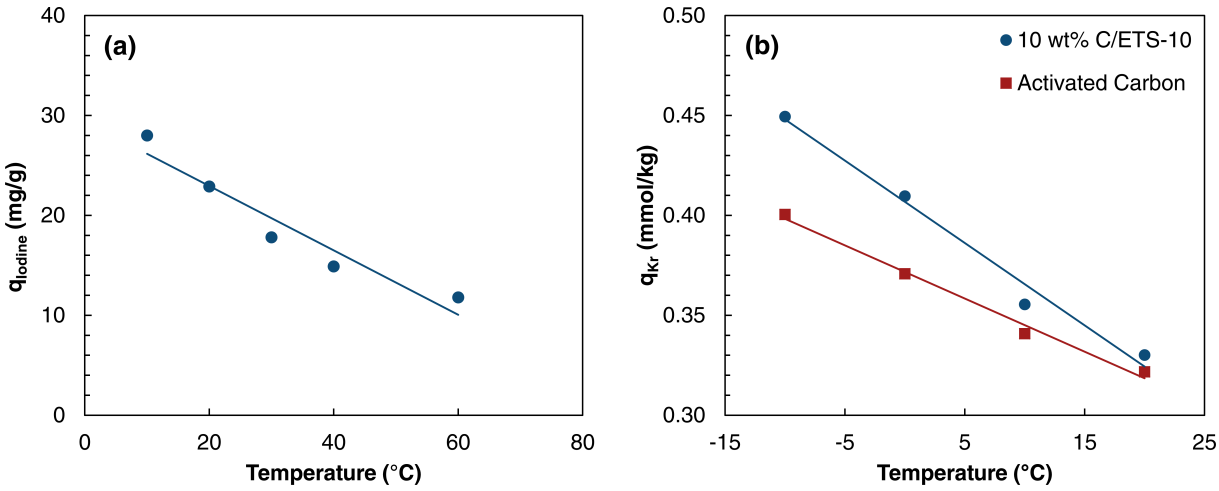

Figure 3.5: (a) Iodine and (b) krypton sorbent capacities for 10 wt% C/ETS-10 at various temperatures. Krypton capacity of activated carbon is shown as well in (b)

and krypton uptake are seen to decrease with increasing column temperature relatively linearly, confirming that this is an exothermic process.

3.2.4 Comparing 10 wt% C/ETS-10 to Other Sorbents

Coconut shell activated carbon 6–12 mesh was obtained from Fischer Scientific to compare its removal capacity for iodine and krypton to our C/ETS-10 sorbent. Fig. 3.6a shows the iodine BT curves for ETS-10, activated carbon, and 10 wt% C/ETS-10, and each experiment was done

at 20 °C with one gram of sorbent. The BT curves shown in Fig. 3.6b for krypton were collected at -10 °C with one gram of sorbent.

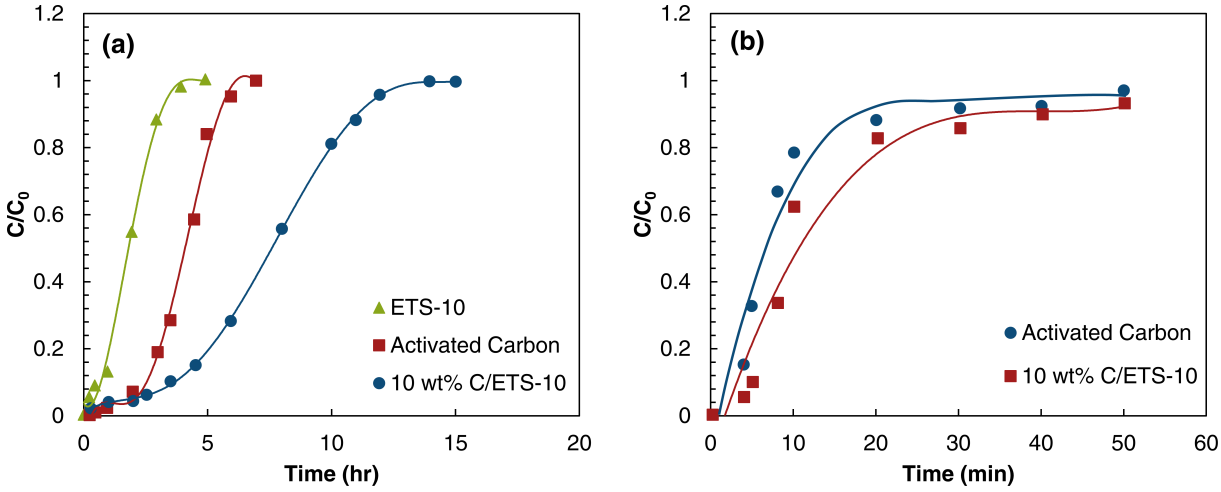

Figure 3.6: (a) Iodine (inlet = 25 ppm) and (b) krypton (inlet = 70 ppm) single component breakthrough curves at 20 °C

The observed iodine sorption capacities for ETS-10, activated carbon, and 10 wt% C/ETS-10 are 5.5, 11.5, and 28.9 mg/g, respectively, while the krypton capacities were 0.45 and 0.40 mmol/kg for 10 wt% C/ETS-10 and activated carbon, respectively. As stated in Chapter 1, AC is used a benchmark sorbent because of its historical use for iodine and krypton capture, and though it can not be used under the conditions of reprocessing, it is still regarded as an effective removal technique. As such, we chose to carry out comparison experiment with activated carbon, and results are promising for the C/ETS-10; 10 wt% C/ETS-10 exhibited 250% the iodine capacity of activated carbon at 20 °C and a 10% increase in krypton capacity. However, at temperatures higher than 20 °C the capacity of C/ETS-10 begins to diminish and approach that of AC. This is shown in Fig. 3.5b.

3.2.5 Characterization of Used Sorbent

We characterized the 10 wt% C/ETS-10 sorbent used for iodine sorption with TGA, EDS, SEM, TEM, and XRD. Since the amount of krypton adsorbed on the C/ETS-10 during krypton single component adsorption experiments was so small, our characterization gave no meaningful results.

TGA of the iodine-saturated 10 wt% C/ETS-10 was performed to measure the amount of adsorbate on various materials, and is shown in Fig. 3.7. During TGA, the sample of sorbent is

heated at a constant rate while its mass is measured and recorded. TGA was performed to 1000

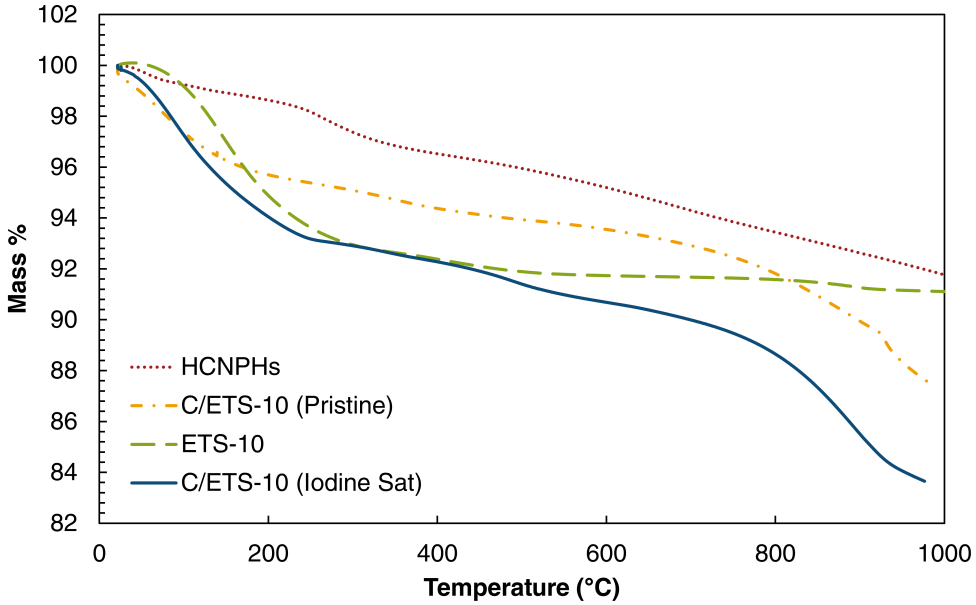

Figure 3.7: TGA of HCNPHs, ETS-10, and 10 wt% C/ETS-10 before and after iodine sorption

°C on the synthesized ETS-10, HCNPHs, and unused and iodine saturated 10 wt% C/ETS-10. ETS-10 exhibited an 8.3% mass loss, 7% of which was lost below 320 °C and is attributed to loosely bound water. Weight loss of the ETS-10 above 320 °C was slow and was comprised of water contained deep within the pores of ETS-10. The HCNPHs also lost water weight close to 4.8%. Both the unused and saturated C/ETS-10 samples had a similar mass loss, losing about 4.8 wt% from water. However, the iodine-saturated sample has two small steps at 250 and 450 °C, which may be due to iodine first being evaporated from the surface of the sorbent and then from deeper within the pores at higher temperatures.

EDS is a technique used for the elemental analysis of a sample. It uses X-rays to excite a sample which then releases X-rays. Each element has characteristic X-rays, thus the sample's composition can be analyzed with EDS. Fig. 3.8a and c show the EDS spectra of 10 wt% C/ETS-10 unused and iodine-saturated. EDS allowed us to confirm the presence of iodine on the 10 wt% C/ETS-10 at an amount close to the calculated iodine sorption capacity; five EDS spectra were taken of different iodine-saturated 10 wt% C/ETS-10 samples and reported a range of 3–7 wt% iodine on the samples. Two iodine peaks are seen on the EDS of the iodine-saturated sorbent in Fig. 3.8c. The EDS of the C/ETS-10 used for krypton adsorption is not shown, but is essentially identical to the EDS of the unused sorbent; krypton has no peak. This might be due to the fact

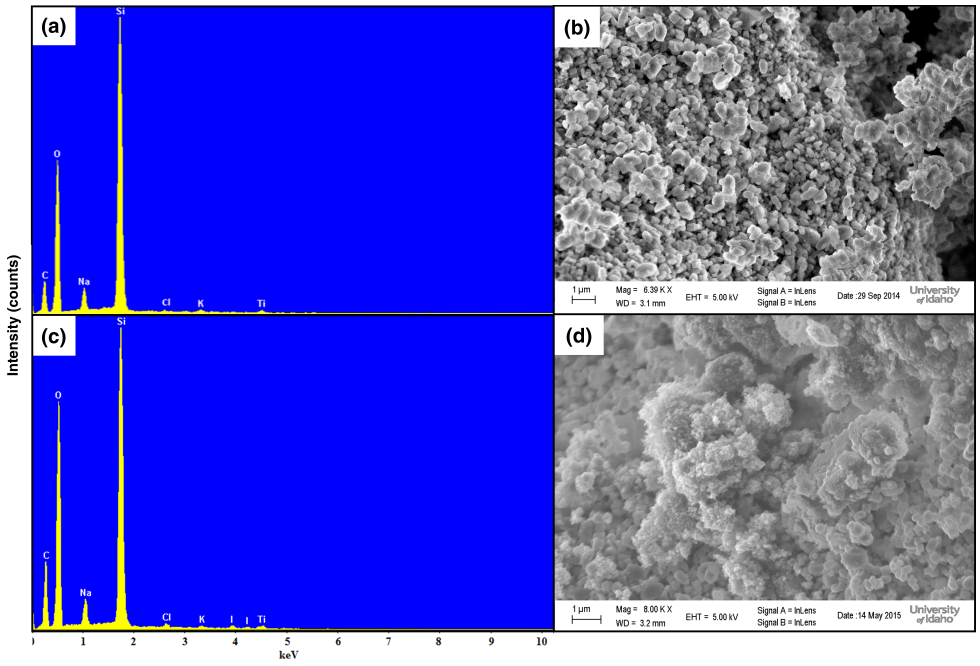

Figure 3.8: (a) EDS and (b) SEM of unused 10 wt% C/ETS-10, (c) EDS and (d) SEM of iodine saturated 10 wt% C/ETS-10

that EDS is carried out under a high vaccum and the small amounts of physisorbed krypton were driven off before the sample could be analyzed.

In Fig. 3.8d, the SEM of the used sorbent, shows small coral-like globules when compared to the larger crystals surrounding them. Theses coral-like globules are taken to be adsorbed iodine, as this is the only identifiable difference between the SEM of the unused (Fig. 3.8b) and saturated sorbent.

The XRD pattern of the iodine-saturated sorbent is shown in Fig.3.9. It contains all the original XRD peaks of the unused sorbent, though it has more noise due to amorphous iodine and possible shielding. However, there is one additional peak at $2\theta = 26.8^\circ$ on the used sorbent XRD. Peaks within 0.4° of this have been attributed to iodine adsorbed on graphite by Fleischmann [86] and iodine-doped ciprofloxacin by Refat [87]. This provides reasonable evidence that iodine has in fact crystallized to some degree on the surface of the C/ETS-10.

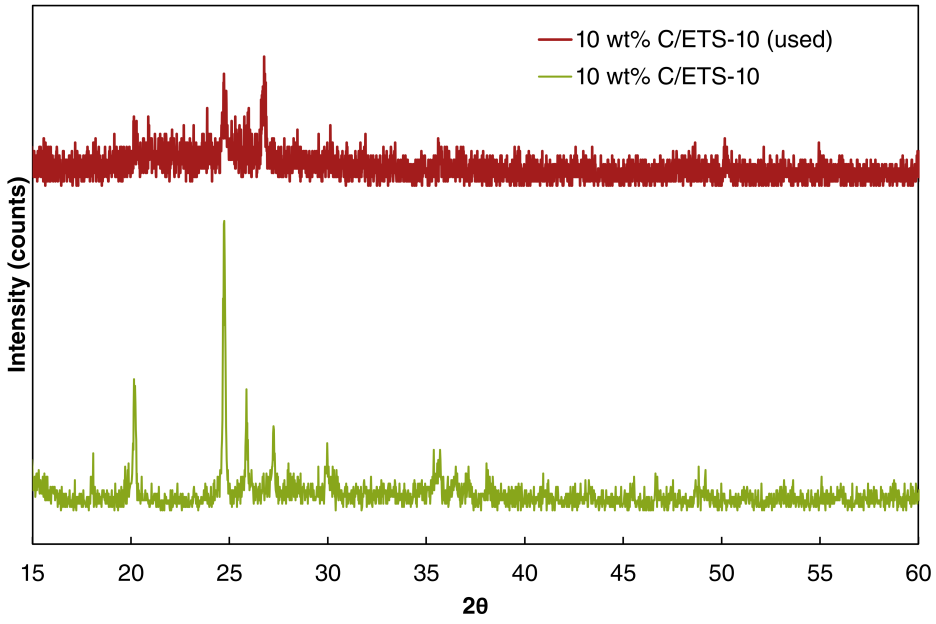

Figure 3.9: XRD pattern comparison of unused and iodine-saturated 10 wt% C/ETS-10

Chapter 4: Multicomponent Adsorption Studies

Pictured in Fig. 4.1 is the off-gas treatment schematic from ORNL [6]. Tritiated water is first removed on a 3A MS bed, followed by a bed of AgZ to remove iodine. Subsequently, an NaOH scrubber removes ^{14}C before the stream is dried to a dew point of -90 °C. Finally, Xe and Kr are captured separately on beds of AgZ and HZ, respectively. One of the goals of porous sorbent development is to avoid a complicated setup such as this by using adsorbents that are selective and effective even when multiple contaminants are present. To this end, we performed multi-contaminant adsorption experiments with iodine and krypton contained in nitrogen to understand how each contaminant affects the sorption of the other. We collected the sorption capacities of iodine and krypton while varying inlet concentration, temperature, and adding moisture. This research has value because to the best of our knowledge, no experiments evaluating the combined adsorption of iodine and krypton have been reported.

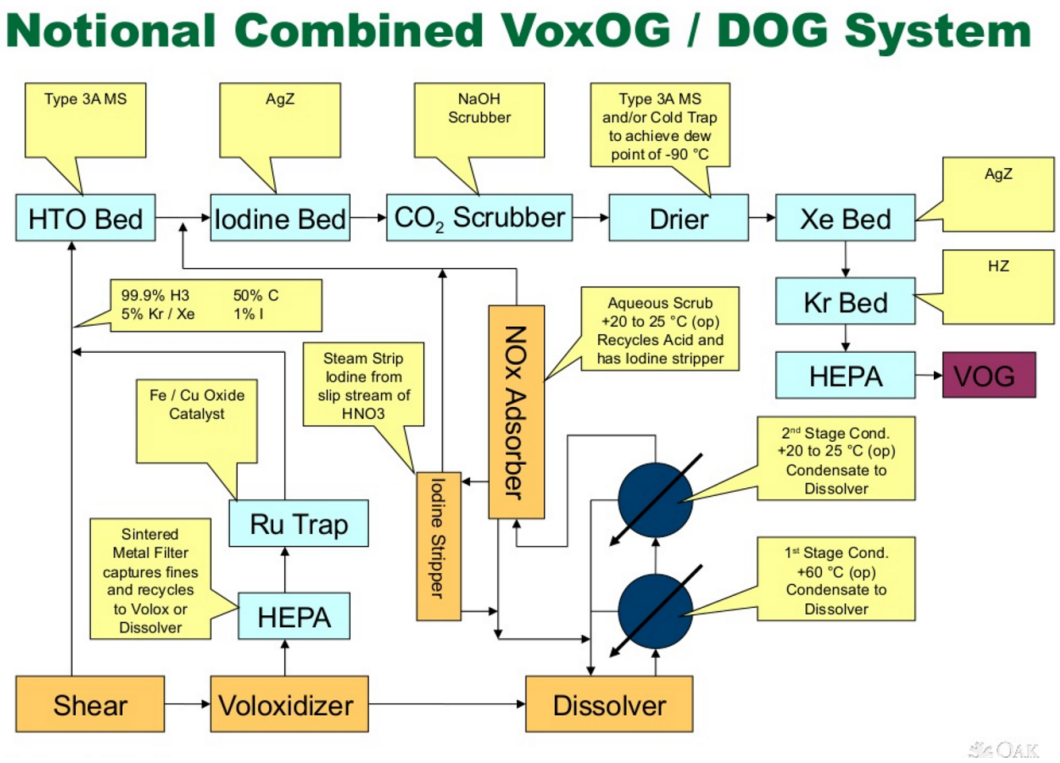

Figure 4.1: Flow diagram of off-gas treatment at Oak Ridge National Laboratories from [6]

4.1 Experimental Setup

The experimental setup and the methods used in the single component experiments were modified to add iodine, krypton, and moisture simultaneously to the off-gas. The multicomponent experimental setup is shown in Fig. 4.2. Iodine and krypton were added by flowing 1000 ppm

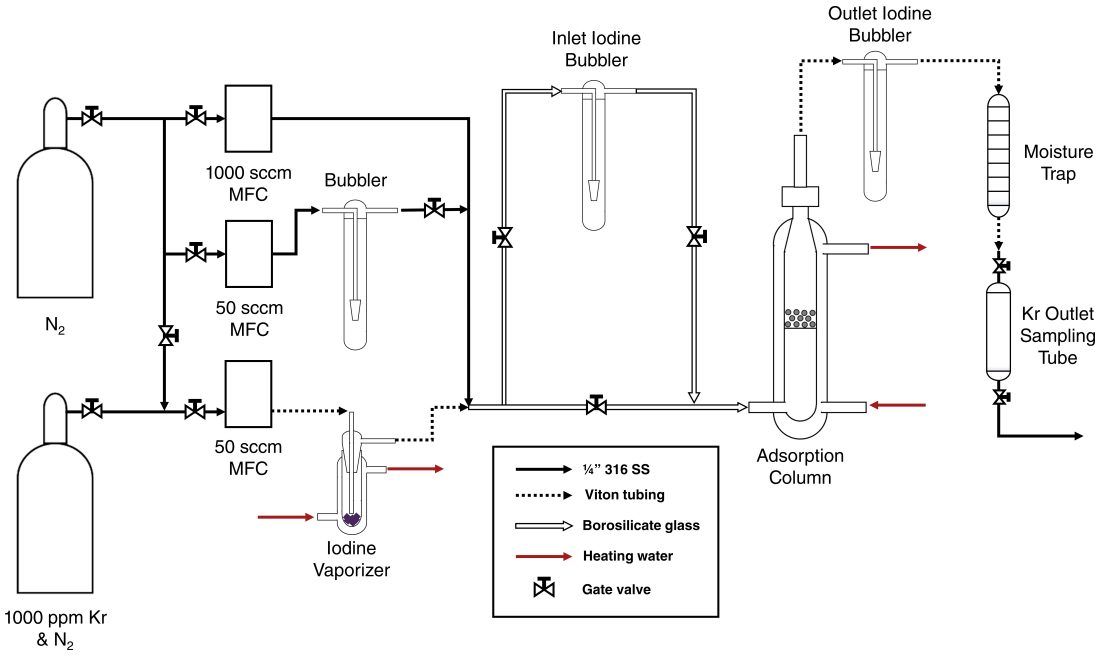

Figure 4.2: Experimental setup for multicomponent experiments including moisture addition

krypton balanced with N_2 through the iodine vaporizer. Bulk krypton concentration was varied by changing the flow rate of this stream between 10 and 30 SCCM. Bulk iodine concentration was varied by changing the temperature of the iodine vaporizer. As in the single component studies, the small stream of iodine and krypton was added to a large N_2 gas flow to make a simulated of gas containing 15–50$\pm$3 ppm iodine and 70–150$\pm$5 ppm krypton balanced with N_2 flowing at 180$\pm$1 SCCM. Moisture was added to the stream in relative humidities (RH) of 7–85% by splitting the large N_2 stream and flowing a portion of it through a water-filled bubbler, as shown in Fig. 4.2, and adding it to the main off-gas flow. The RH of the stream was measured using a DigiSense 60020-40 humidity meter.

The pelletization of the 10 wt% C/ETS-10 sorbent was modified by compacting the 1:1 10 wt% C/ETS-10 powder:colloidal silica paste in a stainless-steel pellet press rather than an extrusion press as was used in the single component studies. The modified pellet press is shown in Fig.

4.3. The modified pellet press produces a more uniform C/ETS-10 pellet of 1/8” diameter and

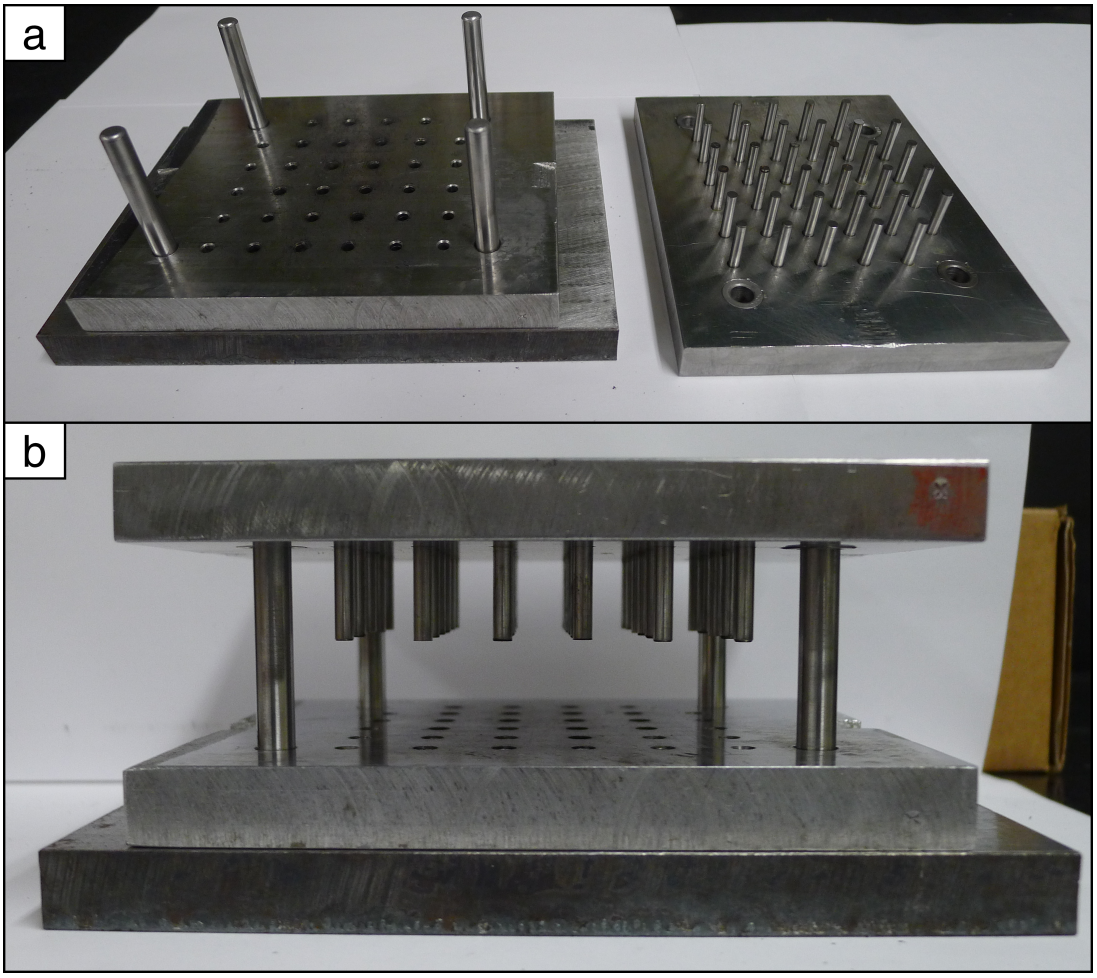

Figure 4.3: (a) Top view and (b) side view of the pellet press used to pelletize C/ETS-10

3/8” length. Both iodine and krypton single component adsorption experiments were redone with pellets made in the modified press at 20 °C with 2.5 g of sorbent as a standard. At an inlet concentration of 25 ppm iodine, the 10 wt% C/ETS-10 had a 46.5 mg/g sorption capacity, and krypton sorption capacity was 0.4 mmol/kg with an inlet of 70 ppm krypton.

4.2 Temperature Variation

Iodine and krypton capacities were studied on the 10 wt% C/ETS-10 sorbent at 20, 40, and 60 °C. The inlet stream contained 25 ppm iodine and 70 ppm krypton. BT curves are shown in Fig. 4.4. At 20 °C, adding krypton reduced iodine sorption capacity of 10 wt% C/ETS-10 from 46.5 mg/g for single component iodine to 41.5 mg/g, an 11% decrease. Adding 25 ppm iodine to 70 ppm krypton reduced single component krypton sorption capacity 3.5%, from 0.40 mmol/kg to

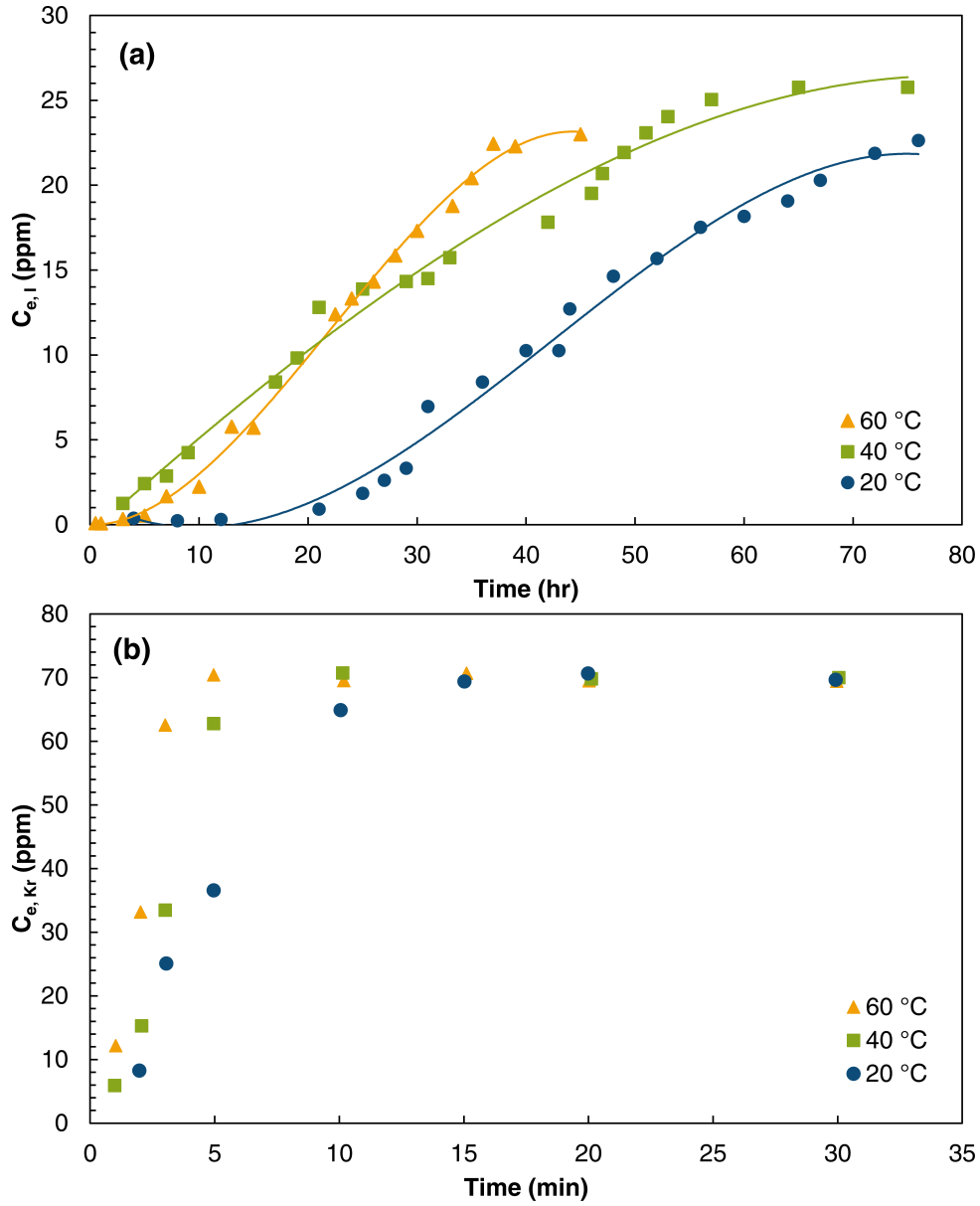

Figure 4.4: BT curves for (a) iodine and (b) krypton from 20–60 °C. Iodine inlet concentration was 25 ppm, and krypton inlet concentration was 70 ppm

0.38 mmol/kg. Increasing temperature to 60 °C decreased the sorption capacity for both contaminants; iodine capacity decreased 30% to 27.9 mg/g, and krypton capacity decreased 24%, to 0.29 mmol/kg.

4.3 Inlet Concentration Variation of Iodine and Krypton

Iodine sorption capacity was recorded while varying the iodine inlet concentration from 15–50 ppm, keeping krypton concentration at 70 ppm in the off-gas, and temperature at 20 °C. BT

curves for these experiments are shown in Fig. 4.5. Results of the inlet concentration variation experiments provide information on how the adsorption equilibrium changes with bulk concentrations and is used to derive isotherms discussed in the modeling chapter. Iodine sorption capacities were found to range from 33.5–49.5 mg/g, at iodine inlet concentrations of 15–50 ppm. Higher inlet concentrations yielded a higher iodine sorption capacities. The increase in iodine capacity accompanying the increased bulk iodine concentration in the off-gas is expected, as higher amounts of contaminant in the off-gas increase the mass transfer rate of contaminant from the bulk to the adsorbed phase, and shift the equilibrium concentrations to favor the adsorbed phase. The time for equilibrium to be reached decreases as the bulk concentration is increased. This phenomena can also be explained by the higher mass transfer driving force at higher bulk concentrations, which cause the sorbent to saturate faster.

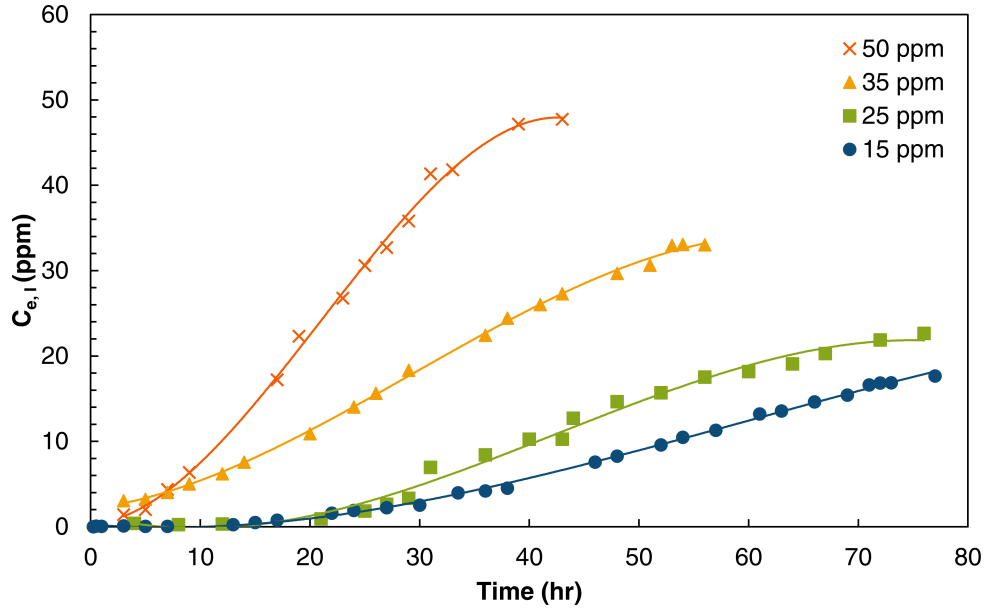

Figure 4.5: BT curves of iodine on 10 wt% C/ETS-10 with varying inlet iodine concentration. Bulk krypton concentration was held at 70 ppm and temperature was 20 °C.

Krypton inlet concentration was varied from 70–150 ppm while holding the bulk concentration of iodine at 25 ppm, and temperature at 20 °C. As with the iodine sorption experiments, higher inlet concentrations of krypton increased the krypton sorption capacity and decreased the time required to reach equilibrium. Krypton sorption capacity increased from 0.39 mmol/kg to 0.75 mmol/kg when the inlet krypton concentration was increased from 70 to 150 ppm.

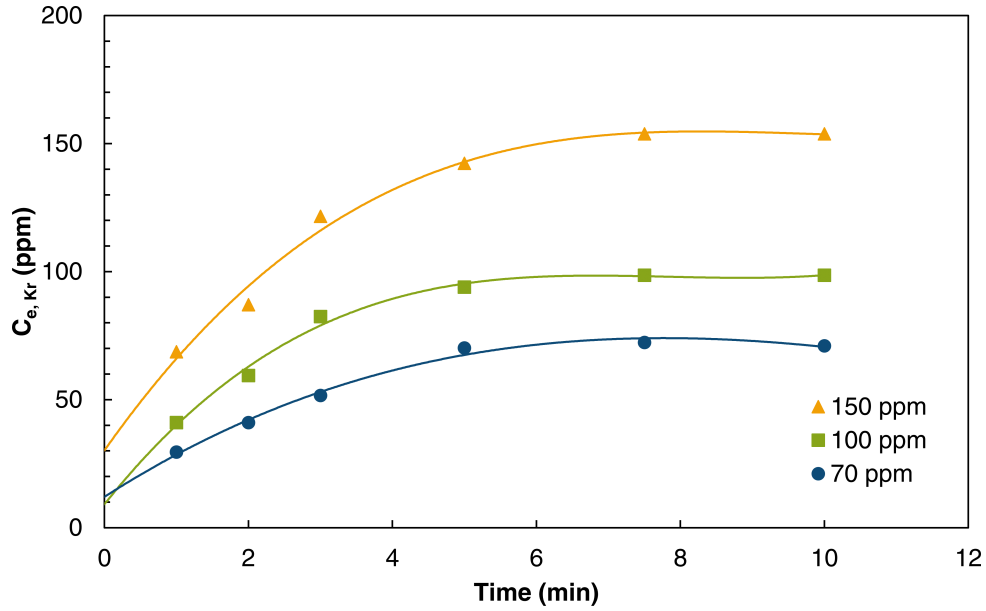

Figure 4.6: BT curves of krypton on 10 wt% C/ETS-10 with varying inlet krypton concentration. Bulk iodine concentration was held at 25 ppm and temperature was 20 °C.

Eq. 4.1 is the first order rate equation for adsorption processes:

$$\frac{dq_i}{dt} = k_i(q_e - q_i) \tag{4.1}$$

where q_i is the amount of component i in the adsorbed phase. Its rate of change is related to the rate constant, k_i, and the driving force for the reaction, $q_e - q_i$, where q_e is the equilibrium adsorbed amount. The rate constant typically follows the Arrhenius equation,

$$k_i = k_{i0}e^{\frac{-E_a}{RT}} \tag{4.2}$$

Where k_{i0} is a base rate constant, or frequency factor, E_a is the activation energy, T is the operating temperature of adsorption, and R is the universal gas constant.

Most physisorption has been shown to follow a first order process; therefore, it is not unreasonable to assume that the sorption of iodine and krypton on C/ETS-10 would as well. Equations 4.1 and 4.2 suggest that the rate of adsorption should be strongly dependent on temperature; however, calculating the rate constant for the inlet concentration variation experiments show that the rate of adsorption is also strongly dependent on the bulk concentration of contaminant.

This is because adsorption on C/ETS-10 is diffusion limited, meaning that the rate of adsorption is limited by the mass transfer of adsorbate from the bulk to the surface of the sorbent. Though Eq. 4.2 can still describe the process, it is actually a mass-transfer equation rather than a rate equation, and k_i describes mass transfer rate rather than adsorption rate. This affects how we mathematically describe adsorption and is discussed further in Chapter 5.

4.4 Iodine Adsorption with Moisture Addition

The effect of moisture on the adsorption capacity of iodine was studied by introducing moisture into the simulated off-gas stream at 30-85% relative humidity (RH) at 25 °C. Sorbent capacities for iodine in the moist stream were calculated from the generated breakthrough curves shown in Fig. 4.7. Each experiment was carried out with an off-gas stream of 25 ppm iodine, 70 ppm krypton, and was performed at 20 °C. Introducing moisture into the simulated off-gas stream

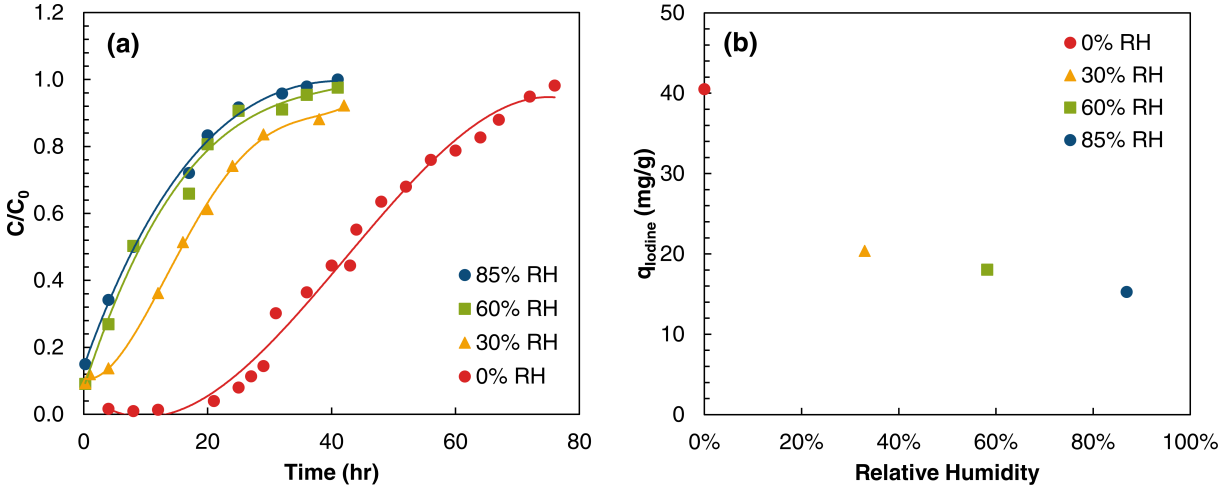

Figure 4.7: The effect of moisture addition on the iodine sorption of 10 wt% C/ETS-10. (a) BT curves and (b) iodine sorption capacity

even in small amounts had a significant effect of the 10 wt% C/ETS-10, reducing capacity 50% from 41.5 mg/g with no moisture added to 20.3 mg/g at 30% RH. However, higher RH further reduced the capacity only 12% more, with iodine sorption capacity decreasing to 15.3 mg/g at 85% RH. A hypothesis for this precipitous decrease in iodine sorption capacity with increasing RH is that at higher humidity moisture condenses, blocking a portion of the sorbent's pores, and thus, iodine's access to them. If true, this would mean that the moisture inhibition of iodine sorption is exclusive rather than competitive.

To add perspective by comparing the effect of moisture on other sorbents, Wu et al. found

that at 80 °C and 100% RH, the iodine capacity of Ag@ETS-10 was reduced 23% [76]. Staples et al. [14]found that just 5% RH decreased the iodine capacity of silver faujasite from 139 mg/g to 42 mg/g (a 70% decrease) at 100 °C and a 500 ppm iodine inlet concentration; and at conditions close to our study—60% RH and 25 °C—Moore and Howerton found the capacity of Amberlite XAD-12 to decrease 75% [32].

Chapter 5: Mathematical Modeling of Data

5.1 Adsorption Equilibrium

5.1.1 Adsorption Isotherms

Adsorption isotherms relate the concentration of contaminant in the bulk gas, C, to the adsorption capacity of the adsorbent at equilibrium, q_e. As the name 'isotherm' implies, these relations are at constant temperatures.

One of the simplest thermodynamic models for adsorption is the Langmuir isotherm, with the basic assumptions [23]:

1. Molecules of adsorbate are adsorbed on a fixed number of sites.
2. Each site may hold one adsorbate molecule.
3. All sites have equal affinity for the sorbate
4. There are no interactions between adsorbed molecules.

The Langmuir model can be derived from the rate equations [23]:

Rate of adsorption

$$r_{ads} = k_a C(1 - \frac{q_e}{q_m}) \tag{5.1}$$

Rate of desorption

$$r_{des} = k_d \left(\frac{q_e}{q_m}\right) \tag{5.2}$$

Where k_a and k_d are the kinetic rate constants of adsorption and desorption, respectively; C is the bulk concentration of contaminant; q_e is the amount of contaminant adsorbed in equilibrium with C, and q_m is the maximum capacity of the sorbent. At equilibrium, the rates of adsorption

and desorption are assumed to be equal. This allows to set Equations 5.1 and 5.2 equal to each other. Solving, we get Eq. 5.3.

$$q_e = \frac{q_m K_L C}{1 + K_L C} \tag{5.3}$$

In Eq. 5.3, K_L is the Langmuir equilibrium constant and is equal to k_a/k_d. This expression shows that adsorption under the Langmuir assumptions exhibits asymptotic behavior; as $C \rightarrow \infty$, $q_e \rightarrow q_m$. The linearized form of Eq. 5.3 is,

$$\frac{C}{q_e} = \frac{C}{q_m} + \frac{1}{K_L q_m} \tag{5.4}$$

By plotting C/q_e vs. C at constant temperature from experimental data, C being the inlet concentration of contaminant, q_m and K_L can be found from the reciprocals of the slope and intercept, respectively.

Though the Langmuir isotherm is based on theoretical principles, it makes many simplifying assumptions and has failed to predict all adsorption systems. The Langmuir's isotherms failures have led to an empirical isotherm, called the Freundlich isotherm.

$$q_e = K_F C^{1/n} \tag{5.5}$$

The Freundlich isotherm relation in Eq. 5.5, assumes that q_e is proportional to the bulk concentration of sorbate raised to a power, $1/n$, where n is greater than one for favorable isotherms, and less than one for non-favorable isotherms. K_F is the Freundlich equilibrium constant. The linearized form of the Freundlich isotherm is as follows;

$$ln(q_e) = ln(K_F) + \frac{1}{n} ln(C) \tag{5.6}$$

Plotting $ln(q_e)$ vs. $ln(C)$ gives K_F, and n from the intercept and slope of the graph, respectively. The linearized equations 5.4 and 5.6 were fit to multicomponent concentration variation equilibrium data for iodine and krypton to find the parameters shown in Table 5.1. Fig. 5.1 is a plot of

q_e vs. C_0, comparing iodine and krypton experimental sorption capacities to the Langmuir and Freundlich isotherms.

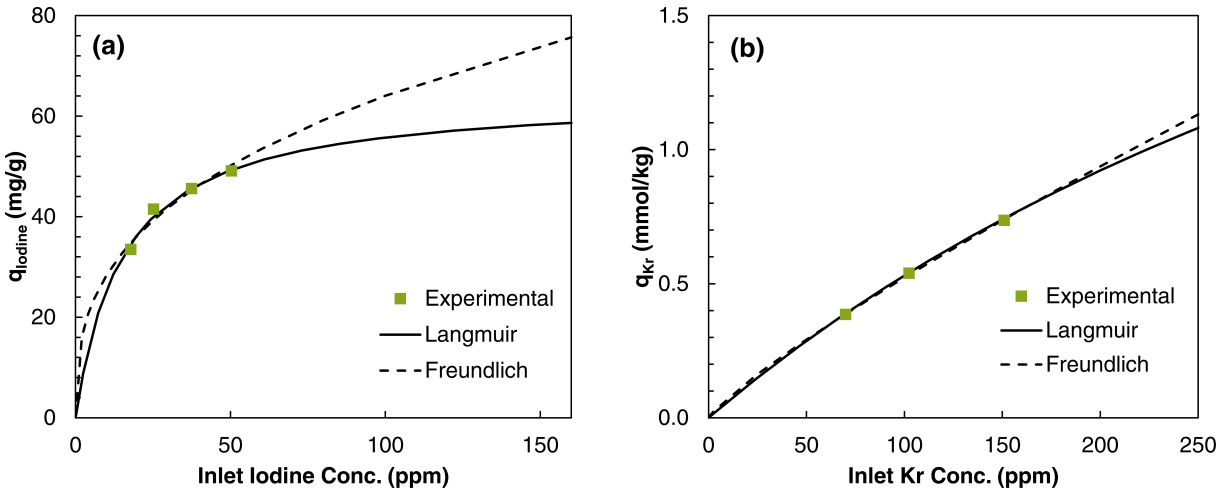

Figure 5.1: Langmuir and Freundlich isotherm fits for (a) iodine and (b) krypton multicomponent sorption capacities on 10 wt% C/ETS-10

Table 5.1: Langmuir and Freundlich isotherm parameters for iodine and krypton multicomponent concentration variation experiments

Model	Constants	Iodine	Krypton
Langmuir	q_m (mg/g)	64.26	0.2933
	K_L (L/mg)	6.3	0.52
	R^2	0.9945	0.9526
Freundlich	K_F (mg g^{-1} ppm^{-1})	12.57	0.0009
	n (mg_2 g^{L-1})	2.827	1.19
	R^2	0.9404	0.9992

The R^2 values and Fig. 5.1 show that both the Langmuir and Freundlich isotherms fit the data quite well within the experimental range. Originally, low concentrations of iodine and krypton over a small range were chosen to simulate actual nuclear reprocessing off-gas conditions; however, since the experimental data range is small, extrapolating to a wider range of concentrations using the Langmuir and Freundlich isotherms may lead to inaccurate sorption capacities. This poses problems when trying to use the isotherms as part of a more complex model to generate breakthrough curves. This issue is discussed in more detail in the mass-transfer modeling section.

5.1.2 The Equilibrium Constant

5.2 Kinetic Modeling of Adsorption in Fixed-Bed Columns

5.2.1 The Mass-Transfer Zone

Continuous processes offer increased productivity, reduced costs, and adaptability over batch processes. Adsorption is no different, and most industrial adsorption processes use a fixed bed of sorbent with a continuous flow of fluid. However, this situation is more complex than batch processing because the flow dynamics and transfer rate of the sorbate between fluid and sorbent determine efficiency rather than solely equilibrium, as in batch processes. In fixed-bed adsorption contaminant concentrations in the bulk and adsorbed phases change with position in the sorbent bed and time creating concentration profiles. Fig. 5.2 illustrates the concentration profile of the fluid phase in a fixed-bed column. The bottom half of the figure shows the effluent concentration of the column. The effluent concentration is related to the saturation level of the sorbent, which is pictured in the upper half of Fig. 5.2

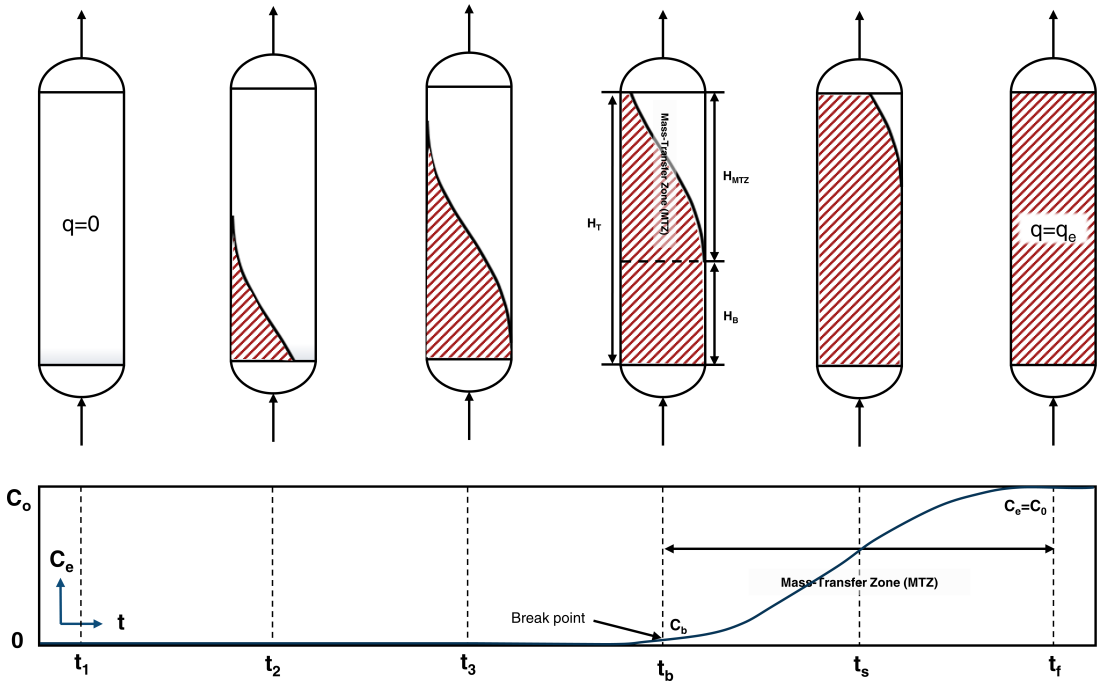

Figure 5.2: Illustration of the bulk fluid concentration profile in a fixed-bed adsorption column as a function of height in the sorbent bed and time

When adsorption begins at time t_1, the sorbent contains no contaminant. The rate of adsorption is highest when the fluid containing the contaminant contacts the bed. As the contaminant is adsorbed along the bed, its concentration in the bulk fluid drops until none is left in the bulk. This length of bed where adsorption occurs is known as the mass-transfer zone (MTZ), and it is depicted in Fig. 5.2 at time t_b. The length of the MTZ depends on the rate of adsorption, and is elongated by mass-transfer resistances which slow adsorption rate. The mass-transfer resistances and axial dispersion in the bed also create the 'S' shape of the MTZ. Once the section of the sorbent bed closest to the inlet is saturated, the MTZ shifts toward the end of the bed until time t_b, the break point, when the outlet concentration of the column is C_b, the maximum allowed concentration of contaminant in the outlet stream. After t_b, the outlet concentration continues to increase until the exhaustion time, t_f, when the sorbent is completely saturated.

5.2.2 Scale-Up Design Method for Adsorption Columns

Knowledge of the MTZ properties is critical because in industrial applications adsorption may only be carried out until the break point, since no effluent concentration greater than C_b is allowed. Column design requires that the height of the bed must be much larger than the MTZ to maximize effective use of the sorbent and avoid having to recharge the adsorption column frequently. Because of the C_b limit, adsorption can not be carried out to equilibrium, or saturation of the sorbent, and the sorbent capacity calculated through Eq. 5.7 (from Chapter 3) at equilibrium is not representative of the sorbent's usefulness; only a portion of this capacity may be utilized.

$$q_i = Q \int_0^{t_f} \frac{(C_{i0} - C_{ie})}{M} dt \tag{5.7}$$

If Eq. 5.7 determines the total sorbent capacity, then Eq. 5.8 refers to the usable sorbent capacity.

$$q_{iu} = Q \int_0^{t_b} \frac{(C_{i0} - C_{ie})}{M} dt \tag{5.8}$$

q_{iu}, or the usable sorbent capacity, is the loading of contaminant on the sorbent at the time at which the effluent concentration of the column is at the maximum permissible level, C_b. The

ratio q_{iu}/q_i is then the fraction of the total bed capacity completely saturated at t_b. If the sorbent bed is assumed to have uniform density and adsorptive properties, then the ratio q_{iu}/q_i is also proportional to the length of the bed saturated, H_B, at t_b. H_B is found by Eq. 5.9 and illustrated in Fig. 5.2.

$$H_B = \frac{q_{iu}}{q_i} H_T \tag{5.9}$$

In Eq. 5.9, H_T is the total height of the sorbent bed. The length of the MTZ, H_{MTZ}, can then be found by the difference of the total height of the bed and the length of bed saturated, as shown in Eq. 5.10.

$$H_{MTZ} = H_T - H_B \tag{5.10}$$

Once the height of the MTZ is known, it can be used in conjunction with removal requirements to design an adsorption column. The caveat of extending this method to other operating conditions is that the height of the MTZ changes with temperature, inlet concentration, and other parameters—the question is, how? Performing experiments such as the ones in Chapters 3 and 4 answers this question to an extent, but performing experiments to cover all operating conditions is impractical. Therefore, experimental data is fit to kinetic models, which are used to predict the behavior of adsorption.

5.2.3 The Thomas, Yoon-Nelson, and Adams-Bohart Models

The model proposed in 1944 by Thomas [88] is one of the most widely used models to predict fixed-bed column breakthrough. The Thomas Model assumes that the Langmuir isotherm applies and that axial dispersion of the sorbate in the column is negligible. It follows Eq. 5.11 [89–91];

$$ln\left(\frac{C_0}{C_e} - 1\right) = \frac{q_0 k_{TH} M}{Q} - k_{TH} C_0 t \tag{5.11}$$

where C_0 and C_e are the inlet and outlet concentrations of the column, respectively; q_0 is the maximum adsorption capacity of the sorbent in equilibrium with C_0; k_{TH} is the Thomas kinetic constant; M is the mass of sorbent charged to the column; Q is the volumetric flow rate of fluid through the column, and t is the time of experiment. A plot of $ln\left(\frac{C_0}{C_e}-1\right)$ vs. t gives a linear trend from which q_0 and k_{TH} can be found.

The Yoon-Nelson Model is a less complicated model that does require any adsorbent characteristics, such as sorbent capacity [92]. The model assumes that the probabilities of breakthrough and the rate of decrease in adsorption are proportional. The Yoon-Nelson Model is described by Eq. 5.12.

$$ln\left(\frac{C_e}{C_0-C_e}\right)=k_{YN}t-\tau k_{YN} \tag{5.12}$$

In Eq. 5.12, k_{YN} is the Yoon-Nelson kinetic constant, and τ is the time required for 50% breakthrough of the adsorbate. k_{YN} and τ can be found from the slope and intercept of $ln\left(\frac{C_e}{C_0-C_e}\right)$ vs. t, respectively.

. Originally proposed by Adams and Bohart [93], the model was meant to account for the adsorption of chlorine on a fixed bed of activated carbon. It is based on the definition chemical activity in a diluted medium, and it is simplified to Eq. 5.13 by assuming [94, 95]:

- Low bulk concentrations of contaminant. $C << C_0$.
- When $t \rightarrow \infty$, $q \rightarrow N_0$. Where N_0 is the adsorption capacity of the adsorbent per unit volume of the bed.
- The rate of adsorption is limited by external mass transfer.

This leads to Eq.5.13

$$ln\left(\frac{C_e}{C_0}\right)=C_0k_{AB}t-N_0k_{AB}(H_T/v) \tag{5.13}$$

Like the Thomas and Yoon-Nelson Models, the Adams-Bohart Model includes a kinetic constant, k_{AB}. H_T is the height of the bed, and v is the superficial velocity of fluid through the column. N_0 and k_{AB} can be found from a linear plot of $ln\left(\frac{C_e}{C_0}\right)$ vs t.

Comaparison of Model Parameters

The Thomas, Yoon-Nelson, and Adams-Bohart model parameters from equations 5.11–5.13 were found for single component iodine experiments, shown in Table 5.2, and multicomponent experiments, shown in Tables 5.3 and 5.4. Figures 5.3 and 5.4 compare the experimental and model-generated BT curves. All model BT curves were generated by solving Equations 5.11–5.13 for C_e/C_0 using model parameters from the tables.

Table 5.2: Thomas, Yoon-Nelson, and Adams-Bohart Model parameters for iodine breakthrough in single component temperature variation experiments.

Model	Component	Iodine			
	Temp. (°C)	10	20	40	60
Thomas	q_0 (mg/g)	24.69	19.37	12.62	9.56
	k_{TH} (L/gh)	2123	2536	4123	5049
	R^2	0.9640	0.9312	0.9409	0.9130
	SSE	0.0404	0.0302	0.0373	0.0674
Yoon-Nelson	τ (hr)	8.817	6.917	4.507	3.415
	k_{YN} (1/hr)	0.5506	0.6577	1.0690	1.3092
	R^2	0.9640	0.9312	0.9409	0.9130
	SSE	0.0404	0.0302	0.0373	0.0674
Adams-Bohart	N_0 (g/L)	9.111	8.139	5.251	4.189
	k_{AB} (L/gh)	1120	1101	1804	2131
	R^2	0.9574	0.9287	0.9242	0.9353
	SSE	0.6282	0.9370	1.0896	0.5517

The R^2 values shown in the tables are measures of how well the experimental data fits the linearized forms of the model equations. The sum of the squared errors, SSE, indicates how well the experimental BT curves match the BT curves generated by each model. SSE values were calculated with Eq. 5.14;

$$SSE = \sum_{i=1}^{N} \left(C_{e,exp} - C_{e,model}\right)^2 \tag{5.14}$$

where N is the number of data points, and $C_{e,exp}$ and $C_{e,model}$ are the effluent adsorbate concentrations of the column from the experiment and calculated by the corresponding model, respectively. According to Eq. 5.14, SSE values are dependent on how many experimental data points exist, but each experiment has varying amounts of data points. Each experiment having a different number of experimentally gathered points means that model fits across different experiments

cannot be compared using the SSE.

Examining Equations 5.11 and 5.12 more closely, we see that the Thomas and Yoon-Nelson models are mathematically equivalent; this is made apparent by the identical R^2 and SSE values for both models. The difference between the two models is in their utility. The Yoon-Nelson Model is more concise in form, as it excludes parameters that describe the sorbent bed in its calculation; thus, when extrapolating the model over wide ranges of operating conditions the Yoon-Nelson model has less utility than the Thomas model which includes flow rate and bed height in its calculation.

In general, the Thomas and Yoon-Nelson models fit significantly better than the Adams-Bohart model. The superior fit is exemplified by the SSE values for the Thomas and Yoon-Nelson models being lower than the Adams-Bohart model in Tables 5.2–5.4. Furthermore, the Adams-Bohart BT curve fits in Figures 5.3 and 5.4 increase exponentially without being limited to $C_e/C_0 = 1$, and this trend is not realistic.

Table 5.3: Thomas, Yoon-Nelson, and Adams-Bohart Model parameters for iodine and krypton breakthrough in multicomponent concentration variation experiments.

Model	Component	Iodine				Krypton		
	Concentration (ppm)	15	25	35	50	70	100	150
Thomas	q_0 (mg/g)	37.85	38.72	45.20	50.38	0.0286	0.0331	0.0621
	k_{TH} (L/gh)	656.7	325.5	254.7	311.2	300093	145439	110946
	R^2	0.9571	0.9306	0.9931	0.9868	0.9415	0.9958	0.9674
	SSE	0.0734	0.0385	0.0034	0.0134	0.0238	0.0025	0.0115
Yoon-Nelson	τ (hr)	47.79	34.30	28.75	22.50	0.0273	0.0226	0.0274
	k_{YN} (1/hr)	0.1207	0.0850	0.0930	0.1618	72.96	49.31	58.51
	R^2	0.9571	0.9306	0.9931	0.9868	0.9415	0.9958	0.9674
	SSE	0.0734	0.0385	0.0034	0.0134	0.0238	0.0025	0.0115
Adams-Bohart	N_0 (g/L)	12.64	15.84	18.77	19.22	0.0208	0.0404	0.0643
	k_{AB} (L/gh)	426.5	166.0	132.1	168.9	51905	19817	12475
	R^2	0.8757	0.9389	0.9402	0.8522	0.9653	0.7147	0.7956
	SSE	5.3118	0.0650	0.2447	1.6472	0.0061	0.0581	0.0376

The q_0, τ, and N_0 parameters of the three models describe the bulk properties of the sorbent. These parameters define the general height and length of the BT curve. Figures 5.3–5.4 show that each kinetic model generally fits the overall height and length of the experimental BT curves well. As such, the sorption capacity parameters, q_0 and N_0, are close to the sorption capacities calculated for each experiment. In single component experiments, the sorbent capacity calculated from the experiment ranged from 11.8 mg/g at 60 °C to 28.0 mg/g at 10 °C; the q_0

Table 5.4: Thomas, Yoon-Nelson, and Adams-Bohart Model parameters for iodine and krypton breakthrough in multicomponent temperature variation experiments.

Model	Component	Iodine			Krypton		
	Temp. (°C)	20	40	60	20	40	60
Thomas	q_0 (mg/g)	38.72	31.08	29.38	0.0869	0.0588	0.0347
	k_{TH} (L/gh)	325.5	411.3	682.6	122666	212487	406708
	R^2	0.9306	0.8852	0.9312	0.9844	0.9819	0.9939
	SSE	0.0385	0.1089	0.0784	0.0124	0.0114	0.0050
Yoon-Nelson	τ (hr)	34.31	26.86	25.98	0.0842	0.0560	0.0330
	k_{YN} (1/hr)	0.0850	0.1101	0.1788	29.41	51.66	98.89
	R^2	0.9306	0.8852	0.9312	0.9844	0.9819	0.9939
	SSE	0.0385	0.1089	0.0784	0.0124	0.0114	0.0050
Adams-Bohart	N_0 (g/L)	15.84	14.85	9.77	0.0545	0.0364	0.0187
	k_{AB} (L/gh)	166.0	154.7	470.9	33443	57733	103952
	R^2	0.9389	0.8012	0.8036	0.7047	0.6620	0.7725
	SSE	0.0650	0.7931	7.3840	0.2280	0.4864	0.2298

parameter from the Thomas model for the single component iodine experiments is about 15% smaller, ranging from 9.56 to 24.7 mg/g in the same temperature range. The reason for the discrepancy between q_0 and the actual sorption capacity is because the Thomas model predicts a slightly faster breakthrough, as shown in Fig. 5.3, and this correlates to a smaller sorption capacity. Another discrepancy of the Thomas and Yoon-Nelson models is seen at the top and bottom of the 'S' curve shape. This is especially true of the multicomponent iodine breakthrough fits shown in Fig. 5.4a and c. One possible explanation that the Thomas and Yoon-Nelson models do not conform to the exact shape of the experimental data breakthrough is that the inlet concentration of iodine during experiments tended to drift $\pm$3 ppm. Both models are based on a constant inlet concentration assumption and were found to be quite sensitive to changes; model parameters varied up to 25% when calculated with a 3 ppm change in the inlet concentration. Another reason that the Thomas and Yoon-Nelson models may not conform to the shapes of the multicomponent curves specifically, is the existence of a competition between iodine and krypton for adsorption sites. This competition can change the shape of the BT curves in ways unaccounted for by the Thomas and Yoon-Nelson models. However, the general fit still represents the experimental capacity and the length of the MTZ in general, as the inlet concentration was taken frequently during experiments and an average value for the inlet concentration was used for all calculations.

Overall, the purpose of modeling experimental BT data is to predict breakthrough behavior at

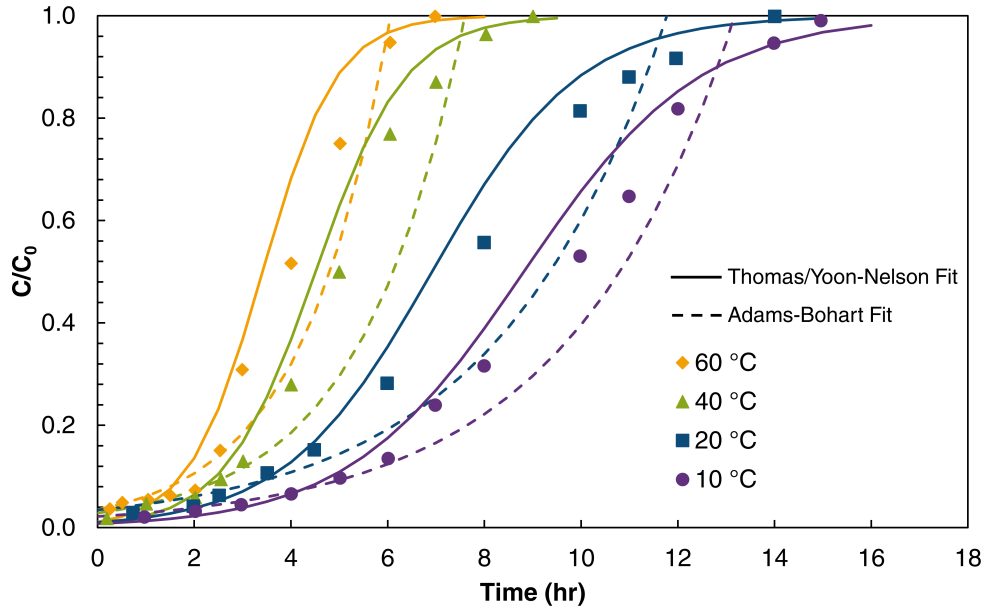

Figure 5.3: Thomas, Yoon-Nelson, and Adams-Bohart model fits for single component iodine breakthrough experiments with column temperature variation

inlet concentrations and temperatures not experimentally tested. To do this accurately, the model parameters must follow a predictable trend. The trends of the model parameters are illustrated in Fig. 5.5, which shows the model parameters for iodine breakthrough experiments as functions of temperature for single component experiments, and inlet concentration for multicomponent experiments.

Parameter fits for single component iodine experiments in Fig. 5.5a–c show a definite trend in the model parameters. The kinetic constants for each model increase with temperature close to linearly, though the deviations appear unpredictable. Multicomponent iodine parameter fits are much more erratic. Trends exist, but it is less clear whether it is due to the system's conditions or outlying data.

In general, the Thomas and Yoon-Nelson Models fit the experimental data, but their respective "kinetic constants" largely lack a physical meaning. We can examine the parameters' trend with temperature or concentration; however, no thermodynamic consideration is included in their calculation and the kinetic constants of these models lumped many phenomena into a single constant. Including thermodynamics in the BT curve prediction allows an iterative solution that is much more adaptable and discloses fundamental information about the adsorption process, such as the heat of adsorption, spontaneity of the process, and adsorption behavior (isotherms). If the process is more thoroughly understood, then a more adaptable model can be derived.

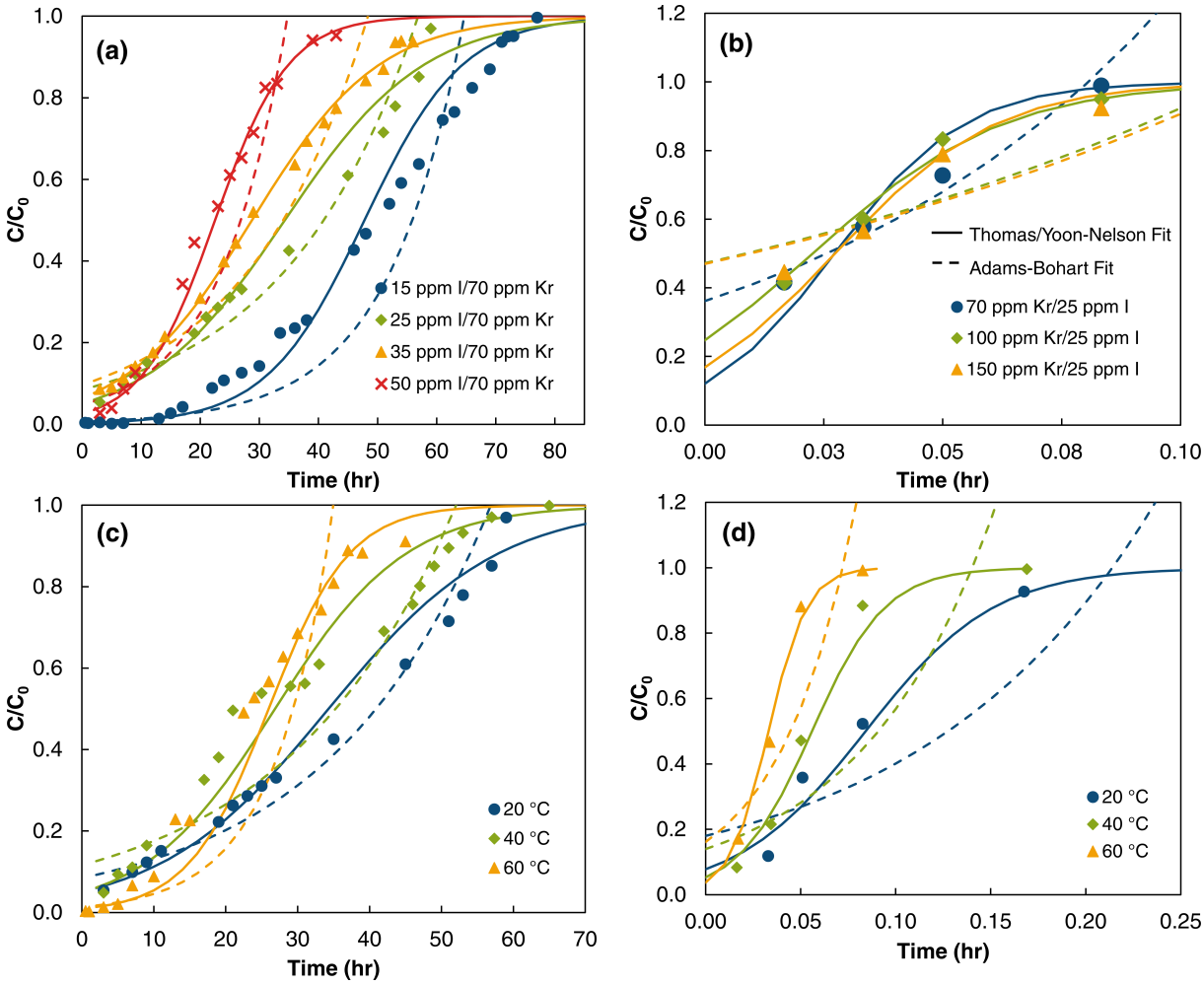

Figure 5.4: Thomas, Yoon-Nelson, and Adams-Bohart model fits for multicomponent experiments. (a) iodine breakthrough with inlet iodine concentration variation, (b) krypton breakthrough with krypton inlet concentration variation, (c) iodine breakthrough with column temperature variation, and (d) krypton breakthrough with column temperature variation. Thomas/Yoon-Nelson fits are shown by a solid line, and Adams-Bohart by a dashed line. Model line colors correspond the breakthrough colors shown in the legend on each graph.

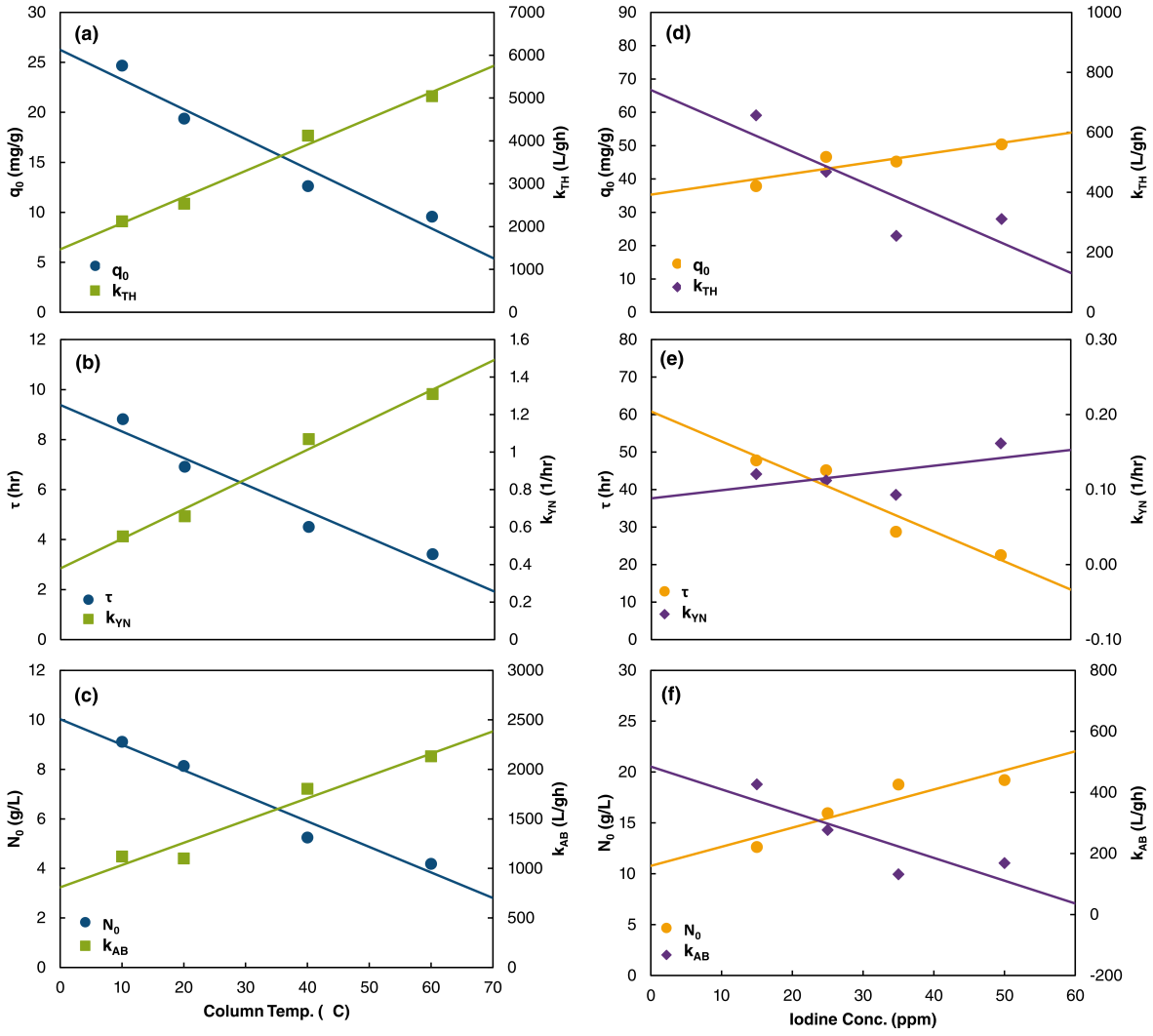

Figure 5.5: Thomas, Yoon-Nelson, and Adams-Bohart parameters as functions of (a-c) temperature for single component iodine experiments, and (d-f) inlet iodine concentrations for multicomponent experiments

5.3 Mass-Transport Based Model

5.3.1 Equation Derivation

A more rigorous model can be derived from mass balance of the sorbate around a differential element of the adsorption column with the general relation,

Rate of change of concentration in the gas phase = Flow of sorbate in - Flow of sorbate out - Rate of adsorption

This relation allows a differential equation to be derived provided the following assumptions,

1. The adsorption column has no radial concentration gradient.
2. Bulk gas follows the ideal gas law.
3. Properties of the sorbent including affinity for the contaminant and bed density are uniform.
4. The inflow of gas has a constant velocity, which it maintains in the column.

To find Eq. 5.15.

$$\frac{\partial C(t,z)}{\partial t} = D_z \frac{\partial^2 C(t,z)}{\partial z^2} - v\frac{\partial C(t,z)}{\partial z} - \rho_b \frac{\partial q(t)}{\partial t} \tag{5.15}$$

Where,

- $t =$ Time of experiment
- $z =$ Position in the column. z is contained in the range $[0, L]$
- $C(t,z) =$ Concentration of the gas contaminant or sorbate as a function of time and bed depth
- $D_z =$ Diffusivity of the contaminant through the bulk gas
- $v =$ Superficial velocity of the bulk gas through the column
- $\rho_b =$ Density of the sorbent bed, (mass/volume)

- $q(t) =$ Adsorbed amount of the contaminant. Varies with time

Eq. 5.15 relates the spatial and temporal change in the bulk concentration of contaminant, $C(t,z)$, to convective mass transfer, $\left(v\frac{\partial C(t,z)}{\partial z}\right)$, axial dispersion, $\left(D_z\frac{\partial^2 C(t,z)}{\partial z^2}\right)$, and adsorption rate, $\left(\rho_b\frac{\partial q}{\partial t}\right)$. Typically, the axial dispersion in gas flow columns at low flow is negligible, which reduces Eq. 5.15 to,

$$\frac{\partial C(t,z)}{\partial t} = -v\frac{\partial C(t,z)}{\partial z} - \rho_b\frac{\partial q}{\partial t} \tag{5.16}$$

In Eq. 5.16, the adsorption rate term is the most significant, and is where the thermodynamics and kinetics of adsorption can be included.

Pseudo-First and Second Order Kinetic Models

There are several kinetic models proposed to describe the rate of adsorption on different adsorbents. The pseudo-first and pseudo-second order models for gas-solid adsorption are the most widely used because they are simple and fit many systems well [96]. Lagergren [97] proposed the pseudo-first order model with the assumption that adsorption rate is proportional to the number of vacant adsorption sites, and is expressed as,

$$\frac{\partial q}{\partial t} = k_i(q_e - q) \tag{5.17}$$

Where, k_i is the pseudo-first order adsorption rate constant, and q_e is the equilibrium adsorption amount relative to the bulk concentration. At $t = 0$, $q = 0$, and as $t \to \infty$, $q \to q_e$. Solving Eq. 5.17 using these boundary conditions yields,

$$q = q_e\left(1 - e^{-k_i t}\right) \tag{5.18}$$

Pseudo-second order kinetics are similar, but assume that the rate of adsorption is proportional to the square of the number of vacant sites, as shown by Eq. 5.19.

$$\frac{\partial q}{\partial t} = k_s(q_e - q)^2 \tag{5.19}$$

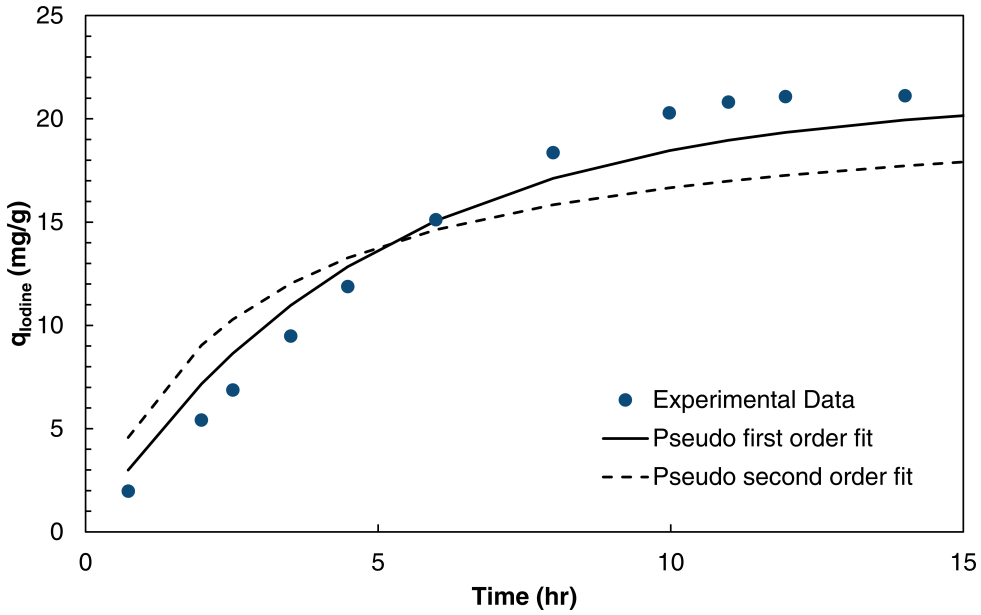

Figure 5.6: Comparsion of pseudo-first and -second order kinetic models with experimental data. Experimental data is from a single component iodine experiment. inlet concentration of iodine was 25 ppm, temperature was 20 °C.

Eq. 5.19 is the pseudo-second order kinetic model where k_s is the pseudo-second order kinetic rate constant. Using the same boundary conditions as Eq 5.18, the adsorbed amount at any time following pseudo-second order adsorption is given by,

$$q = \frac{q_e^2 k_s t}{1 + q_e k_s t} \tag{5.20}$$

It is important to choose a rate expression which minimizes the error between the final mass-transfer model and experimental data. The k_i and k_s rate constants were calculated from Equations 5.18 and 5.20 by minimizing the SSE between the experimental adsorbed amount, q_{exp}, and the adsorbed amount calculated from Equations 5.18 and 5.20, q_{calc}. Fig 5.6 shows a comparison of the kinetic models to experimental data. We quantified the error between the models and experimental data using the normalized standard deviation, shown in Eq. 5.21.

$$\Delta q = \sqrt{\frac{\Sigma[(q_{exp} - q_{calc})/q_{exp}]^2}{(N-1)}} \times 100\% \tag{5.21}$$

In Eq. 5.21, N is the number of experimental data points. The normalized standard deviation,

Δq, represents the average standard deviation of all points as a percentage. The comparison pictured in Fig 5.6 had Δq values of 16.4% and 47.5% for pseudo-first and -second order fits, respectively. Δq values were found for all iodine experiments, and this trend was apparent for all the experimental data, with the pseudo-first order model correlating with Δq values between 6% and 20%, and the pseudo-second order model having Δq values above 40%. Thus, the pseudo-first order kinetic model is a reasonable approximation, and is used as the adsorption rate term for all calculations.

Knowing how k_i varies with temperature allows us to solve the mass-transfer model to generate calculated BT curves at many temperatures, and makes the model more flexible. Kinetic rate constants are known to vary with temperature according to the Arrhenius equation,

$$k_i = k_0 * e^{\frac{-E_a}{RT}} \tag{5.22}$$

Where k_0 is the pre-exponential, or frequency, factor; E_a is the activation energy of adsorption; R is the universal gas constant, and T is the operating temperature. Linearizing Eq. 5.22 gives,

$$ln(k_i) = ln(k_0) - \left(\frac{E_a}{R}\right)\frac{1}{T} \tag{5.23}$$

From this equation, a plot of $ln(k_i)$ vs. $1/T$ can be used to find k_0 and E_a. Fig. 5.7 shows this plot for single component iodine experiments performed at multiple temperatures with an inlet concentration of 25 ppm; E_a and k_0 were found to be 14.5 kJ/mol and 0.0632 s^{-1}, respectively.

The problem of using pseudo-first order kinetics, whose equation pertains to homogeneous reactions, for the heterogeneous adsorption reaction also needs to be addressed. Adsorption is heterogeneous; however, as noted in Chapter 4, varying the inlet concentration seems to increase the rate of adsorption. Fitting BT curves collected at different inlet concentrations to the rate equation reveals that the rate of adsorption varies linearly with inlet concentration; higher bulk gas concentrations increase adsorption rate. This trend is evidence that the adsorption of iodine and krypton on C/ETS-10 is diffusion limited—meaning that the adsorption rate is limited by a homogeneous phenomena—and can be described by pseudo-first order kinetics. This claim is further supported by iodine having a low activation energy, which indicative of diffusion limited adsorption.

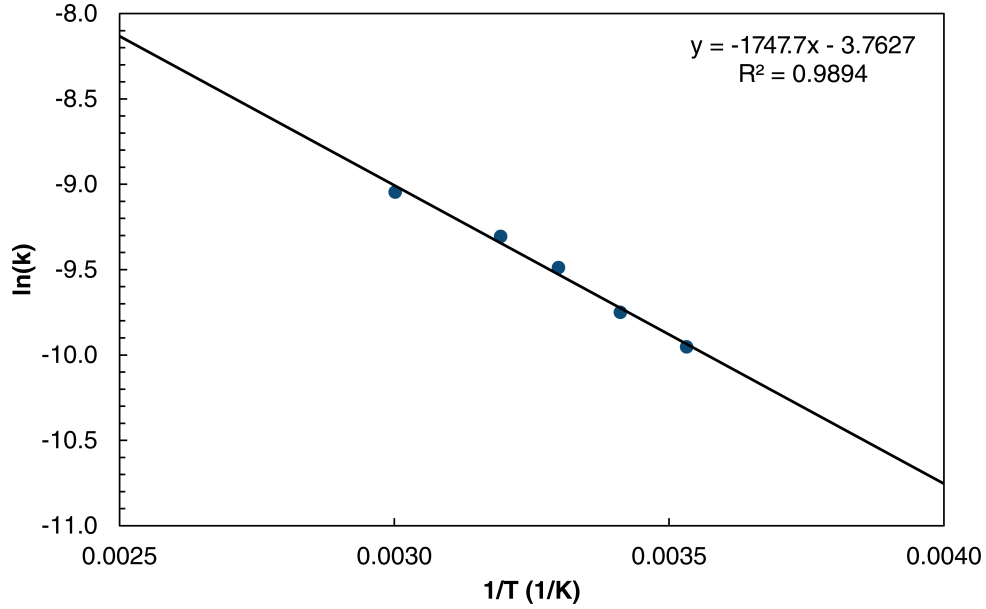

Figure 5.7: $ln(k_i)$ vs. $1/T$ for iodine single component experiments. Inlet concentration of iodine was 25 ppm.

During adsorption, the bulk concentration of contaminant in the off-gas ranges from 0 to C_0 along the sorbent bed; and since q_e varies with bulk concentration, the sorbent capacity at equilibrium—found from the single- and multicomponent experiments—cannot be used for q_e. Instead, we incorporate adsorption thermodynamics by substituting an isotherm equation in the rate of adsorption term, Eq. 5.17, which solves q_e as a function of the bulk concentration. As noted earlier, the Langmuir isotherm presents a more realistic isotherm than the Freundlich, since it imposes a limit to q_e as $C \to \infty$. Therefore, it will be used in the mass-transfer model.

5.3.2 Development of a Numerical Solution

Numerical methods must be used to solve Eq. 5.16, since it cannot be solved analytically. The numerical method solves the partial differential equation by approximating its terms, then solving for the independent variable, C, over discrete increments of the dependent variables, t and z. Eq. 5.16 is solved by approximating its differential terms using the backward divided difference method (BDD)—a truncated Taylor series. The BDD approximations are shown in Equations

5.24 and 5.25.

$$\frac{\partial C(t,z)}{\partial t} \cong \frac{C_i^l - C_i^{l-1}}{\Delta t} \tag{5.24}$$

$$\frac{\partial C(t,z)}{\partial z} \cong \frac{C_i^{l-1} - C_{i-1}^{l-1}}{\Delta z} \tag{5.25}$$

Δz and Δt above are the segment and differential time element lengths, respectively; i and l denote the bulk off-gas concentration length segment and time element, respectively. Fig. 5.8 depicts the adsorption column split into N_z segments of Δz length, and is shown at various saturation levels. The substituted approximations from Equations 5.24 and 5.25 are shown in Eq.

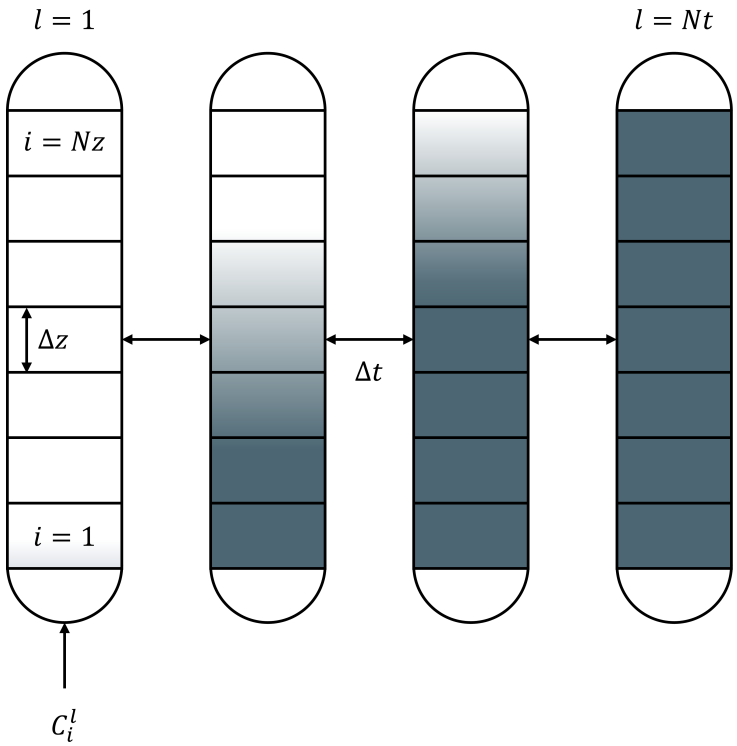

Figure 5.8: Diagram of a fixed-bed adsorption column split into discrete time and length steps. The column length is split into N_z segments of height Δz. Time steps have a duration of Δt. Eq. 5.16 is solved for each length, and time step. The current segment being solved is denoted by i, and the current time step by l.

5.26, and the BDD method is illustrated in Fig. 5.9.

$$\frac{C_i^l - C_i^{l-1}}{\Delta t} = -v\frac{C_i^{l-1}C_{i-1}^{l-1}}{\Delta z} - \rho_b \frac{\partial q}{\partial t}\bigg|_i^l \tag{5.26}$$

The first unknown node, (i, l) in Fig. 5.9 is solved using known quantities, represented by the

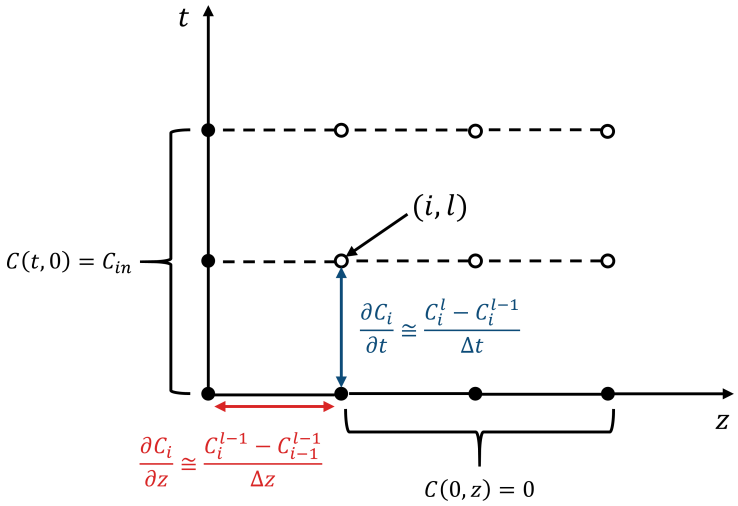

Figure 5.9: Illustration of method to solve Eq. 5.16. Each circle represents a concentration at a segment in the column denoted by i, at a time step denoted by l. The filled circles represent values that are known before any solution is implemented, and the empty circles are concentration values that are unknown.

red and blue arrows, using Eq. 5.26. Once the concentration at (i, l) is known, node $(i + 1, l)$ can be solved for. This is repeated to solve concentrations for all i at time step l. The time step is incremented to $l + 1$, and bulk concentration can again be solved for all length segments. These steps are repeated until the bulk concentration is known for all i and l.

When carrying out this numerical solution, the rate of adsorption term from Eq. 5.16 is evaluated at the concentration node currently being solved; this is shown by Eq. 5.27.

$$\left.\frac{\partial q}{\partial t}\right|_i^l = k_i(q_e - q_i^l) \tag{5.27}$$

In Eq. 5.27, q_i^l is the amount of contaminant adsorbed in segment i at time step l, and is estimated by Euler's method, as shown in Eq. 5.28.

$$q_i^l = q_i^{l-1} + k_i(q_e - q_i^l)\Delta t \tag{5.28}$$

Solving Eq. 5.28 for q_i^l yields,

$$q_i^l = \frac{q_i^{l-1} + q_e k_i \Delta t}{1 + k_i \Delta t} \tag{5.29}$$

Eq. 5.29 is then substituted into Eq. 5.27 to get,

$$\left.\frac{\partial q}{\partial t}\right|_i^l = k_i \left(q_e - \frac{q_i^{l-1} + q_e k_i \Delta t}{1 + k_i \Delta t} \right) \tag{5.30a}$$

Simplifying yields,

$$\left.\frac{\partial q}{\partial t}\right|_i^l = \frac{k_i}{1 + k_i \Delta t} \left(q_e - q_i^{l-1} \right) \tag{5.30b}$$

and further substituting Eq. 5.3, the Langmuir isotherm equation, in for q_e yields,

$$\left.\frac{\partial q}{\partial t}\right|_i^l = \frac{k_i}{1 + k_i \Delta t} \left(\frac{q_m K_L C_i^l}{1 + K_L C_i^l} - q_i^{l-1} \right) \tag{5.30c}$$

Now that we have obtained $\frac{\partial q}{\partial t}$ in terms of C_i^l and q_i^{l-1}—a known quantity—Eq. 5.30c can be substituted into Eq. 5.26 to obtain Eq. 5.31.

$$\frac{C_i^l - C_i^{l-1}}{\Delta t} = -v \frac{C_i^{l-1} C_{i-1}^{l-1}}{\Delta z} - \rho_b \frac{k_i}{1 + k_i \Delta t} \left(\frac{q_m K_L C_i^l}{1 + K_L C_i^l} - q_i^{l-1} \right) \tag{5.31}$$

To make Eq. 5.31 simpler, the following substitutions are made.

$$\lambda = v \frac{\Delta t}{\Delta z} \tag{5.32a}$$

$$B = \frac{\rho_b k_i \Delta t}{1 + k_i \Delta t} \tag{5.32b}$$

$$C_i^l = \alpha \tag{5.32c}$$

$$C_i^{l-1} = \beta \tag{5.32d}$$

$$C_{i-1}^{l-1} = \gamma \tag{5.32e}$$

$$q_i^{l-1} = \delta \tag{5.32f}$$

λ from Eq. 5.32a is a typical parameter in numerical solutions is a stability factor. If $\lambda \leq 1/2$ is not satisfied, then the PDE solution can either oscillate or not converge. To prevent this, a

loop updating λ to meet this condition was implemented in the MATLAB code, and is shown in Appendix I. Substituting Equations 5.32a – 5.32f into Eq. 5.31 gives,

$$\alpha - \beta = -\lambda(\beta - \gamma) - \rho_b \Delta t \left[\frac{k_i}{1 + k_i \Delta t} \left(\frac{K_L q_m \alpha}{1 + K_L \alpha} - \delta \right) \right] \tag{5.33}$$

Which can be put into the quadratic form,

$$\alpha^2(K_L) + \alpha K_L \left(\beta(\lambda - 1) - \lambda\gamma + B(q_m - \delta) + \frac{1}{K_L} \right) - (\beta(1 - \lambda) + \lambda\gamma + B\delta) = 0 \tag{5.34}$$

Finally, C_i^l can be solved using the quadratic equation.

$$\alpha = C_i^l = \frac{-b \pm \sqrt{b^2 - 4ac}}{2a} \tag{5.35}$$

Where,

$$a = K_L \tag{5.36}$$

$$b = K_L \left(\beta(\lambda - 1) - \lambda\gamma + B(q_m - \delta) + \frac{1}{K_L} \right) \tag{5.37}$$

and

$$c = -\left(\beta(1 - \lambda) + \lambda\gamma + B\delta\right) \tag{5.38}$$

5.4 Mass-Transfer Model Results

Fig. 5.10 shows a comparison of the numerically solved mass-transfer model and experimental data BT curves for single component and multicomponent iodine experiments. As with the Thomas and Yoon-Nelson models, the mass-transfer model fits single component data better than the multicomponent data. Each example in Fig. 5.10 is representative of the mass-transfer model fit for all iodine experiments; the mass-transfer model fits single component experiments

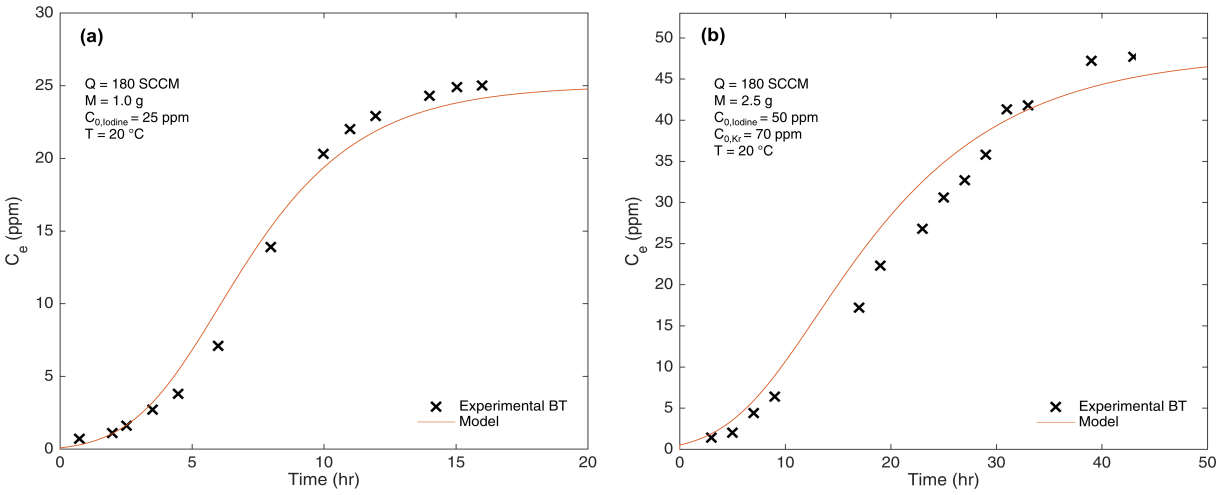

Figure 5.10: Mass-transfer model fit of experimental iodine BT curves. (a) Single component and (b) multicomponent. Experimental conditions are listed within the figure.

well, but does not fit the top and bottom of the 'S' curve for multicomponent experiments as closely. Some of the misfit is corrected by inputting inlet concentration as a function of time into the mass-transfer model—accounting for inlet concentration drift—but some discrepancies remain. We performed a parametric study to investigate these discrepancies.

5.4.1 Parametric Study of the Mass-Transfer Model

It is necessary to examine the sensitivity of the mass-transfer model generated BT curves to changing kinetic and thermodynamic parameter. A parametric study was done varying k_0, E_a, q_m, and K_L by percentages of their experimentally calculated values. The results are detailed in Fig. 5.11. Fig. 5.11a and b show how the mass-transfer model changes with the kinetic rate constant parameters k_0 and E_a. As expected, higher values of the rate constant increase the slope of the BT curve. Increasing the rate constant through both parameters increases the overall rate of adsorption; the sorbent reaches equilibrium faster, and the length of the MTZ decreases. The mass-transfer model shows a similar response to changes in pre-exponential factor and activation energy, though is much more sensitive to activation energy changes, as it is contained in the exponential term.

Changes in the isotherm parameters q_m and K_L did not change the shape of the BT curve significantly, but rather, shifted it. Increasing q_m by 50% maintained the curve shape, but the exhaustion time increased by four hours; decreasing q_m 50% lowered the exhaustion time by

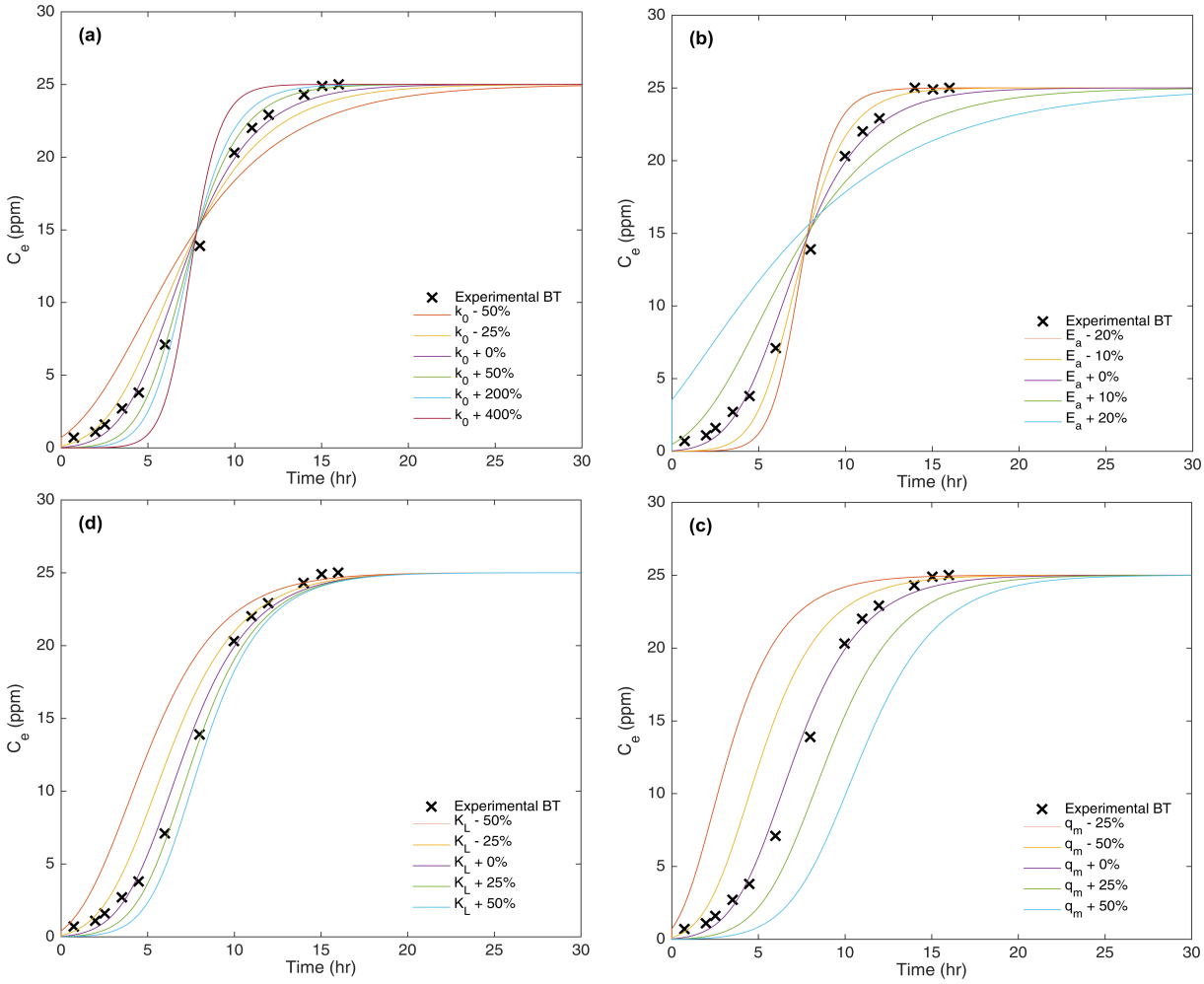

Figure 5.11: Parametric study showing the effect of varying the (a) pre-exponential factor, (b) activation energy, (c) maximum adsorption capacity, and (d) the Langmuir equilibrium constant on the shape of the mass-transfer based model

four hours. Varying the Langmuir equilibrium constant, K_L, shifted the curve similarly—higher values increased exhaustion time. However, the main effect of changing K_L was on the shape of the bottom of the 'S' curve. This occurs because K_L is related to the rate of sorption, not the capacity. Higher values of the Langmuir equilibrium constant translate to a higher rate of sorption—primarily during the beginning of the experiment when the driving force, $q_e - q$, for adsorption is greatest. The higher sorption rate keeps the effluent concentration lower for longer, but the outlet concentration increases at a higher rate overall.

The effect of these parameters divulges why experimental data deviates from the model. There are two likely explanations for the deviation of the model from experimental results seen in Fig. 5.10b. Firstly, the pseudo-first order kinetic model may not approximate this adsorption accu-

rately; Fig. 5.6 show the pseudo-first order fit to undercut the experimental data near the exhaustion time. Secondly, inaccurate representation of the equilibrium constant. In our model we use the Langmuir equilibrium constant which relates the equilibrium concentration of the bulk to the adsorbed phase. However, the Langmuir equilibrium constant is idealized from the original definition of the equilibrium constant defined in Eq. 5.39.

$$K = \prod_i (a_i)^{\nu_i} \tag{5.39}$$

Eq. 5.39 defines the equilibrium constant on an activity basis, where K is the equilibrium constant, a_i is the activity of component i, and ν_i is the stoichiometric coefficient of component i. Many researchers have commented on the fallacy in using the Langmuir equilibrium constant to predict isotherms [98–103]. However, modification of the Langmuir equation—such as to the extended Langmuir equation which includes multiple components as part of its derivation—can alter the mass-transfer model to fit experimental BT suitably for industrial modeling application.

$$q_{e,i} = \frac{q_{m,i} K_{L,i} C_i}{1 + \sum_{i=1}^{n} K_{L,i} C_i} \tag{5.40}$$

In Eq. 5.40, the subscript i denotes a specific contaminant, and n is the number of contaminants. Temperature dependence is included in Eq. 5.40 through the equilibrium constant;

$$K_{L,i}(T) = K_{L,i0} e^{\frac{-H_{ads,i}}{RT}} \tag{5.41}$$

where $-H_{ads,i}$ is the heat of adsorption for contaminant i, and $K_{L,i0}$ is the standard state Langmuir equilibrium constant. The unknowns in Equations 5.40 and 5.41 can be found by performing experiments over a wide range of temperatures and bulk gas concentrations.

If we account for the iodine inlet concentration drift and alter the experimentally calculated Langmuir equilibrium constant by +60%, the mass-transfer model's fit increases significantly as shown in Fig. 5.12. Following these observations, collecting data at a wider range of conditions to fit more rigorous thermodynamic and kinetic models to use within the mass-transfer model is highly recommended.

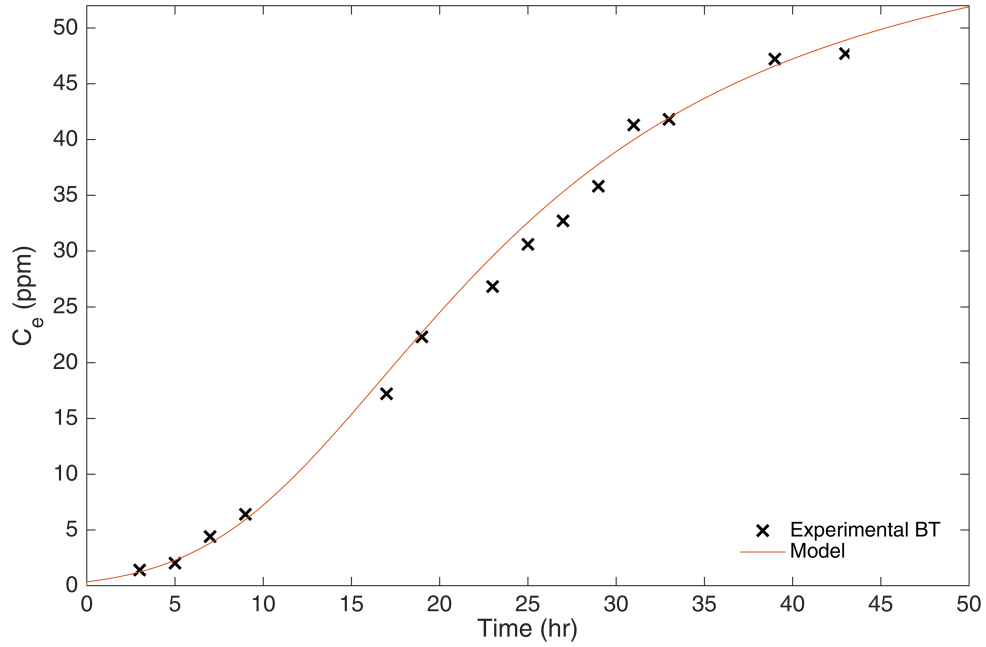

Figure 5.12: Mass-transfer model fit to the breakthrough curve of multicomponent iodine. The Langmuir equilibrium constant has been corrected, and experimental iodine inlet feed concentration drift accounted for.

Chapter 6: Summary & Conclusions

6.1 Summary

Nuclear reprocessing is key in making nuclear energy sustainable in the future. Increasing the feasibility, and safety is the core motivation behind our research presented in this thesis. We studied adsorption on 10 wt% C/ETS-10 sorbent we have synthesized by performing adsorption experiments with iodine and krypton at ambient temperatures and realistically low bulk contaminant concentrations.

Iodine sorption capacities for the 10 wt% C/ETS-10 ranged from 27.9 to 49.5 mg/g, and krypton sorption capacities ranged from 0.29 to 0.75 mmol/kg (0.024–0.063 mg/g). Past research on the adsorption of iodine and krypton is difficult to reconcile with our own results because studies use many different, pressures, temperatures, and off-gas constituents; however, a few studies performed near the conditions that were used in this research can give some perspective. AgZ is one of the top sorbents for iodine sorption and a study comparable to our own was performed by Patton et al. in 2014 [28]. Patton performed dynamic adsorption experiments with an iodine inlet concentration of 50 ppm at 150 °C (the optimum temperature for iodine sorption on silver) and found that AgZ had an iodine sorption capacity of 72 mg/g. For krypton, HZ and the MOF Ni/DOBDC are two of the forefront sorbents currently being studied. Our own 10 wt% C/ETS-10 exhibits 130% the HZ krypton capacity reported by Greenhalgh et al. [56], who used a 150 ppm krypton inlet stream with 79% nitrogen at cryogenic temperatures. The C/ETS-10 also exhibits a much higher capacity than the 0.0055 mg/g exhibited by Ni/DOBDC in a study by Liu et al. [62] which was carried out with a 40 ppm krypton inlet in air at 25 °C. Provided these comparisons, 10 wt% C/ETS-10 is a viable sorbent that warrants further research for future UNF reprocessing off-gas applications.

6.2 Future Work

Two main areas would benefit from further studies: experimental studies, and mass-transfer model development. Currently, adsorption/desorption cycle experiments are being performed to investigate how well the sorbent retains iodine and krypton which is important to predict how the sorbent might fare in storage conditions.

Experiments conducted over a wider range of bulk concentrations to generate more complete isotherms to bolster the mass-transfer model as wells as provide more data to compare with other vanguard sorbents. Further multicomponent experiments, especially at higher bulk concentrations, should be performed to illuminate more about how krypton and iodine affect the sorption of each other.

A major goal of this work was to perform capture of iodine and krypton under realistic conditions. In pursuit of this information, more experiments at higher temperatures and with contaminants such as Xe and nitrogen oxides are recommended.

The mass-transfer model developed to predict adsorption breakthrough curves closely fit experimental data while providing a way to incorporate thermodynamics and kinetics. This made a more robust model able to be used for scale-up. However, there is room to refine the mass-transfer model. Redefining the isotherm used to calculate the equilibrium concentrations between the gas phase and sorbent to include a multicomponent aspect such as the extended Langmuir isotherm does would add another degree of complexity to the model. This could make the model fit experimental data more closely as well as help in the understanding of the multicomponent adsorption process. Finally, the model can be extended to output adsorption column requirements.

Appendix I: Mass-Transfer Model MATLAB Code

```
m=1;                                % Mass of sorbent in grams
F=180;                              % Flow in SCCM
T=283.15;                           % Temperature of column in K
L=1;                                % Bed height in cm
r=2.54/2;                           % Radius of column in cm

rhosorbent=m/(L*pi*r^2)*1000;       % Bed density in g/L
nu=F/(pi*r^2)/60;                   % Superficial gas velocity in
    cm/s
tau=L/nu;                           % Residence time in seconds

Nz=10;                              % Number of segments
dz=L/Nz;                            % Height of segment in cm
z=0:dz:L;                           % Position vector

tfh=20;                             % Total experiment time in hr
tfs=tfh*3600;                       % Total experiment time in
    seconds
Nt=50;                              % Number of time steps
dt=tfs/Nt;                          % Length of time step in
    seconds
dth=tfh/Nt;                         % Length of time step in hr
t=dth:dth:tfh;                      % Time vector in hours

lambda=nu*dt/dz;                    % Relaxation factor

while lambda>0.4                    % Update lambda for stability
    Nt=Nt*2;
    dt=tfs/Nt;
```

```
27          lambda=nu*dt/dz;
28          dth=tfh/Nt;
29          t=dth:dth:tfh;
30  end
31
32  Cin=linspace(25,25,Nt);          % Inlet concentration in ppm
33  Cin=Cin/22.4e6;                  % Inlet concentration in mol/L
34  C=zeros(1,Nz);                   % Concentration vector along
        column
35  Cout=zeros(5,Nt);                % Outlet concentration over
        time
36
37  MWI=126.9*2;                     % Molecular mass of iodine in
        g/mole
38  qmw=40;                          % Monolayer capacity in mg/g
39  qm=qmw/1000/MWI;                 % Monolayer capacity in mol/g
40  Kl=1.6e6;                        % Langmuir equilibrium
        constant in L/mole I
41  ko=0.0632;                       % Pre exponential factor in 1/
        s
42  Ea=14532;                        % Activation energy in J/mol
43  R=8.3145;                        % Universal gas const. in J/
        molK
44  k=ko*exp(-Ea/(R*T));             % Adsorption rate constant in
        1/s
45  qold=0;                          % Initialize the adsorbed
        amount
46  q=zeros(1,Nz);                   % Adsorbed amount over the
        column
47  B=rhosorbent*dt*k/(1+k*dt);      % Constant used in calculation
48
```

```
for l=2:Nt                          % Iterate time step
    for i=2:Nz                      % Iterate spatial step
        if i==2                     % C1=C(i-1,l-1), C2=C(i,l-1)
            C1=Cin(l);              % Bulk concentration is Cin at
                the begining of the column
        else
            C1=C2;
        end

        if l==2
            C2=0;
            qold=0;                 % Adsorbed amount is 0 at time
                0
        else
            C2=C(i);
            qold=q(i);              % qold=q(i,l-1), current
               segement, previous time
        end

        quadA=Kl;                   % Quadratic coefficients
        quadB=Kl*(C2*(lambda-1)-lambda*C1+B*(qm-qold)+(1/Kl));
        quadC=-(C2*(1-lambda)+lambda*C1+B*qold);

        C(i)=(-quadB+sqrt(quadB^2-4*quadA*quadC))/(2*quadA); %
           solve for bulk concentration at i,l
        qe=qm*Kl*C(i)/(1+Kl*C(i)); % Equilibrium adsorption
           amount. Based on bulk concentration at i,l.
        q(i)=qold+k*(qe-qold)*dt; % Calculate adsorbed amount
           at current time and segment based on i,l-1.

    end
```

```
74        Cout(1,l)=C(Nz); % Store concentration at outlet to plot
              breakthrough
75    end
```

References

[1] *International energy outlook 2013*. Tech. rep. DOE/EIA-0484(2013). Washington, DC: U.S. Energy Information Administration, July 2013.

[2] *Levelized cost and levelized avoided cost of new generation resources in the annual energy outlook 2017*. Tech. rep. Washington, DC: U.S. Energy Information Administration, Apr. 2017.

[3] *Projected costs of generating electricity 2015 edition*. Tech. rep. NEA No. 7057. Issy-les-Moulineaux, France: Nuclear Energy Agency, July 1980.

[4] *Processing of used nuclear fuel*. 2016. URL: http://www.world-nuclear.org/information-library/nuclear-fuel-cycle/fuel-recycling/processing-of-used-nuclear-fuel.aspx.

[5] IAEA. "Energy, Electricty and Nuclear Power Estimates for the Perid Up to 2050". 1 (2013).

[6] R. Jubin. "Spent Fuel Reprocessing". *Introduction to nuclear chemistry and fuel cycle separations course* (2008), p. 22.

[7] *Removal, storage, and disposal of gaseous radionuclides from airborne effluents*. Tech. rep. IAEA-209. Vienna: International Atomic Energy Agency, 1976.

[8] P. Paviet-Hartmann, W. Kerlin, and B. Steven. "Treatment of Gaseous Effluents Issued from Recycling — A Review of the Current Practices and Prospective Improvements". *Nea/oecd workshop on actinide and fission product partioning and transmutation exchange meeting*. San Francisco, CA, 2010.

[9] N. R. Soelberg et al. "Radioactive Iodine and Krypton Control for Nuclear Fuel Reprocessing Facilities". *Science and technology of nuclear installations* 2013 (2013), pp. 1–12.

[10] D. R. Haefner and T. J. Tranter. *Methods of gas phase capture of iodine from fuel reprocessing off-gas: a literature survey*. Idaho National Laboratory Tech. Report INL/EXT-07-12299. Idaho Falls, Idaho: Idaho National Laboratory, Feb. 2007.

[11] L. G. Trevorrow et al. *Compatibility of technologies with regulation in the waste management of h-3, i-129, c-14, and kr-85. part i. initial information use*. Argonne National Laboratory Tech. Manual ANL-83-57. Argonne, Illinois: Argonne National Laboratory, Aug. 1983.

[12] T. L. D., L. M. Toth, and E. D. Collins. *Molten hyrdroxide trapping process for radioiodine*. Oak Ridge National Laboratory Tech. Manual ORNL/TM-2002/247. Oak Ridge, Tennessee: Oak Ridge National Laboratory, Jan. 2003.

[13] R. T. Jubin. *A literature survey of methods to remove iodine from off-gas streams using solid sorbents*. Oak Ridge National Laboratory Tech. Manual ORNL/TM-6607. Oak Ridge, Tennessee: Oak Ridge National Laboratory, Mar. 1979.

[14] D. W. Holladay. *A literature survey: methods for the removal of iodine species from off-gases and liquid waste streams of nuclear power and nuclear fuel reprocessing plants*. Oak Ridge Laboratory Tech. Manual ORNL/TM-6350. Oak Ridge, Tennessee: Oak Ridge National Laboratory, Jan. 1979.

[15] *Separation, storage and disposal of krypton-85*. Tech. rep. Technical Report Series No. 199. Vienna: International Atomic Energy Agency, 2015.

[16] P. R. Monson. *Krypton retention on solid sorbents*. Savannah River Laboratory Tech. Report DP-1615. Aiken, South Carolina: Savannah River Laboratory, Jan. 1982.

[17] D. M. Strachan. "Processes for Removal and Immobilization of C , I , and Kr". September (2009), p. 2010.

[18] H. Shaw. *Determination of the open and closed porosity in an immobilized pu ceramic wasteform*. Tech. Report UCRL-ID-132605. Livermore, CA: Lawrence Livermore National Laboratory, 1998.

[19] H. Sun et al. "Capture and reversible storage of volatile iodine by porous carbon with high capacity". *Journal of materials science* 50.22 (2015), pp. 7326–7332.

[20] R. E. Adams et al. *The release and adsorption of methyl iodide in the hfir maximum credible accident*. Tech. Report ORNL/TM-1291. Oak Ridge, TN: Oak Ridge National Laboratory, 1965.

[21] B. S. Choi et al. "Adsorption equilibrium and dynamics of methyl iodide in a silver ion-exchanged zeolite column at high temperatures". *Adsorption* 7.2 (2001), pp. 91–103.

[22] H. Deuber. "Investigations on the retention of elemental radioiodine by activated carbons at high temperatures". *Nuclear technology* 72.1 (1986), vp.

[23] D. M. Ruthven. *Principles of adsorption and adsorption processes*. 1984.

[24] W. J. Maeck, D. T. Pence, and K. J. H. *A highly efficient inorganic adsorber for airborne iodine species (silver zeolite development studies)*. Tech. rep. IN-1224. Idaho Falls, Idaho: Idaho Nuclear Corporation, Oct. 1968.

[25] B. Puppe and W. Jürgen. "Process for the removal of iodine and organic iodine compounds from gases and vapors using silver-containing zeolite of the faujasite type". 4,913,850. 1990.

[26] C. M. Slansky et al. *Lwr fuel reprocessing and recycle progress report for july 1–september 30, 1979*. Tech. Report ICP-1108. Idaho Falls, ID: Idaho National Laboratory, 1976.

[27] R. T. Jubin. "Organic Iodine Removal From Simulated Dissolver OFF-Gas Streams Using Silver-Exchanged Mordenite". *16th doe nuclear air cleaning conference* (1980).

[28] K. K. Patton et al. *Iodine loading of no aged silver exchanged mordenite*. Fuel Cycle R & D ORNL/LTR-2014/425. Oak Ridge, Tennessee: Oak Ridge National Laboratory, Aug. 2014.

[29] T. M. Nenoff et al. "Silver-mordenite for radiologic gas capture from complex streams: Dual catalytic CH_3I decomposition and I confinement". *Microporous and mesoporous materials* 200 (2014), pp. 297–303.

[30] Q.-H. Cheng, Z.-J. Li, and T.-W. Chu. "Adsorption of gaseous iodine-131 at high temperatures by silver impregnated alumina". *Nuclear science and techniques* 26.4 (2015), pp. 1–5.

[31] T. Fukasawa, K. Funabashi, and Y. Kondo. "Separation technology for radioactive iodine from off-gas streams of nuclear facilities". *Science and technology* 3131.April 2013 (1994), pp. 37–41.

[32] J. G. Moore and W. B. Howerton. *Lmfbr fuel cycle studies progress report for september 1970, no. 17*. Tech. Report ORNL/TM-3095. Oak Ridge, TN: Oak Ridge National Laboratory, 1970.

[33] S. Sarri et al. "Removal of iodide from aqueous solutions by polyethylenimine-epichlorohydrin resins". English. *Journal of radioanalytical and nuclear chemistry* 298.1 (2013), pp. 399–403.

[34] S. A. Kandil et al. "An improvement of radioiodine separation from tellurium oxide target through the bed depth of ion-exchanger". *Journal of radioanalytical and nuclear chemistry* 293.1 (2012), pp. 75–79.

[35] C. Decamp and S. Happel. "Utilization of a mixed-bed column for the removal of iodine from radioactive process waste solutions". *Journal of radioanalytical and nuclear chemistry* 298.2 (2013), pp. 763–767.

[36] B. J. Riley et al. "Chalcogen-based aerogels as a multifunctional platform for remediation of radioactive iodine". *Rsc advances* 1.9 (2011), pp. 1704–1715.

[37] B. J. Riley et al. "Chalcogen-based aerogels as sorbents for radionuclide remediation". *Environmental science and technology* 47.13 (2013), pp. 7540–7547.

[38] K. S. Subrahmanyam et al. "Chalcogenide aerogels as sorbents for radioactive iodine". *Chemistry of materials* 27.7 (2015), pp. 2619–2626.

[39] J. J. Perry et al. "Noble gas adsorption in metal-organic frameworks containing open metal sites". *Journal of physical chemistry c* 118.22 (2014), pp. 11685–11698.

[40] D. F. Sava et al. "Capture of volatile iodine, a gaseous fission product, by zeolitic imidazolate framework-8". *Journal of the american chemical society* 133.32 (2011), pp. 12398–12401.

[41] K. W. Chapman, G. J. Halder, and P. J. Chupas. "Pressure-induced amorphization and porosity modification in a metal- organic framework". *Journal of the american chemical society* 131.48 (2009), pp. 17546–17547.

[42] K. MUNAKATA, T. SHINOZAKI, and H. OKABE. "Adsorption of Krypton on Adsorbents at Cryogenic Temperatures". *Journal of power and energy systems* 2.1 (2008), pp. 171–177.

[43] A. Dillon et al. "Storage of hydrogen in single-walled carbon nanotubes". *Nature* 386 (1997), pp. 377–379.

[44] S. Talapatra et al. "Gases do not adsorb on the interstitial channels of closed-ended single-walled carbon nanotube bundles". *Physical review letters* 85.1 (2000), pp. 138–141.

[45] M. R. Babaa et al. "Opening of single-walled carbon nanotubes: Evidence given by krypton and xenon adsorption". *Surface science* 531.1 (2003), pp. 86–92.

[46] M. Muris et al. "Methane and krypton adsorption on single-walled carbon nanotubes". *Langmuir* 16.17 (2000), pp. 7019–7022.

[47] M. Foroutan and A. Taghavi Nasrabadi. "Adsorption and separation of binary mixtures of noble gases on single-walled carbon nanotube bundles". *Physica e: low-dimensional systems and nanostructures* 43.4 (2011), pp. 851–856.

[48] S. Jalili and R. Majidi. "Study of Xe and Kr adsorption on open single-walled carbon nanotubes using molecular dynamics simulations". *Physica e: low-dimensional systems and nanostructures* 39.1 (2007), pp. 166–170.

[49] J. Liu, P. K. Thallapally, and D. Strachan. "Metal-organic frameworks for removal of XE and KR from nuclear fuel reprocessing plants". *Langmuir* 28.31 (2012), pp. 11584–11589.

[50] K. Munakata. "Vacancy Solution Model Formulated by the NRTL Equation for Correlation of Adsorption Equilibria". *Journal of chemical engineering of japan* 40.5 (2007), pp. 398–409.

[51] R. E. Bazan et al. "Adsorption equilibria of O2, ar, kr and xe on activated carbon and zeolites: Single component and mixture data". *Adsorption* 17.2 (2011), pp. 371–383.

[52] S. Kitani and J. Takada. "Adsorption of Krypton and Xenon on Various Adsorbents". *Journal of nuclear science and technology* 2.2 (1965), pp. 51–56.

[53] D. Ianovski et al. "Adsorption of noble gases on h-mordenite". *Journal of nuclear science and technology* 39 (2002), pp. 1213–1218.

[54] T. G. Garn, M. R. Greenhalgh, and J. D. Law. *Novel sorbent development and evaluation for the capture of krypton and xenon from nuclear fuel reprocessing off-gas streams*. Idaho National Laboratories Preprint INL/CON-13-29010. Idaho Falls, Idaho: Idaho National Laboratory, Oct. 2013.

[55] C. Daniel et al. "Xenon capture on silver-loaded zeolites: Characterization of very strong adsorption sites". *Journal of physical chemistry c* 117.29 (2013), pp. 15122–15129.

[56] M. Greenhalgh, T. G. Garn, and J. D. Law. "Development of a hydrogen mordenite sorbent for the capture of krypton from used nuclear fuel reprocessing off-gas streams". *Journal of nuclear science and technology* 51.4 (2014), pp. 476–481.

[57] U. Mueller et al. "Metal–organic frameworks—prospective industrial applications". *J. mater. chem.* 16.7 (2006), pp. 626–636.

[58] A. Soleimani Dorcheh et al. "Noble gases and microporous frameworks; From interaction to application". *Microporous and mesoporous materials* 162 (2012), pp. 64–68.

[59] C. J. Jameson, A. K. Jameson, and H.-M. Lim. "Competitive adsorption of xenon and krypton in zeolite NaA: ^{129}Xe nuclear magnetic resonance studies and grand canonical Monte Carlo simulations". *The journal of chemical physics* 104.4 (1996), p. 1709.

[60] B. J. Sikora et al. "Thermodynamic analysis of Xe/Kr selectivity in over 137000 hypothetical metal–organic frameworks". *Chemical science* 3.7 (2012), pp. 2217–2223.

[61] P. Ryan et al. “Computational screening of metal-organic frrameworks for xenon/krypton separation”. *Aiche journal* 57 (7 2011).

[62] J. Liu, D. M. Strachan, and P. K. Thallapally. “Enhanced noble gas adsorption in Ag@MOF-74Ni.” *Chemical communications (cambridge, england)* 50.4 (2014), pp. 466–468.

[63] C. A. Fernandez et al. “Switching Kr/Xe selectivity with temperature in a metal-organic framework”. *Journal of the american chemical society* 134.22 (2012), pp. 9046–9049.

[64] Y. Zhu et al. “Low temperature preparation of hollow carbon nano-polyhedrons with uniform size, high yield and graphitization”. *Materials chemistry and physics* 134.2-3 (2012), pp. 639–645.

[65] Z. Ji. “Synthesis and engineering of titanosilicate ETS-10 for enhanced photocatalytic activity in an optical fiber reactor” (2009).

[66] S. M. Kuznicki, H. M. Garfinkel, and K. A. Thrush. “Use of crystalline molecular sieves containing charged octahedral sites in cyclic desiccating processes”. 9300152. 1993.

[67] B. Tanchuk et al. “Adsorptive drying of {co2} using low grade heat and humid, ambient air”. *Separation and purification technology* 120 (2013), pp. 354–361.

[68] C. C. Pavel et al. “The sorption of some radiocations on microporous titanosilicate ETS-10”. *Journal of radioanalytical and nuclear chemistry* 258.2 (2003), pp. 243–248.

[69] L. Liu et al. “Synthesis and adsorption properties of titanosilicates ETS-4 and ETS-10 from fly ash”. *Journal of hazardous materials* 195 (2011), pp. 340–345.

[70] N. A. Al-Baghli and K. F. Loughlin. “Binary and ternary adsorption of methane, ethane, and ethylene on titanosilicate ETS-10 zeolite”. *Journal of chemical and engineering data* 51.1 (2006), pp. 248–254.

[71] A. Ansòn et al. “Adsorption of argon, oxygen, and nitrogen on silver exchanged ETS-10 molecular sieve”. *Microporous and mesoporous materials* 109.1-3 (2008), pp. 577–580.

[72] S. M. Kuznicki et al. “Xenon adsorption on modified ETS-10”. *Journal of physical chemistry c* 111.4 (2007), pp. 1560–1562.

[73] S. M. Kuznicki. “Large-pored crystalline titanium molecular sieve zeolites”. 4853202. 1989.

[74] M. W. Anderson et al. “Microporous titanosilicate ets-10: a structural survey”. *Philosophical magazine part b* 71.5 (1995), pp. 813–841.

[75] H. Liu et al. “Engelhard titanosilicate-1 and engelhard titanosilicate-2 as promising adsorbents in multivalence heavy metal removal”. *Journal of environmental chemical engineering* 3.2 (2015), pp. 1081–1087.

[76] L. Wu et al. “Iodine adsorption on silver-exchanged titania-derived adsorbents”. *Journal of radioanalytical and nuclear chemistry* 302.1 (2014), pp. 527–532.

[77] C. N. He et al. "Study of aluminum powder as transition metal catalyst carrier for cvd synthesis of carbon nanotubes". *Materials science and engineering a - structural materials properties microstructure and processing* 441.1 (2006), pp. 266–270.

[78] X. Yang et al. "Synthesis of microporous titanosilicate ETS-10 with TiF4 or TiO2". *Microporous and mesoporous materials* 46.1 (2001), pp. 1–11.

[79] J. Hodkiewicz and T. F. Scientific. "Characterizing Carbon Materials with Raman Spectroscopy". *Application note: 51901* (210), pp. 1–5. eprint: 0508657.

[80] A. C. Ferrari et al. "Raman spectrum of graphene and graphene layers". *Physical review letters* 97.18 (2006), pp. 1–4. arXiv: 0606284v1 [cond-mat].

[81] Y. Su, M. L. Balmer, and B. C. Bunker. "Raman spectroscopic studies of silicotitanates". *Journal of physical chemistry b* 104.509 (2000), pp. 8160–8169.

[82] P. D. Southon and R. F. Howe. "Spectroscopic studies of disorder in the microporous titanosilicate ETS-10". *Chemistry of materials* 14.10 (2002), pp. 4209–4218.

[83] J. Rocha et al. "Synthesis of microporous titanosilicate ets-10 from $ticl_3$ and tio_2: a comprehensive study". *Microporous mesoporous materials* 23 (1998), pp. 253–263.

[84] K. P. Prasanth et al. "Hydrogen sorption in transition metal modified ETS-10". *International journal of hydrogen energy* 34.2 (2009), pp. 888–896.

[85] A. D. Clesceri, L. S. Greenberg, and A. E. Franson. *Standard methods for the examination of water and wastewater, 20th ed.* Tech. rep. 20th Ed. Washington, D.C.: American Public Health Association, 1998.

[86] M. Fleischmann, P. J. Hendra, and J. Robinson. "X-ray diffraction from adsorbed iodine on graphite". *Nature* 288.13 (1980), pp. 152–153.

[87] M. S. Refa, W. F. El-Hawary, and M. A. Moussa. "Ir, ^{1}h nmr, mass, xrd, and tga/dta investigations on the cirprofloxacin/iodine charge-transfer complex". *Spectrochimica acta part a: molecular and biomolecular spectroscopy* 78 (2011), pp. 1356–1363.

[88] H. C. Thomas. "Heterogeneous ion exchange in a flowing system". *Journal of the american chemical society* 66.2 (1944), pp. 1664–1666.

[89] Z. Xu, J.-G. Cai, and B.-C. Pan. "Mathematically modeling fixed-bed adsorption in aqueous systems". *Journal of zhejiang university-science a (applied physics & engineering)* 14.3 (2013), pp. 155–176.

[90] S. Biswas and U. Mishra. "Continuous Fixed-Bed Column Study and Adsorption Modeling: Removal of Lead Ion from Aqueous Solution by Charcoal Originated from Chemical Carbonization of Rubber Wood Sawdust". *Journal of chemistry* 2015 (2015).

[91] Y. A. Mustafa and S. E. Ebrahim. "Utilization of Thomas Model To Predict the Breakthrough Curves for Adsorption and Ion". 16.4 (2010), pp. 6206–6223.

[92] A. Ghribi and M. Chlendi. "Modeling of Fixed Bed Adsorption: Application to the Adsorption of an Organic Dye". *Asian journal of textile* 1.4 (Apr. 2011), pp. 161–171.

[93] G. Bohart and E. Q. Adams. "Some aspects of the behavior of charcoal with respect to chlorine". *J. am. chem.* 42 (1920), pp. 523–529.

[94] Z. Z. Chowdhury et al. "Breakthrough curve analysis for column dynamics sorption of Mn(II) ions from wastewater by using Mangostana garcinia peel-based granular-activated carbon". *Journal of chemistry* 2013.Ii (2013).

[95] F. Karpowicz, J. Hearn, and M. C. Wilkinson. "The quantitative use of the Bohart-Adams equation to describe effluent vapour profiles from filter beds". *Carbon* 33.11 (1995), pp. 1573–1583.

[96] G. Song et al. "An investigation of CO2 adsorption kinetics on porous magnesium oxide". *Chemical engineering journal* 283 (2016), pp. 175–183.

[97] S. Lagergren. "Zur theorie der sogenannten adsorption gelöster stoffe". *Handl* 24 (1898).

[98] P. N. Diagboya et al. "Graphene oxide–tripolyphosphate hybrid used as a potent sorbent for cationic dyes". *Carbon* 79 (2014), pp. 174–182.

[99] Y. Liu. "Is the free energy change of adsorption correctly calculated?" *Journal of chemical & engineering data* 54.7 (2009), pp. 1981–1985.

[100] S. Dikmen et al. "Determination of equilibrium, kinetic and thermodynamic parameters of acid red 88 adsorption onto montmorillonitic clay." *Environmental engineering & management journal (eemj)* 14.5 (2015).

[101] S. Salvestrini et al. "Considerations about the correct evaluation of sorption thermodynamic parameters from equilibrium isotherms". *The journal of chemical thermodynamics* 68 (2014), pp. 310–316.

[102] T. T. Trinh et al. "A procedure to find thermodynamic equilibrium constants for CO_2 and CH_4 adsorption on activated carbon". *Phys. chem. chem. phys.* 17.12 (2015), pp. 8223–8230.

[103] H. N. Tran, S. J. You, and H. P. Chao. "Thermodynamic parameters of cadmium adsorption onto orange peel calculated from various methods: A comparison study". *Journal of environmental chemical engineering* 4.3 (2016), pp. 2671–2682.